Simultaneous multi-slice imaging techniques for MRI acquisitions

Jenni Schulz

Simultaneous multi-slice imaging techniques for MRI acquisitions

Thesis, Radboud University Nijmegen, The Netherlands

Illustrated; with bibliographic information and English and Dutch summaries

ISBN: 978-94-6284-114-7

Printed by Ipskamp Drukkers, Enschede

Simultaneous multi-slice imaging techniques for MRI acquisitions

Proefschrift

ter verkrijging van de graad van doctor
aan de Radboud Universiteit Nijmegen
op gezag van de rector magnificus prof. dr. J. H. J. M. van Krieken,
volgens besluit van het college van decanen
in het openbaar te verdedigen op donderdag 12 oktober 2017
om 12:30 uur precies

door

Jennifer Schulz

geboren op 25 september 1986
te Gelsenkirchen, Duitsland

Promotor:	Prof. dr. David G. Norris
Manuscriptcommissie:	Prof. dr. Arend Heerschap (voorzitter)
	Prof. dr. Penny Gowland University of Nottingham, Verenigd Koninkrijk
	Dr. Kawin Setsompop Massachusetts General Hospital Boston, Verenigde Staten

Simultaneous multi-slice imaging techniques for MRI acquisitions

Doctoral Thesis

to obtain the degree of doctor
from Radboud University Nijmegen
on the authority of the Rector Magnificus prof. dr. J. H. J. M. van Krieken,
according to the decision of the Council of Deans
to be defended in public
on Thursday, October 12, 2017 at 12:30 hours

by

Jennifer Schulz

born on September 25, 1986
in Gelsenkirchen, Germany

Supervisor:	Prof. dr. David G. Norris
Doctoral thesis committee:	Prof. dr. Arend Heerschap (chair)
	Prof. dr. Penny Gowland University of Nottingham, United Kingdom
	Dr. Kawin Setsompop Massachusetts General Hospital Boston, United States of Americ

Contents

Chapter 1

Introduction

1.1. History of magnetic resonance imaging

The hyperfine structure in nuclei was first observed in 1881 by Albert Abraham Michelson [94], but only in 1924, Wolfgang Pauli was able to explain this phenomenon in terms of quantum mechanics (QM) by proposing the existence of a nuclear magnetic moment. [116] By extending the Stern-Gerlach experiment, Columbia University Professor Isidor Rabi described and measured nuclear magnetic resonance in molecular beams in 1938 [125] for which he was awarded the Nobel Prize in 1944. Felix Bloch and Edward Purcell discovered the magnetic resonance phenomenon in liquids and solids in 1946 and performed the first nuclear magnetic resonance (NMR) experiments. [13][124] In 1952, they both received the Nobel Prize for Physics for their pioneering work. In 1950, Erwin L. Hahn used pulsed RF energy in NMR to generate the first "spin-" or "Hahn-echo" [56]. Raymond Damadian then showed at Brooklyn's Downstate Medical Center in the early 1970s the existence of different T1 and T2 relaxation times in tissue distinguishing tumorous from healthy tissue. [31] The first two-dimensional back-projected MR image was provided by Paul C. Lauterbur at Stony Brook University using gradients in the magnetic field in 1973. [78] Peter Mansfield further developed this technique and the mathematical analysis of the MR signals in the 1970s by developing echo-planar imaging (EPI) leading to faster acquisitions and better image quality. [89] Due to the importance of Lauterbur's and Mansfield's work with respect to the application of MRI in medicine, both received the Nobel Prize in Physiology or Medicine in 2003. Based on the work of Lauterbur, Richard Ernst in 1975 introduced two dimensional

Fourier transform imaging with phase-encoding to NMR which is still the basic reconstruction method in current MRI techniques. [74] The first MR image of a human was presented by Peter Mansfield and Andrew A. Maudsley in 1977/78, a cross section through a finger [90], but only in the early 1980s, the first useful images could be reconstructed after the Fourier transform-based spin-warp imaging technique of Bill Edelstein and his colleagues at the Aberdeen Universtity was introduced. [38] This dominant method of spatial encoding is still used today.
Clinical MR scanners became available in the 1980s and are now commonly used at magnetic field strengths of 1.5T and 3T. [1] Since signal-to-noise ratio (SNR) increases approximately linearly with the field strength, there has been a trend to higher field strengths such as 7T and 9.4T installed at research centers worldwide. [64]

1.2. Principles of magnetic resonance imaging

This section gives an overview of the principles of magnetic resonance imaging. Starting of with the description of a "spin" and "magnetization", signal formation will be explained followed by spatial encoding. At a later stage, a short introduction to RF-pulses and pulse sequences can be found. Finally, functional MRI and the BOLD contrast mechanism will be introduced. More detailed descriptions are given in standard textbooks such as [10][81][25][20].

1.2.1. Spin and NMR

In QM, atomic nuclei have an angular momentum which is called spin. If the number of neutrons and protons in a nuclei are both even, the spins are paired and cancel each other out resulting in no net spin. However, if the number of neutrons and protons are both odd, the nucleus is a boson with an integer spin. If the number of all nucleons in total is odd (^{1}H, ^{13}C, ^{15}N, ^{19}F, ^{23}Na, ^{31}P, ...), the nucleus is a fermion possessing a half-integer spin. This non-zero spin is a requirement for NMR. The nuclei then carry an angular momentum $\mathbf{I}$ and a magnetic moment $\boldsymbol{\mu}$ which are coupled by the isotope specific gyromagnetic ratio γ (eq. 1.1). Hydrogen has a gyromagnetic ratio of 42.58MHz/T.

$$\boldsymbol{\mu} = \gamma \cdot \mathbf{I} \tag{1.1}$$

In equilibrium, magnetic moments are randomly distributed cancelling each other out. In the presence of an external static magnetic field $\mathbf{B_0}$, however, they interact with the field and align in 2I+1 ways reinforcing or opposing $\mathbf{B_0}$, and precessing around the $\mathbf{B_0}$-axis. The discrete energy levels obtained are described in QM according to the Zeeman effect as

$$E_m = -\gamma\hbar m B_0. \tag{1.2}$$

Fermions with spin 1/2 such as hydrogen have two eigenstates and μ_z is aligned parallel or anti-parallel to $\mathbf{B_0}$. The energy difference

$$\Delta E = -\gamma\hbar B_0 \tag{1.3}$$

corresponds to the resonance radio frequency (RF) that can be emitted or absorbed. The energy of a photon is described by the Planck-Einstein relation (eq. 1.4) and proportional to its frequency ω_0.

$$E = \hbar\omega_0 = \gamma\hbar B_0 \tag{1.4}$$

This resonance frequency, also called Larmor frequency, can then be written as:

$$\omega_0 = \gamma B_0 \tag{1.5}$$

The probability of occupancy of the eigenstates is not equal, but depends on ΔE, the Boltzmann constant k and the absolute temperature T and is given by the Boltzmann distribution in eq. 1.6 with $n_\uparrow$ indicating the number of magnetic moments aligned parallel to $\mathbf{B_0}$ and $n_\downarrow$ anti-parallel.

$$\frac{n_\uparrow}{n_\downarrow} = \exp(-\Delta E/kT) \tag{1.6}$$

Since the parallel alignment is energetically slightly favorable and more populated than the anti-parallel state, there is a resulting net magnetization ($\mathbf{M_0}$) along the $\mathbf{B_0}$-direction.

1.2.2. Magnetization and relaxation

The motion of the bulk magnetic moments can be described by the classical Euler's equation of motion (eq. 1.7).

$$\frac{d}{dt}\mathbf{M}(t) = \mathbf{M}(t) \times \gamma\mathbf{B}(t) \tag{1.7}$$

The solution is a rotational motion of the magnetization about the axis of the static magnetic field called precession. Equation 1.7 can be transformed into a coordinate system that rotates about the **B**-axis with an angular frequency ω,

$$\frac{d}{dt}\mathbf{M} = \frac{\delta}{\delta t}\mathbf{M} + \omega \times \mathbf{M}, \tag{1.8}$$

giving

$$\frac{\delta}{\delta t}\mathbf{M} = \mathbf{M} \times (\gamma\mathbf{B} + \omega). \tag{1.9}$$

Equation 1.9 states that if ω is chosen to be equal to $-\gamma B_0$, the effect of the main magnetic field disappears and the Larmor frequency of a magnetic dipole in an external static magnetic field (eq. 1.5) is obtained. In addition to the static magnetic B_0-field, an oscillating magnetic field (B_1)

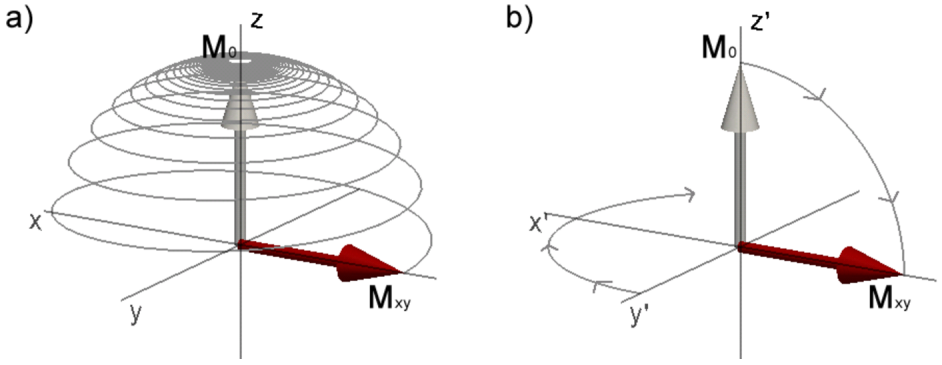

Figure 1.1: Trajectory of an RF pulse excitation with a flip angle of 90° [69]
a) In the laboratory frame, the net magnetization $M_0 = M_z$ precesses on a spiral trajectory into the x-y plane resulting in a transverse component of the magnetization M_{xy} precessing at the Larmor frequency.
b) In the rotating frame, the magnetization is tipped into the x'-y' plane.

can be applied. It can be described by

$$B_1(t) = B_1^e(t)\ e^{-i(\omega_{rf}+\phi)}. \tag{1.10}$$

B_1^e defines the envelope function, ω_{rf} the carrier frequency and ϕ the initial phase angle. The carrier frequency ω_{rf} typically is in the radio frequency (RF) range. Therefore, the B_1-field is also referred to as RF-field or RF-pulse because it is usually only applied during a short time. (More specific information on RF pulse design is given in section 1.3.)

If a circularly polarised B_1 field is applied perpendicular to B_0, the overall precession in the laboratory frame will be a combination of two individual precessional motions and therefore describe a spiral trajectory as visualized in figure 1.1 a). The precession can also be observed from a rotating frame of reference. In the rotating frame, the main magnetic field B_0 does not have any influence. If B_1 is additionally applied "on resonance" with a frequency $\omega_{rf} = \omega_0$, it becomes stationary. The magnetization M_0 will then only precess about $\mathbf{B_1}$. While B_1 is applied, the net magnetization will rotate into the transverse plane (figure 1.1 b)).

In the laboratory frame, there will arise a transverse magnetic field component M_{xy} rotating at the Larmor frequency according to:

$$M_{xy} = M_0\ \sin(\alpha) \quad \text{with} \quad \alpha = \gamma B_0 \tau. \tag{1.11}$$

τ reflects the duration of the B_1 field, also referred to as radiofrequency (RF) field or RF pulse due to its short duration in the order of milliseconds. The process of applying an RF pulse and creating transverse magnetization is referred to as excitation with the flip angle α. After the application of the RF pulse, the spin system is no longer in equilibrium. Over time, it will return to the state with no transverse magnetization and longitudinal magnetization of M_0. This process is called relaxation and shown in figure 1.2. There are two different relaxation mechanisms: the spin-lattice relaxation characterized by the time constant T_1 and the spin-spin relaxation which is characterized by the time constant T_2. T_1 describes the longitudinal relaxation which is the recovery of the M_z component. T_2 describes, on the other hand, the transversal relaxation which is the loss of the phase coherence between individual spins. Due to the random nature of the spin-spin interaction, the signal decay caused by T_2 relaxation is irreversible. Both time constants depend on the tissue and the field strength. The evolution of the individual magnetization

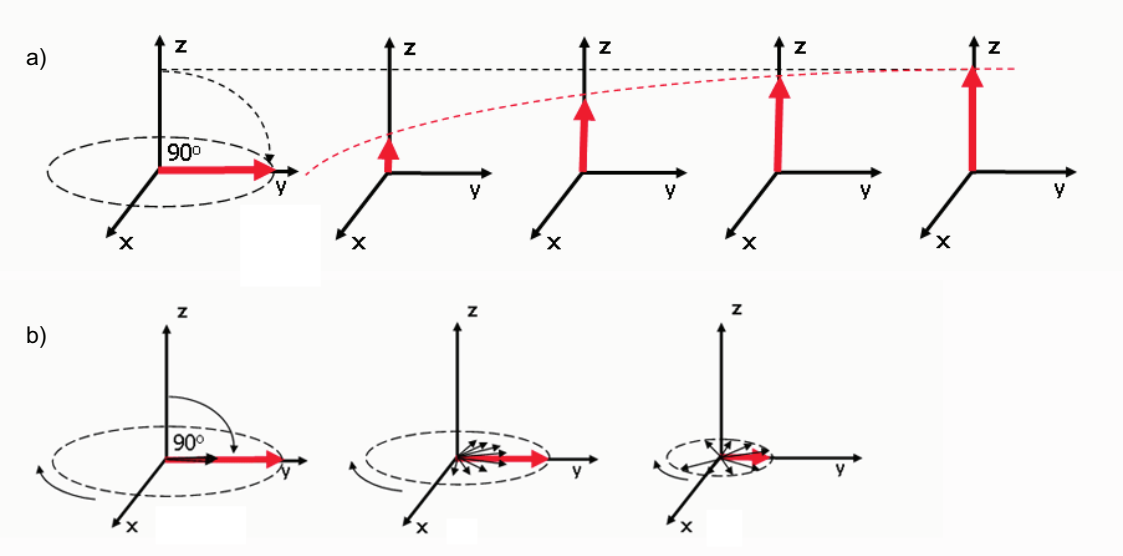

Figure 1.2: T_1, T_2 and T_2^* relaxation processes after a 90° RF Pulse excitation [126]
a) The process of the longitudinal relaxation described by the time constant T_1 is the recovery of the magnetization component M_z to equilibrium which is an exponential process.
b) The process of the transversal relaxation described by the time constants T_2 and T_2^* is the loss of the phase coherence of the spin system referred to as de-phasing.

components is described by the Bloch equations:

$$\frac{dM_x}{dt} = M_x \times \gamma B_x - \frac{M_x}{T_2} \tag{1.12a}$$

$$\frac{dM_y}{dt} = M_y \times \gamma B_y - \frac{M_y}{T_2} \tag{1.12b}$$

$$\frac{dM_z}{dt} = M_z \times \gamma B_z - \frac{M_z - M_0}{T_1} \tag{1.12c}$$

In the rotating frame of reference, the Bloch equations and its solutions are very much simplified. The exponential relaxation process of M_z can be described as

$$\frac{dM_z}{dt} = \frac{M_0 - M_z(t)}{T_1} \tag{1.13a}$$

yielding

$$M_z(t) = M_0 \left(1 - e^{-t/T_1}\right) + M_z(0)\ e^{-t/T_1}. \tag{1.13b}$$

Whereas the de-phasing of the M_{xy} component is described by

$$\frac{dM_{xy}}{dt} = \frac{M_{xy}(t)}{T_2} \tag{1.14a}$$

yielding

$$M_{xy}(t) = M_{xy}(0)\ e^{-t/T_2} = M_0\ \sin(\alpha)\ e^{-t/T_2}. \tag{1.14b}$$

In fact, the loss of the phase coherence of the spins is faster than described by T_2 due to local field inhomogeneities and susceptibility effects which are, however, constant over time. Since the cause of the variation of Larmor frequency of the spin system is fixed, the resultant de-phasing can be reversed (see section 1.4.4). This effect is referred to as T_2^* relaxation and described by the time constant T_2^* according to equation 1.15.

$$\frac{1}{T_2^*} = \frac{1}{T_2} + \frac{\gamma \Delta B_0}{2\pi} \tag{1.15}$$

ΔB_0 describes the deviation of the magnetic field from the main magnetic field B_0. From equation 1.15, it becomes clear that T_2^* is always smaller than T_2.

1.2.3. From NMR to MRI

To produce a 2D image in MRI, the generated signal has to be localized. That is done through the application of magnetic field gradients and distinguishes MRI from the basic NMR technique. The gradients generate a spatially varying magnetic field. This magnetic field has maximum values about two orders of magnitude smaller than the main magnetic field, but a lot larger than the magnetic field inhomogeneities yielding precise encoding of spatial locations.

Magnetic field gradients

The standard MR system consists of a set of gradients which are aligned in three orthogonal directions (x,y and z). The net gradient magnetization $\mathbf{G}$ is the sum of the three components $\mathbf{G_x}$, $\mathbf{G_y}$ and $\mathbf{G_z}$ which are spatially varying linear functions. Since the gradient strength at the isocenter is always 0, the Larmor frequency is preserved at this location. For other locations, the Larmor frequency becomes position $\mathbf{r}$ dependent according to

$$\omega(\mathbf{r}) = \gamma\left(\mathbf{B_0} + \mathbf{r}\ \mathbf{G}\right). \tag{1.16}$$

K-space formalism

The complex signal $S(t)$ that is acquired during an MR scan consists of a range of frequencies (see section 1.2.3) and is related to the proton density function $\rho(\mathbf{r})$ by

$$S(t) = \int \rho(\mathbf{r})\ e^{-i\int_0^t \mathbf{G}(t')dt'} d^3\mathbf{r}. \tag{1.17}$$

With

$$\mathbf{k} = \gamma \int_0^t \mathbf{G}(t')dt', \tag{1.18}$$

a simple expression for the acquired signal $S(k)$ is found and the proton density can be obtained by inverse Fourier Transform (FT) of it.

$$S(k) = \int \rho(\mathbf{r})\ e^{ik\mathbf{r}} dk \tag{1.19a}$$

$$\rho(\mathbf{r}) = \int S(k)\ e^{-ik\mathbf{r}} dk \tag{1.19b}$$

The Fourier Transform therefore connects the image domain to the k-space domain in which the data is acquired. The discrete steps in k-space define the image field-of-view (FOV) and the

maximum extents the image resolution.

$$\Delta k = \frac{1}{FOV} \tag{1.20a}$$

$$\frac{1}{2k^{\max}} = \frac{FOV}{N} \tag{1.20b}$$

In order to avoid aliasing in the image, the nominal sampling interval has to obey the Nyquist theorem. It states that to be able to describe a signal unambiguously, the sampling frequency should be at least twice the highest frequency contained in the signal.
Additionally, the sampled k-space range determines the spatial frequencies to be resolved in the image. Low spatial frequencies determining most of the SNR are located in the centre of k-space, whereas high spatial frequencies responsible for fine details are on the outside. Therefore, higher resolution images can be obtained by covering larger extents.

1.2.4. Spatial encoding in MRI

Slice selection

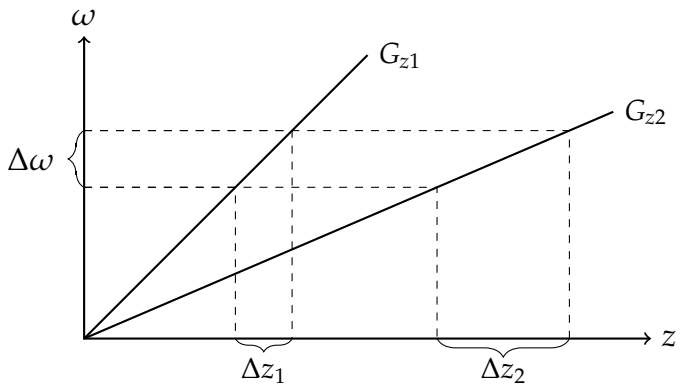

Figure 1.3: The principle of slice selection. An RF pulse with bandwidth $\Delta\omega$ is applied together with the slice select gradient G_z and only spins that meet the resonance condition are excited. The gradient strength defines the slice thickness, whereas the slice profile is defined by the RF pulse shape. Weaker gradients G_{z2} excite a thicker slice, stronger gradients G_{z1} a thinner.

Slice selection is the process of exciting only spins in a certain volume of interest. It is achieved by playing out an RF pulse while applying a linear magnetic field gradient in the slice direction

which has historically been the z-direction. This gradient is called slice select gradient G_z. Since the RF pulse is designed to have a certain bandwidth $\Delta\omega$ and particular centre frequency, only spins with a Larmor frequency in this interval can be excited as shown in figure 1.3. The slice thickness is then defined according to equation 1.21. For small flip angles, the slice profile is defined by the FT of the RF pulse waveform.

$$\Delta z = \frac{\Delta\omega}{\gamma G_z} \tag{1.21}$$

Due to the simultaneous application of the slice selection gradient and the RF pulse, spins within the excited slice experience different magnetic fields. This however causes a linear phase gradient along the slice resulting in dephased magnetization. To rewind this effect and eventually obtain a signal, a slice rephase gradient needs to be applied. For a symmetric RF pulse, the rephase gradient moment needs to be half of the moment of the slice select gradient. Inversion and slice selective 180° refocusing pulses do not need a rephasing gradient because the phase accumulation of the first half of the RF pulse will cancel out during the second half.

Frequency encoding

Frequency encoding has traditionally been applied the x-axis, also referred to as readout (RO) direction. A linear frequency encoding gradient G_x is applied while acquiring the signal. As described before, the gradient G_x causes a spatially varying frequency along the RO direction. The acquired signal has a readout bandwidth corresponding to the difference of the lowest and highest frequencies and is proportional to the gradient strength G_x.

Phase encoding

The encoding in the third dimension along the y-axis is called phase encoding. The applied gradient G_y is played out after the excitation and before the readout period. It consists of a short gradient pulse of time t_{PE} introducing a spatially dependent phase (eq. 1.22) to the signal along the phase encode direction.

$$\Delta\phi(y) = \gamma\, G_y\, t_{PE}\, y \tag{1.22}$$

A single phase encoding gradient is not sufficient to localize the origin of the signal. For each repetition, a particular phase encode gradient with a unique moment is applied. The concept of phase encoding combined with frequency encoding is visualized in figure 1.4.

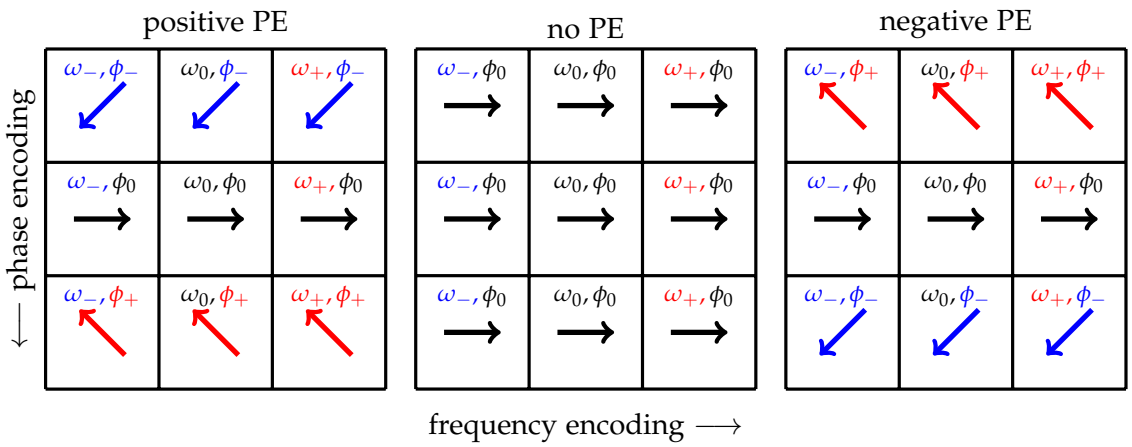

Figure 1.4: Phase encoding combined with frequency encoding. In the given example, each voxel consists of a different spin density. Frequency encoding differentiates the columns ($\omega_-/\omega_0/\omega_+$) and phase encoding the rows ($\phi_-/\phi_0/\phi_+$). Three different phase encode gradient schemes are given: positive PE gradient, no PE gradient and negative PE gradient. The acquired signal is always equal to the sum of all nine vectors and needs to be disentangled by FT.

1.3. RF PULSE DESIGN

As introduced in chapter 1.2.2, the transverse magnetization in MRI is created by the application of an RF pulse. There are many different RF pulses consisting of different shapes coming along with different characteristics. Typical examples would be a hard or rectangular pulse, a sinc pulse or tailored pulses based on the Shinnar-le Roux (SLR) algorithm. [10]

1.3.1. Hard pulses

In the time domain, hard pulses have the shape of a rectangular function as shown in figure 1.5. They are typically used if no spatial or spectral selection is necessary and are characterised by a very short pulse duration. The bandwidth of a hard pulse is usually very broad and a wide range of frequencies can be excited. Within the range of the small flip angle approximation, the spatial excitation profile of a rect-pulse is a sinc-shape.

Hard pulses are simple, but not very commonly used. A typical application would be a 3D excitation where the imaging volume is filling the coil sufficiently. [10]

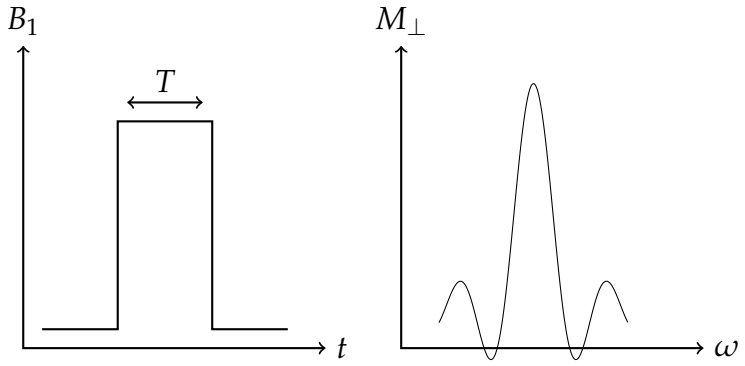

Figure 1.5: On the left, there is a hard pulse (rect-function) in the time domain. On the right, the spectral excitation profile in the form of a sinc-function which translates to the spatial profile.

1.3.2. Sinc pulses

Sinc-pulses are used very commonly in MRI. They are very flexible and can, for instance, be used as (selective) excitation, saturation, inversion or refocusing pulses. As shown in figure 1.5, the sinc-function's central lobe has the highest amplitude and is continued by smaller adjacent lobes of alternating polarity.

The Fourier transform of the sinc-function is the rect-function which would give an ideal slice profile in the case of uniform excitation. However, RF-pulses are not infinitely long. Long pulses increase TE and TR which is not desired. Therefore, the sinc-pulse needs to be truncated at a defined point. The mathematical description is then:

$$B_1(t) = \begin{cases} A \cdot sinc\left(\frac{\pi t}{t_0}\right) = A t_0 \frac{\sin\left(\frac{\pi t}{t_0}\right)}{\pi t}, & -N_L t_0 \leq 0 \leq N_R t_0 \\ 0, & \text{elsewhere} \end{cases} \tag{1.23}$$

A: peak RF amplitude at t=0

t_0: one-half the width of the central lobe

N_L, N_R: number of zero-crossings to the left and right of central lobe

The bandwidth of the sinc-pulse is typically defined as:

$$\Delta f = \frac{1}{t_0} \tag{1.24}$$

with a time-bandwidth-product:

$$T\ \Delta f = N_L + N_R. \tag{1.25}$$

A consequence of the truncated sinc is that for higher flip angles ringing can occur at the edges of the excited slice. To prevent this and improve the slice profile, the sinc-function is typically used in combination with a Hamming or Hanning window tapering the RF amplitude.

1.3.3. Shinnar-Le Roux pulses

With the help of the Bloch equations (see equations 1.12), the excitation profile of an RF-pulse can be calculated in a "forward" manner. The "inverse" problem, in which the frequency profile is given, is more difficult. For small flip angles, the small flip angle approximation holds and the RF-pulse can be obtained by taking the inverse Fourier transform of the frequency profile. However, due to nonlinearities in the Bloch equations, this approach does not work well for larger flip angles.

The Shinnar-Le Roux (SLR) algorithm is a mathematical description to solve the inverse problem. Amplitude and phase of the RF pulse are determined on the basis of desired bandwidth, flip angle, percent ripple in the passband and percent tipple in the stopband. SLR pulses are very commonly used for nonadiabatic pulse design in imaging and spectroscopy. [117] Lately, adiabatic pulses based on the SLR algorithm have also been developed. [6]

The underlying mathematical tools of the SLR algorithm are the two-dimensional mathematical representation of rotations SU(2) and the hard pulse approximation. The magnetization is then described by two polynomials with complex coefficients. The forward SLR transform transforms the RF pulse to the two polynomials. The inverse transform results the other way round in the RF pulse form.

1.4. Pulse sequences

A pulse sequence is a combination of RF pulses and gradients. To acquire the data forming an image, many different pulse sequences have been developed. Two basic variants are the gradient echo (GE) and spin echo (SE) sequence which will be explained in this section. In general, a sequence starts with the excitation, followed by the decoding part and has as a third step the readout section.

1.4.1. Gradient echo

The gradient echo sequence is the simplest type of sequence. After the excitation, the generated transverse magnetization is first dephased and then rephased with the readout gradients. To save time, the slice select and phase encode gradient are usually played out at the same time as the read dephasing gradient (see figure 1.6). The time between consecutive excitations is called repetition time TR, whereas the time between excitation and echo formation is referred to as echo time TE. Each repetition the phase encode gradient is incremented by Δk_y until all phase encoding steps, respectively k-space lines, have been acquired. Depending on the values of TR and TE, the obtained image can have a T_1, proton density or T_2^*-weighting.

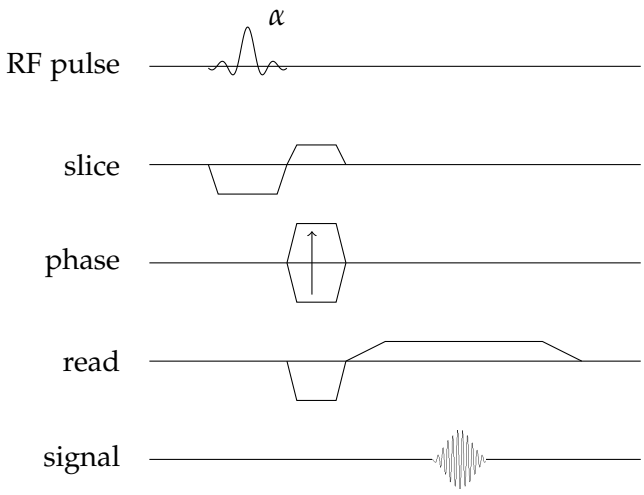

Figure 1.6: The gradient echo sequence.

If the repetition time is kept short, the magnetization will continue to dephase after the signal has been acquired and can interfere in an uncontrolled way with following acquisitions. This can be avoided by applying a phase encode rewinder gradient of opposite moment after the ADC or a

spoiler gradient. The spoiler is usually played out along the x-axis destroying residual transverse magnetization. A second consequence of a short TR is the incomplete recovery of the longitudinal magnetization. However, after several TR intervals, the magnetization reaches a steady state M_z depending on T_1, TR and α:

$$M_z = M_0(1 - \exp(-TR/T_1))/(1 - \cos(\alpha)\ \exp(-TR/T1)). \tag{1.26}$$

The optimal flip angle which yields the maximal steady state signal for given TR and T_1 is called the Ernst angle and defined as:

$$\alpha_{\text{Ernst}} = \arccos(\ \exp(-TR/T_1)\ ). \tag{1.27}$$

If $TR \ll T_1$, the optimal flip angle is much smaller than 90° and the sequence is referred to as fast low angle shot (FLASH).

1.4.2. Time-of-flight magnetic resonance angiography

FLASH sequences can also be used to image blood vessels.
In general, there are two different main techniques of angiography: contrast-enhanced (CE) and non-contrast-enhanced (NCE) magnetic resonance angiography (MRA). A main drawback of CE-MRA techniques is the necessity for (in general Gadolinium (Gd)-based) contrast agents. Lately, there have been concerns about the safety ([149][122]) which reinforced the interest in NCE-MRA techniques such as white blood time-of-flight magnetic resonance angiography (TOF-MRA). [59][96][162]
The TOF-MRA technique is commonly used for peripheral and intracranial applications. [93] To obtain a contrast between the stationary tissue and the flowing blood, TOF-MRA makes use of the so called in-flow effect. [5] The flowing blood moves unsaturated spins from outside of the slice into the imaging plane. This blood has full equilibrium magnetization producing a much brighter signal than the saturated stationary spins of the background tissue. In order to only have blood from one side entering the imaging plane, a presaturation pulse can be applied on one side of the slice. This makes TOF-MRA flow direction sensitive and distinguishes arteriograms from venograms.
TOF-MRA can be applied in 2D and 3D mode. The 2D version shows a better blood-tissue contrast

whereas the 3D sequence generally has higher signal-to-noise (SNR). In any case, the obtained 3D vascular information is generally presented using a maximum intensity projection (MIP). [77]
A main drawback of TOF-MRA is the time-consuming acquisition. To achieve a maximum blood signal, fresh blood has to enter the imaging plane every TR. Therefore, TR and slice thickness have to be chosen with respect to the expected velocity of the blood flow. [73]

1.4.3. Echo planar imaging

Echo planar imaging (EPI) was first proposed by Mansfield [88][90] and is one of the fastest available sequences. It is routinely used in functional MRI (fMRI) and widely spread in the neuroscience community due to its sensitivity to physiological changes upon brain activation. The excitation pulse is followed by a gradient echo train. The readout gradients with changing polarity introduce multiple echoes. Small gradient blips are introduced for spatial encoding along the phase encoding direction in between the acquisition of successive echoes (called blipped EPI [144]). The sequence diagram is shown in figure 1.7. In this way, the entire k-space is acquired after only one slice selective excitation, but every other k-space line needs to be time-reversed post hoc to account for the alternating sampling order.

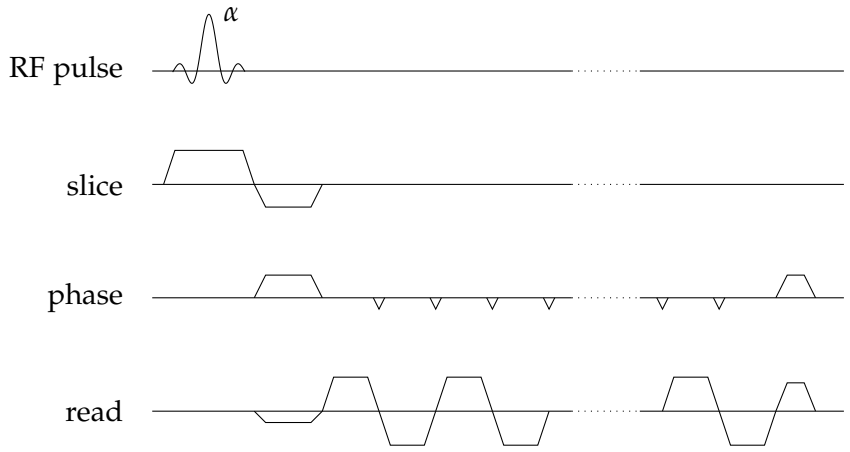

Figure 1.7: The echo planar imaging sequence.

A downside of this sequence type is that hardware demands on the system are very high. Fast gradient switching and high slew rates are mandatory regarding the gradient system. Side effects like eddy currents and heat can cause unwanted time-varying gradients and shifts in the main magnetic field. Common methods to reduce the influence of eddy currents on gradient fields are eddy current compensation and shielded gradient coils (active or passive). Further, there are

post-processing tools available for correction.

1.4.4. Spin echo

The spin echo sequence is essentially similar to the GE sequence, but uses a 180° refocusing pulse to generate the echo after the 90° excitation pulse (see figure 1.8). The application of the 180° refocusing pulse reverses the effect of the T_2^* relaxation and the image contrast is therefore mainly dominated by T_2 relaxation. This makes spin echo sequence less sensitive to susceptibility artifacts than gradient echo sequences.

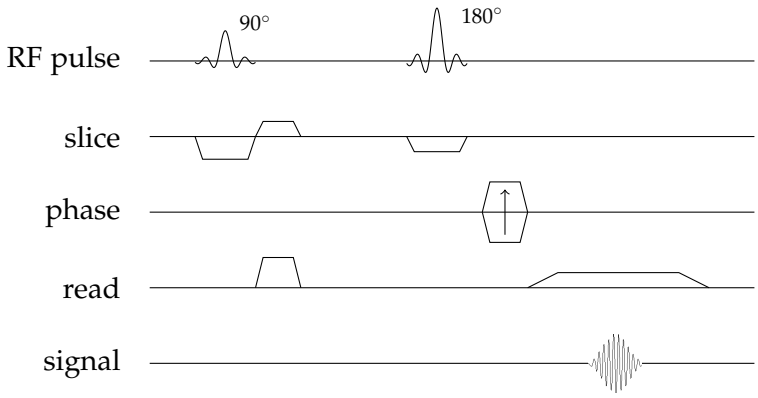

Figure 1.8: The spin echo sequence. The sequence diagram shows the 90° excitation and 180° refocusing pulses as well as the corresponding gradients.

1.4.5. Half-Fourier acquisition single-shot turbo spin echo

It is possible to apply a train of spin echoes following a single excitation. This means that the first spin echo will be repeatedly refocused with 180° RF pulses. If the entire image is acquired in a single shot, the sequence is called half-Fourier acquisition single-shot turbo spin echo (HASTE). However, if the acquisition of one image occurs sequentially, one speaks of rapid acquisition with relaxation enhancement (RARE) imaging or simply turbo spin echo (TSE)/fast spin echo (FSE), first proposed by Hennig in 1986. [62] TSE sequences are the most common sequences in clinical diagnosis and often preceded by a magnetization preparation experiment.
The number of applied refocusing pulses after a single excitation pulse is called echo train length (ETL). The maximal time which is available to play out the echo train is defined by the time constant T_2. In HASTE imaging, there is in principle no given scheme in which the phase encoding

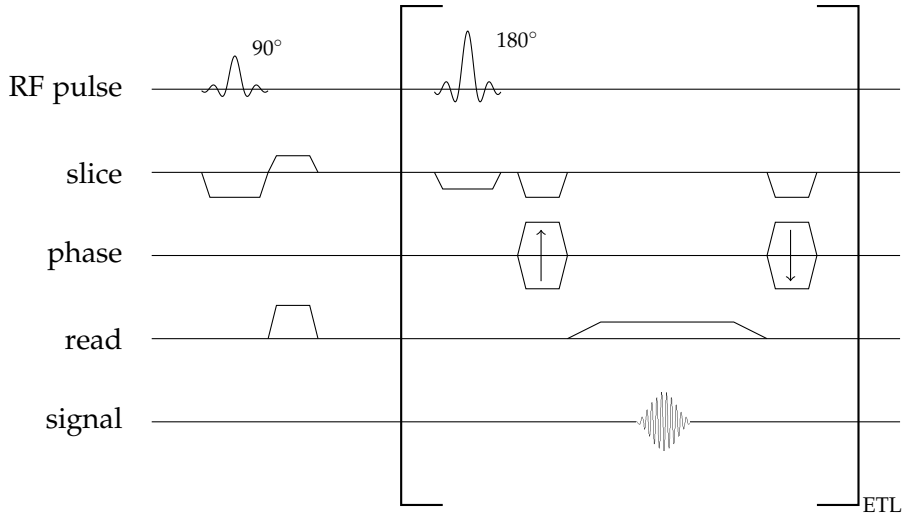

Figure 1.9: The HASTE sequence is also known as single-shot RARE sequence. It consists of a 90° excitation pulse followed by an echo train of 180° refocusing pulses. To fulfill the CPMG condition, the time-integral over the gradients has to be equal for each TE.

steps need to be acquired. In order to save time, it is even possible to omit k-space lines using parallel imaging techniques such as SENSE, GRAPPA or Partial Fourier. The effective echo time TE_{eff} is referred to as the time between the excitation and the acquisition of the centre of k-space and mainly defines the contrast between tissue types in the image. After each spin echo read out and before the next refocusing pulse, a phase encode rewinder gradient is played out ensuring stability of the phase and avoiding varying resonant offsets and therefore transfer of phase-encoded information to later echoes. Additionally, spoiler gradients are applied before and after the refocusing pulse to destroy any free induction decay (FID) signal that can be introduced by the RF pulse and take effect on subsequent spin echoes.

A main drawback of the HASTE sequence is its high power deposition due to the large number of 180° refocusing pulses which is especially problematic at high resolution and high field strength. The heating caused by the RF pulses in the tissue is measured by the specific absorption rate (SAR) in Watt per kilogram and is proportional to the static magnetic field strength B_0, the flip angle α and the bandwidth of the RF pulse $\Delta\omega$ as shown in equation 1.28. Due to high SAR values, many clinical protocols cannot be transferred to field strength of 7T or higher without modifications in accordance with the limitations defined by the International Commission on Non-Ionizing Radiation Protection (ICNIRP) guidelines.

$$\text{SAR} \sim B_0^2 \, \alpha^2 \, \Delta\omega. \tag{1.28}$$

An absolute requirement for artefact free HASTE images is the fulfillment of the Carr-Purcell-Meiboom-Gill (CPMG) condition. It demands that excitation and all refocusing pulses are 90° out of phase. If CPMG is not fulfilled, different coherence pathways can interfere in an uncontrolled manner causing intensity fluctuation and total signal dropouts in the acquired image.

1.5. Accelerated imaging

1.5.1. Parallel imaging

A possibility to accelerate an acquisition is the use of parallel imaging techniques. In parallel imaging, the k-space data is undersampled in a controlled manner making use of multi-channel receiver coils to reconstruct the full image. Each individual coil has a unique sensitivity profile depending on its position and orientation. This can be used to replace part of the gradient spatial encoding by coil spatial encoding. There are several commercially available techniques including SMASH [141], SENSE [123] and GRAPPA [55]. SENSE-like techniques perform the reconstruction and therewith the disentangling of the aliased images in image space, whereas SMASH and GRAPPA-like techniques work in k-space.
The acceleration factor R that can be obtained is equal to the phase encoding lines which are skipped in k-space. For sequences like HASTE or TSE, the duration of the ETL is dramatically reduced resulting in images of maintained or even improved quality. Along with the time saving, there comes a sensitivity reduction caused by the factor R smaller data sample which is a factor of $\sqrt{R}$. Additionally, there is also a spatially varying noise contribution introduced depending on the noise correlation between individual coils due to their geometric properties and the aliasing of the acquire image. Typically, the noise is described by the geometry factor g. [123]

1.5.2. Multiband imaging

In 2D imaging, parallel imaging techniques can only accelerate an acquisition in-plane. Multiband imaging, however, enables an acceleration along the slice direction. First proposed in 2001 by Larkman et al [76], multiband (also called simultaneous multi-slice (SMS)) imaging provides the possibility to accelerate acquisition in the slice direction by exciting and acquiring N slices simulta-

neously without the penalty of a $\sqrt{R}$-reduction in signal to noise ratio. [45][97] The superimposed slices can consequently be reconstructed using a SENSE [123] or slice-GRAPPA [138] algorithm. To excite multiple slices simultaneously, the RF pulse needs to be modified. A linear phase ramp is applied to an individual RF pulse to shift the slice to the desired location. All individually modified RF pulses are subsequently complex-summed [97] to form the new multiband RF pulse. Both, the power deposition and amplitude of the RF pulse, depend linearly on the number of simultaneously excited slices making multiband pulses rather demanding. The RF amplitude is limited by the maximal transmit voltage of the system and different techniques have been developed to maintain an acceptable range especially when applying high multiband factors. [61][53][163][4] So far, multiband factors of up to 12 have been reported, but smaller factors are more commonly used. For a more detailed introduction into multiband imaging techniques, it is referred to reference [8].

PINS

Power independent of number of slices (PINS) [102] pulses are generated by convolving a sinc-pulse with a comb-function. The Fourier Transform yields a periodic excitation profile, meaning that the number of simultaneously excited slices is only limited by the dimensions of the RF coils or the size of the body. Due to their nature, PINS pulses have a low power deposition and are especially suited for SE-based sequences at high field strength. [71][39][101] Lately, a combination of multiband and PINS, so called MultiPINS pulses, has been developed taking advantage of both characteristics; the SMS excitation and the reduced energy deposition. [40]

CAIPIRINHA

A limitation of multiband imaging lies in the ability to properly disentangle the aliased slices as reconstruction is dependent on the coil sensitivity profiles. To improve image quality, controlled aliasing in parallel imaging results in higher acceleration (CAIPIRINHA) [19] has been introduced. By alternating the phase of the individual RF pulses in a defined order, it is possible to shift individual slices within the field-of-view and enlarge the distance between similar voxels. For acquisitions acquiring more than one k_y-line per excitation, the shift can also be evoked by gradient

blips along the slice direction. This technique is called blipped-CAIPIRINHA. [138]

1.6. Functional MRI

Functional MRI is a main technique to investigate the brain. It is able to detect haemodynamic changes involved in the neuronal activity in the brain. Commonly one speaks of the detection of 'brain activation' which refers to the electrophysiological activity of a group of neurons involved in a certain process which is taking place in the brain. Ogawa et al. [107] showed in 1990 the first blood-oxygen-level-dependent (BOLD) contrast in rats. In 1992, Ogawa and Kwong showed independently the first BOLD activation in human brains in a study involving sensory stimulation. [75][109] In the same year, the EPI sequence as useful imaging technique was also demonstrated by Bandettini and Blamire. [7][12] Since then, BOLD fMRI has become the most popular fMRI technique and is commonly measured using an echo-planar imaging (EPI) sequence.

1.6.1. BOLD contrast

Haemodynamic response function

Strictly speaking, the BOLD contrast is not oxygen-level dependent, but relies on the deoxyhemoglobin level present in the tissue which changes upon activation. Whereas oxyhemoglobin is diamagnetic, deoxyhemoglobin is paramagnetic perturbing the main magnetic field. This results in a local decrease in main magnetic field homogeneity. The physiological mechanism describing the relation of brain activation and the measured fMRI signal is described by the haemodynamic response function (HRF) (figure 1.10). The HRF represents the result of the interplay of cerebral blood flow (CBF), cerebral blood volume (CBV) and the oxygen consumption rate ($rCMRO_2$).
First, upon stimulation, the local $rCMRO_2$ increases accompanied by the amount of deoxyhaemoglobin. In the literature, a fast response (also called 'initial dip') has been reported which is believed to originate from the initial oxygen consumption before changes in CBF and CBV take effect. The 'inital dip' remains however very difficult to measure. [22][129]
Second, local CBV increases. The increase in blood volume and hence in the amount of deoxyhaemoglobin causes a decrease in signal intensity. However, the accompanying increase in CBF has an opposing effect and remains the dominant contribution. Dilating vessels will supply a

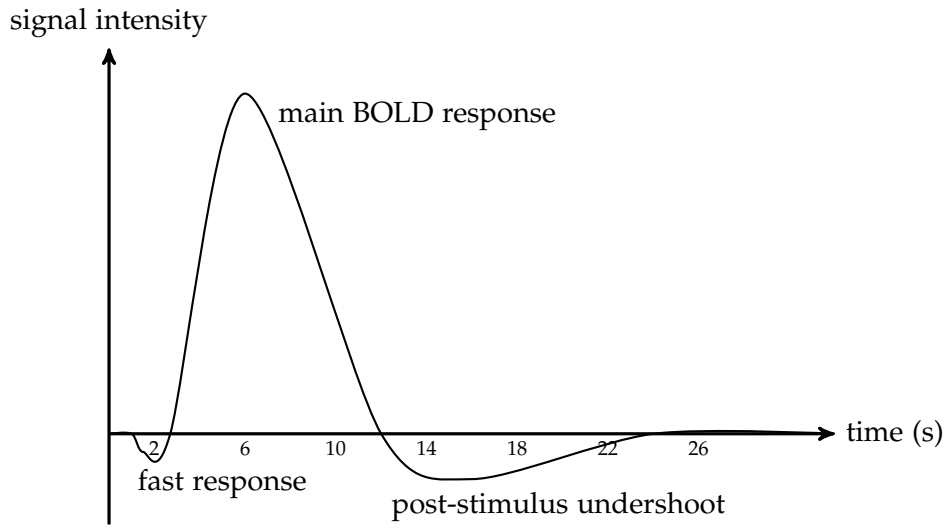

Figure 1.10: The haemodynamic response function is shown as signal intensity versus time. It consists of three parts: the fast response, the main BOLD response and the post-stimulus undershoot.

region with more oxygenated blood than actually processed by the cortex. This leads to a decrease in the concentration of deoxy-haemoglobin. Since the CBF increase outweights the local CBV and $rCMRO_2$ increase, the main BOLD response appears as a positive signal at the site of activation compared to the resting state level. Whereas the fast response appears within 1-3 seconds after stimulation, the main BOLD response reaches its maximum after 6-8 seconds.
The third part of the HRF is called the post-stimulus undershoot. After stimulus termination, the signal first decreases below and then returns back to baseline. The underlying mechanism is so far not understood. The first theory is based on the balloon modell. [23][87] It states that the return of CBV to baseline is delayed compared to the return of CBF which happens faster. This will cause an temporarily increased level of deoxy-haemoglobin which results in the undershoot. More recent convincing studies propose a slightly different explanation. They show a rapid return to baseline for the CBV suggesting the undershoot to be a result of the still elevated $CMRO_2$. A detailed review on the post-stimulus undershoot is given in reference [159].

BOLD contrast mechanisms

The BOLD response consists of four underlying contrast mechanisms: extravascular static dephasing, extravascular dynamic dephasing, intravascular T_2-effect and intravascular dephasing. They

contribute differently to the signal depending on the main magnetic field strength, the vessel size, the spatial resolution and imaging sequence.

When the oxygen level changes, the change in the local field extends beyond the blood vessels. [103] Assuming a cylindrical model, the frequency shift at a distance r and an azimuthal angle ϕ of a vessel with diameter a oriented at an angle θ to the main magnetic field B_0 can mathematically be described as

$$\Delta\omega = 2\ \pi\ \omega_0\ \Delta_\chi\ \ (1 - Y) \sin^2\theta \left(\frac{a}{r}\right)^2 \cos(2\phi). \tag{1.29}$$

The relative blood oxygenation is represented by Y and Δ_χ describes the susceptibility difference between fully oxygen-saturated blood and the surrounding tissue. For relatively large vessels ($a > 20\mu m$ at 4T) [108], the effect on the spins is static. Due to diffusion, they move within an area without significant change in B_0. However, for smaller vessels ($a > 20\mu m$), such as capillaries or post capillary vessels, the effect is a dynamic dephasing. In SE-bases sequences, static dephasing can be refocused whereas the signal in GE-based sequences will always be influenced by both mechanisms.

The third mechanism arises from the interaction of deoxy-haemoglobin in red blood cells and water spins within erythrocytes and the surrounding plasma. [143] An alternative explanation for the intravascular T_2-effect is the diffusion of water spins in and out of the erythrocytes. In any case, it is an effect which is randomly occurring and therefore contributes to the signal in GE and SE-sequences.

The intravascular dephasing, also called intravascular frequency offset effect, is due to a frequency shift of spins within a vessel oriented at an angle α with respect to the main magnetic field B_0. [108] Assuming a large number of randomly oriented vessels, the signal attenuation within a voxel will static and can therefore be refocussed in a SE-experiment.

The contribution of each BOLD contrast mechanism to the obtained signal is not only depending on the sequence, but also on the main magnetic field strength. With increasing B_0, the signal is weighted more towards the site of neuronal activation. Whereas at 1.5T the SE-signal is mainly arising from the intravascular T_2-effect, the relative contributions of dynamic and static effects are nearly equal at 3T. [106] At higher field strengths of 7T and above, the dynamic dephasing will become dominant which results in higher specificity.

1.7. Outline

As introduced in section 1.5, acceleration techniques are a viable tool in MR imaging of today. This thesis will focus on the multiband (MB) technique. It will give different examples of how MB imaging can be applied in different sequences and on how it can be combined with other techniques.

In chapter 2, MB imaging is first applied in a 3D TOF-MRA sequence demonstrating that besides its 2D character, it can also be advantageous when applied in a multi-slab acquisition [135]. Chapter 3 shows how one can further accelerate an EPI acquisition by combining MB imaging with the echo-shifting technique [17]. In chapter 5, MB imaging is combined with the PINS method implemented in a HASTE sequence. A clinical application is presented with effectively reduced acquisition time. Chapter 6 is introducing an RF pulse design of a new form of MB pulse based on a quadratic phase modulation. Applied as excitation-refocusing pulse pair in SE-based sequences, this implementation will reduce peak power voltage while achieving the common MB acceleration.

In the end, a general summary of this thesis is given in chapter 7.

Chapter 2

Multiband multislab 3D time-of-flight magnetic resonance angiography for reduced acquisition time and improved sensitivity

Jenni Schulz[1], Rasim Boyacioğlu[1], David G Norris[1,2]

[1]Donders Institute for Brain, Cognition and Behaviour, Radboud University Nijmegen, The Netherlands

[2]Erwin L. Hahn Institute for Magnetic Resonance Imaging, University Duisburg-Essen, Essen, Germany

Magn Reson Med (2016), 75:1662-1668. doi:10.1002/mrm.25774

Abstract

Purpose: To explore the use of multiband (MB) imaging in multislab (MS) 3D time-of-flight magnetic resonance angiography (TOF-MRA) and to improve acquisition time efficiency (TA), inflow contrast and sensitivity in vessel detection.

Theory and Methods: TOF-MRA is commonly used for imaging intracranial vessels. A MB-MS 3D-TOF-MRA sequences was implemented to excite and acquire multiple slabs simultaneously. CAIPIRINHA was used in addition to improve the quality of image reconstruction. Compared to a standard protocol which acquired three slabs in total the MB-MS protocol reduced the thickness by 3 while simultaneously acquiring data from 3 slabs. The total TA was also reduced by a factor 3.

Results: This technique maintains CNR while reducing TA, compared to standard single-band/MOTSA acquisitions, leading to an increase in CNR/$\sqrt{TA}$ of 1.65 compared to the standard protocol. Furthermore, the strong inflow contrast and increased MTC caused by the MB excitation pulses improves the sharpness of the vessel borders which is reflected by a 5% higher FWHM of the vessel size and a 17% higher slope of the vessel borders compared to the standard single-band acquisition.

Conclusion: MB-MS 3D-TOF-MRA can appreciably accelerate image acquisition and combines the high spatial resolution of 3D imaging with the additional inflow contrast advantage of thinner slab acquisitions without introducing excessive noise arising from the MB reconstruction.

2.1. Introduction

Magnetic resonance angiography (MRA) has become more important in clinical practice over the last few years. Compared to ionizing radiation and intra-arterial catheter manipulation, it is a relatively safe and easy method. [161] The development of new hardware and imaging techniques reduced previous limitations of intravoxel dephasing, signal saturation, and signal ghosting to a level where high resolution images can be acquired in acceptable acquisition times. [161] The 3D vascular information is generally visualized using a maximum intensity projection (MIP [77]) in the form of angiograms and can give insight into velocity and volume flow rate of blood. [73]
There are two different main techniques of angiography: contrast-enhanced (CE) and non-contrast-enhanced (NCE) MRA. In general, CE-MRA is the more common technique. It is mainly used for carotid imaging having shorter acquisition times and better anatomical coverage. A major drawback of CE-MRA is the necessity for contrast agents generally based on Gadolinium (Gd). The examination of patients with severe renal dysfunction may be contraindicated with Gd-based contrast agents due to Nephrogenic Systemic Fibrosis (NSF) after administration. [122][149] The concern about the safety of gadolinium-based contrast agents has reinforced interest in NCE-MRA techniques such as white blood time-of-flight magnetic resonance angiography (TOF-MRA) which is commonly used for peripheral and intracranial applications. [59][96][162]
TOF-MRA sequences can be used in 2D or 3D mode. 2D TOF-MRA sequences generally generate a higher blood-tissue contrast and are routinely used for imaging carotid arteries and peripheral vasculature oriented orthogonal to the imaging plane. [93] 3D sequences have generally higher signal-to-noise (SNR) ratios and can acquire higher spatial resolution images which is desirable for neuroimaging, especially imaging intracranial vessels. With the multiple overlapping thin 3D slab acquisition (MOTSA [112]), it is possible to combine the contrast advantage of 2D acquisitions with the higher SNR of 3D acquisition and further reduce blood signal saturation while maintaining SNR. The main disadvantage of TOF-MRA is long acquisition times which makes it sensitive to motion. This can cause undesired effects like misregistration, complete signal loss in highly stenotic arteries and furthermore limits the field of view. [18][43][84][152]
First proposed in 2001 by Larkman et al [76], multiband (also called simultaneous multi-slice (SMS)) imaging provides the possibility to accelerate acquisition in the slice direction by exciting and acquiring N slices simultaneously without the penalty of a $\sqrt{N}$-reduction in signal to noise ratio. [45][97] The superimposed slices can consequently be reconstructed using a SENSE [76] or

slice-GRAPPA [138] algorithm. An improvement in reconstruction quality can be achieved by shifting slices with respect to each other in the field of view (FOV) along the phase-encoding (PE) direction. This technique is known as controlled aliasing in parallel imaging results in higher acceleration (CAIPIRINHA) [19] and works by modulating the phase of the excitation pulse. However, in high spatial resolution or short TR acquisitions, the spurious thermal noise correlation between aliased slices can further influence the image quality and the right combination of multiband and shift factors has to be chosen carefully. [139]

In this work, a new multiband multislab technique is introduced. It significantly reduces acquisition times, preserves the high spatial resolution of 3D imaging, exploits the contrast advantage of acquisition with thinner slabs, and has increased magnetization transfer contrast (MTC) caused by the off-resonance nature of the multiband pulses. This increased sensitive is particularly of benefit for the detection of intracranial vessels. [37][95] For the lowest acceleration factor (MB factor = 2), the time saving with respect to a single-band standard acquisition is 50%. Higher MB factors, such as 4, can actually achieve time savings of up to 75%. If the necessary reconstruction reference scan (section 2.2.3) is additionally taken into account, a MB MS 4 acquisition will still be accelerated by 64% in comparison to a single-band standard acquisition. The MB factor of 3 used here results in an acceleration of 66% (55% respectively).

2.2. Methods

2.2.1. Sequence

In order to implement the MB technique, a standard FLASH-TOF sequence was modified. The sequence's original excitation RF pulse was frequency-modulated to match each desired slab position. These individually modified RF pulses were subsequently complex-summed [97] to form the new excitation pulse. Furthermore, controlled aliasing in parallel imaging results in higher acceleration (CAIPIRINHA) was implemented to improve the quality of the reconstruction of the aliased slices. [19] With CAIPIRINHA, the phase of the excitation pulse is adjusted for every acquired k-space line in a way that a slice is shifted in the FOV along the PE direction.

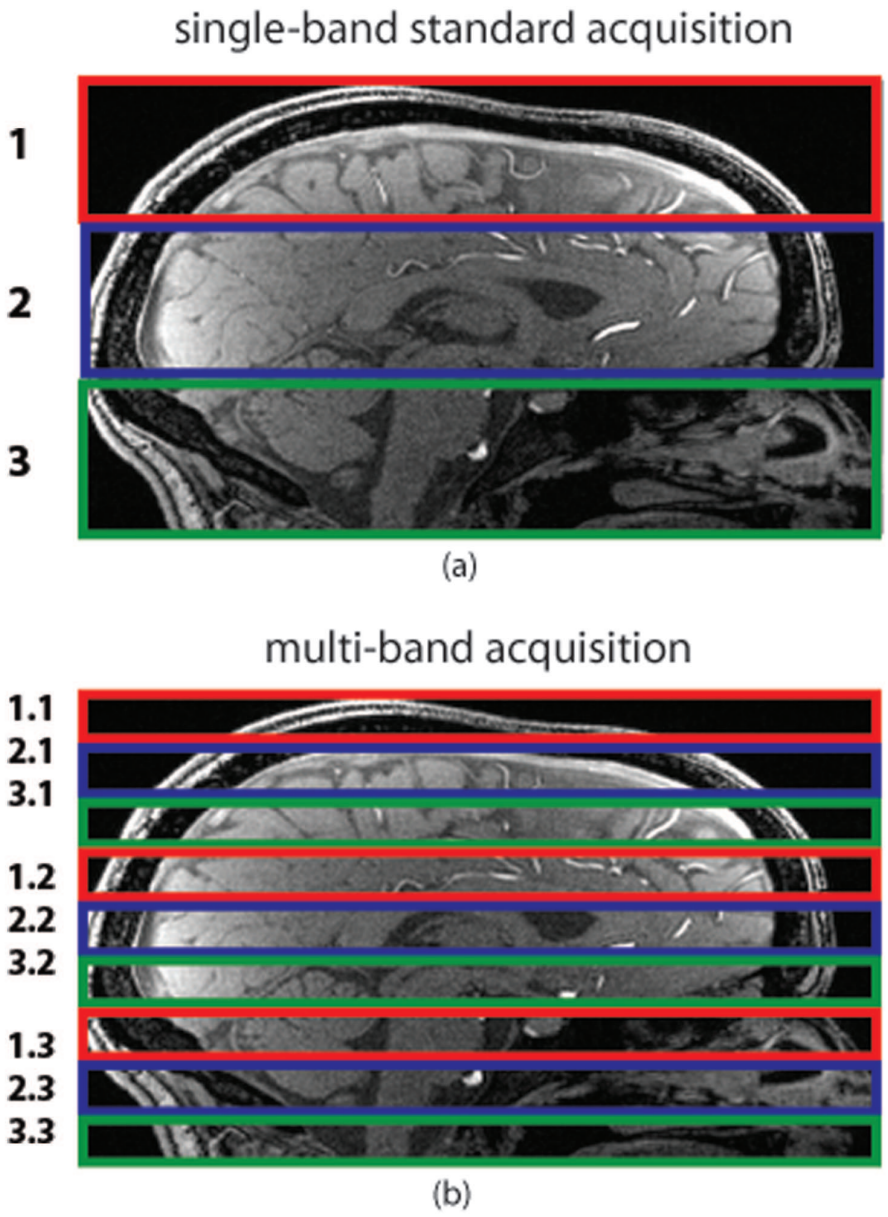

Figure 2.1: Acquisition scheme (neglecting oversampling). The single-band standard protocol acquires 3 slabs of 96 slices in the order indicated by numbers 1,2,3 to cover the entire FOV. For the MB MS acquisition, one needs to acquire 3 times 3 slabs of 32 slices simultaneously to cover the same FOV.

2.2.2. Acquisition

Data were acquired on a 3T MR system (Magnetom Trio, Siemens AG, Healthcare Sector, Erlangen, Germany) using a standard 32-channel head coil. Experiments are reported here from six healthy subjects (2 male and 4 female, aged 23-32) who gave prior informed consent according to local ethical committee requirements.

Our single-band standard protocol for whole brain coverage is based on a standard clinical protocol [1] which is routinely used for evaluating brain vessels. It consists of 3 slabs of 96 slices per slab oversampled by 25% at a TR of 24 ms and a TE of 4.33 ms with a flip angle of 15°. The total acquisition time for this whole brain protocol is TA=9:20 min. The voxel size is 0.6x0.5x0.65 mm^3 and the matrix 384x288 with GRAPPA 2 in-plane acceleration, phase resolution 90%, slice resolution 70% and PF (partial fourier) 6/8 in phase and slice direction. The slice spacing between simultaneously excited slabs decreases with increasing MB factor. To maintain a slice separation of the aliased slices which is suitable for the slice-GRAPPA reconstruction, we used a multiband factor of 3 for the MB MS acquisition. This means that three slabs are excited and acquired simultaneously. To make use of additional in-flow, the individual slab thickness was decreased to 32 slices per slab each oversampled by 25%. For the same brain coverage it was then necessary to acquire nine slabs in total, in three groups of three simultaneously acquired slabs. This is illustrated in figure 2.1. To provide the best possible separation of aliased voxel positions, the middle of the three simultaneously acquired slabs was additionally shifted with CAIPIRINHA [19] by a factor of FOV/2 [139]. All other parameters of the MB MS acquisition were identical to the standard whole brain protocol resulting in an acquisition time of TA=3:04 min.

In order to evaluate the MB MS performance with respect to its sensitivity, a third scan with identical parameters but using the original single-band RF excitation pulse was performed. This again corresponds to a whole brain coverage acquisition of 9 slabs of 32 slices each and TA =9:12 min. If acquisition and reconstruction performed perfectly in the MB MS case, the single-band thin slab and MB MS acquisition would give identical results. Both 9-slab acquisitions are expected to show an increased inflow effect compared to the single-band standard acquisition because degradation of blood signal due to exposure to multiple excitation pulses will be less pronounced.

[1] provided by Radboud University Nijmegen Medical Centre, Department of Radiology, Dr. Anton Meijer

2.2.3. Reconstruction

Reconstruction was performed off-line in MATLAB (MATLAB 7.12, The MathWorks Inc., Natick, MA, 2011) using raw data files. The superimposed slices were unaliased using the slice-GRAPPA algorithm. [138] For a fair comparison, the reference images were also reconstructed using this pipeline without the slice-GRAPPA part.
As the acquisition of a standard TOF-MRA scan for multiband reconstruction purposes would be so time-consuming that the time-efficiency of the MB MS acquisition would be entirely lost, the use of a rapid 3D FLASH sequence was explored. In preliminary experiments, it was shown that it is possible to successfully use FLASH images for reference purposes despite its different contrast. [101] We subsequently pursued data acquisition using 3D FLASH reference data (1:31min). The data were additionally bias field corrected using FAST (FMRIB Software Library v5.0, Oxford, UK, 2012).

2.2.4. Analysis

In order to determine signal intensities and their variations, 3 regions-of-interests (ROIs) per slice were selected. In total, 75 slices were investigated equally distributed over the whole region imaged. The specified ROIs were randomly distributed within the slice, and contained one vessel each. The vessel pixels and their corresponding intensities were identified using an intensity threshold which was determined from a local histogram of pixel intensities. The corresponding local tissue intensities for each vessel were identified from the same ROI using the same threshold. Given that the noise field varies with location this strategy ensured that a broad range of both noise values and vessels was sampled. The determined signal intensities and its variations were used for all of the following quantitative analysis steps.
To compare image quality, we investigated the contrast-to-noise ratio (CNR) and CNR efficiency $\mathrm{CNR}/\sqrt{TA}$. We approximated the variation in vessel signal $\sigma(S_{\text{vessel}})$ by the local variation in tissue signal $\sigma(S_{\text{background tissue}})$. The actual variation in vessel signal $\sigma(S_{\text{vessel}})$ is in fact impossible to evaluate and the approximate variation in vessel signal is the most relevant for clinical practice. Hence:

$$\mathrm{CNR} = \frac{S_{\text{vessel}} - S_{\text{tissue}}}{\sigma(S_{\text{tissue}})} \tag{2.1}$$

In addition to this quantitative assessment of image quality, a visual grading was performed by three naive expert readers following the method of [65]. The images were rated on 'overall image quality' and 'visibility of vessels' on a 4-fold scale: 1) poor - 2) good - 3) very good - 4) excellent. As a crucial metric for the quality of obtaining a good MIP from an acquisition, the vessel-to-background ratio (VBR) as defined in equation 2.2 was investigated. Higher VBRs will lead to better visibility of the vessels. [66][67]

$$\mathrm{VBR} = S_{\mathrm{vessel}} / S_{\mathrm{tissue}} \tag{2.2}$$

Because the MB MS acquisition consists of thinner slabs, the saturation effect of blood within a slab should be less pronounced compared to the single-band standard protocol. To investigate this assumption, the 'normalized vessel size' (nVS) was evaluated. Therefore, the mean size of the same vessels was determined by counting the contributing voxels above the vessel/tissue threshold and normalized to the single-band thin slab acquisition. In addition the 'normalized signal intensity per voxel' (nSI) was evaluated. This was determined by taking the intensity of a voxel as a measure for the amount of blood flowing in this voxel and normalized to the single-band thin slab acquisition.

To further investigate vessel delineation, the intensity profile at the vessel border was measured. This was achieved by using the already identified squared ROIs and defining 2 diagonal profiles across each ROI. On each profile, two linear fits were performed in order two find both vessel edges. The values were averaged to determine the slope of a specific vessel. In addition, the full width at half maximum (FWHM) was calculated for each profile and therefore each vessel.

To judge the completeness of the angiograms, we determined the branching index of the right hemisphere for three subjects using The Vascular Modeling Toolkit (vmtk 1.2). The index was obtained by counting the vessels' bifurcations which were visible in the angiogram.

To investigate the dependency of the slice-GRAPPA performance on the reconstruction and the noise, three slices from the single-band standard acquisition were synthetically superimposed, re-separated with the reconstruction pipeline including the slice-GRAPPA algorithm and compared to the original slices.

2.3. Results

Figure 2.2 shows two different bias field corrected slices of a representative subject for the single-band standard, MB MS and single-band thin slab scan. In terms of image quality regarding vessel detection, MB MS performs similar to the single-band standard protocol. The images suffer from an increased noise contribution in the MB MS case which is also reflected by the lowest CNR, table 2.1. However, the VBR remains still higher in the MB MS case in comparison to the single-band standard protocol, just like the CNR/$\sqrt{TA}$.

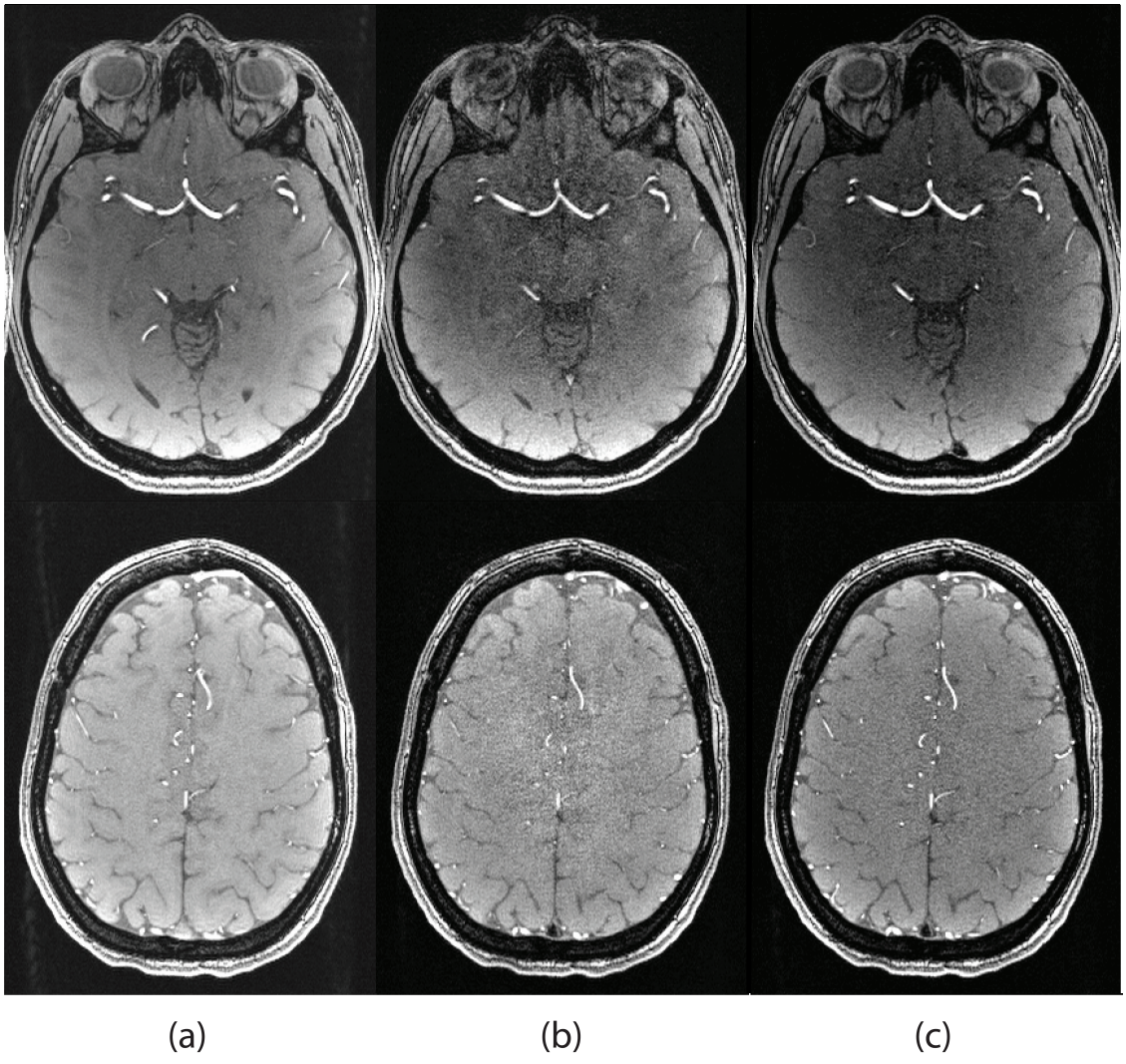

Figure 2.2: Top and bottom show two different bias field corrected slices from the single-band standard protocol (a), MB MS acquisition (b) and single-band thin slab scan (c). The MB MS acquisition appears more noisy, but with the same vessel detection ability.

The visual grading by the expert readers shows similar results to the CNR measurements. The overall images quality was rated lowest in the MB case with 2.28 ± 0.61, compared to the single-band standard protocol with 3.26 ± 0.79 and the single-band thin slab scan with 3.11 ± 0.82. However, the gradings for the visibility of vessels are similar: MB MS 2.86 ± 0.82, single-band standard protocol 3.13 ± 0.86, single-band thin slab 3.22 ± 0.68.

Although the values of the nVS are highest for the single-band standard acquisition, MB MS is superior regarding the average signal intensities per identified vessel voxel (nSI). MB MS performs similarly to the 'ideal' single-band acquisition and both outperform the single-band standard protocol by approximately 10%.

While the slope of the vessel border (table 2.2) is steepest for the MB MS acquisition, the vessel border is least well delineated for the standard single-band acquisition. This result is independent of the vessel size. The FWHM values of the profiles of the vessels is highest for the MB MS acquisition, followed by the single-band standard acquisition. The single-band thin slab scan has the smallest FWHM.

The good vessel visibility results in detailed MIPs for the MB MS acquisition shown in figure 2.3. Here, the MB MS acquisition shows a higher sensitivity to smaller vessels especially in the center of the image in comparison to the single-band standard protocol which is indicated by arrows in the zoomed images on the bottom. Its performance is in fact very close to the 'ideal' single-band thin slab acquisition having a three times longer acquisition time. The branching index given in table 2.2 indicates that the MB MS acquisition performs almost as well as both single-band scans.

Table 2.1: This table shows CNR, CNR/$\sqrt{TA}$, VBR, normalized mean sizes and normalized signal intensities of the determined vessels and their standard deviation for the MB MS acquisition in comparison to the single-band standard and single-band thin slab scans as an average of all subjects.

	contrast-to-noise ratio (CNR)	**CNR / $\sqrt{TA}$**	**vessel-background ratio**	**normalized vessel size**	**normalized signal intensity per voxel**
standard	6.15 ± 4.91	2.02 ± 1.61	2.22 ± 0.62	1.19 ± 1.38	0.91 ± 1.00
MB MS	5.85 ± 4.28	3.34 ± 2.44	2.55 ± 0.74	0.97 ± 1.16	1.05 ± 1.23
thin slab	7.74 ± 6.77	2.55 ± 2.23	2.66 ± 0.62	1.00 ± 1.10	1.00 ± 1.00

In order to evaluate the dependency of the slice-GRAPPA performance on the reconstruction, the ratio of the difference between a representative single-band standard image and a synthesized multiband image calculated from the single-band standard image to the single-band standard image was evaluated (see figure 2.4). The ratio varies with a mean of 15.3% within the brain and

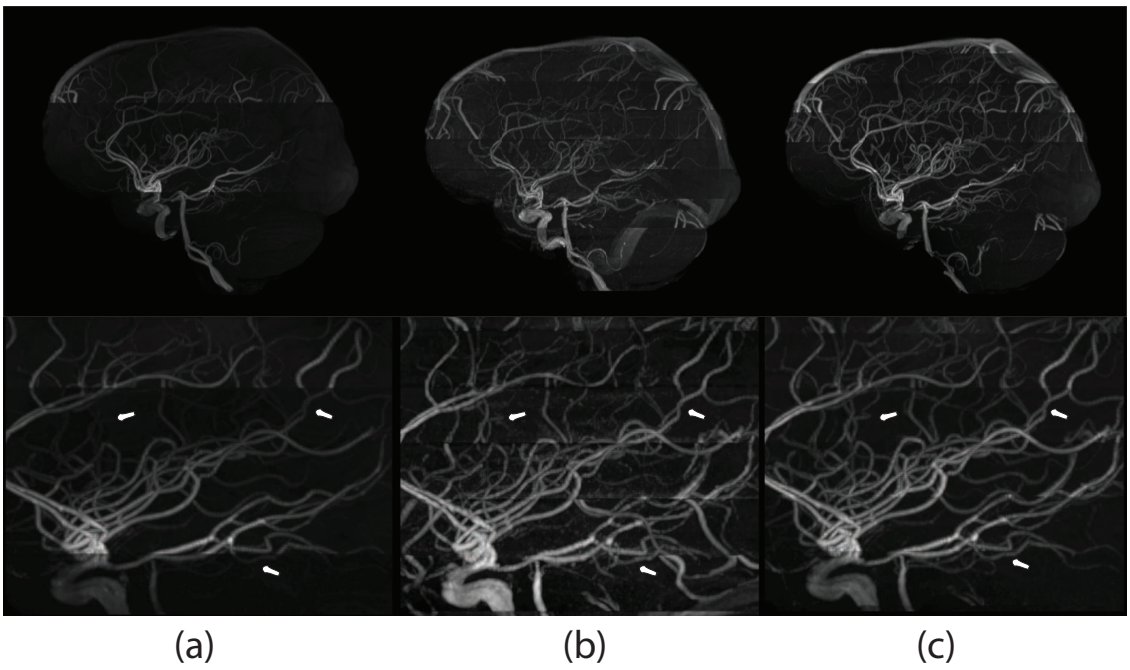

Figure 2.3: MIPs (angiograms) of whole brain coverage (top) and zoomed images (bottom) of the single-band standard (a), MB MS (b) and single-band thin slab (c) acquisition. The MB MS angiograms show a higher sensitivity to smaller vessels due to its thinner slabs indicated by arrows in the bottom images.

Table 2.2: This table shows the mean of the slope of the vessel borders (column 1 all vessels, column 2 small vessels with FWHM < 3vx) and its standard deviation for the MB MS acquisition in comparison to the single-band standard and single-band thin slab scans as an average of all subjects. Additionally, mean and standard deviation of the FWHM of the vessel profiles are given. The branching index is given for the right hemisphere of three representative subjects.

	slope of vessel (I/voxel)		**FWHM (voxels)**	**branching index**
	all	small		
standard	127.3 ± 73.4	121.8 ± 68.3	5.16 ± 3.20	19.3 ± 4.7
MB MS	149.1 ± 79.9	147.9 ± 74.9	5.43 ± 3.11	17.0 ± 1.7
thin slab	144.4 ± 80.9	131.9 ± 71.3	4.97 ± 2.84	19.7 ± 2.3

is highest in the center regions. This corresponds to the region where two out of the three slices are fully superimposed. Owing to the use of the GRAPPA technique, it is not possible to evaluate the noise outside of the brain. [128][137]

2.4. Discussion

The MB MS 3D TOF-MRA sequence is able to reduce the acquisition time by approximately the selected multiband factor. A shorter TA combined with acquisitions of thinner slabs makes TOF-MRA now faster and possibly less sensitive to motion. This can make TOF-MRA more attractive as higher spatial resolutions and larger FOV coverage would be possible leading eventually to new TOF-MRA applications.

Since MB imaging leads to an increased MTC-effect further saturating background tissue, an improvement in small-vessel conspicuity is achieved. [37][95] In addition to the advantage of acquiring thinner slabs for the MB MS acquisition, the visibility of intracranial vessels is improved. Increased unsaturated inflow boosts the signal of the vessels which leads to improved visibility of vessels compared to a single-band standard 3D TOF-MRA protocol. This advantage improves both the performance of TOF-MRA and the robustness.

Because the single-band standard acquisition images are less affected by noise, the tissue-vessel threshold is easier to determine and more stable than for the MB MS acquisition. The analysis algorithm will therefore identify those vessels more precisely. This gives rise to the higher values of the nVS in the single-band standard acquisition compared to MB MS and single-band thin slab scan. The same reasoning holds for the determination of the branching index which is slightly lower in the MB MS acquisition compared to both single-band acquisitions. However, the higher

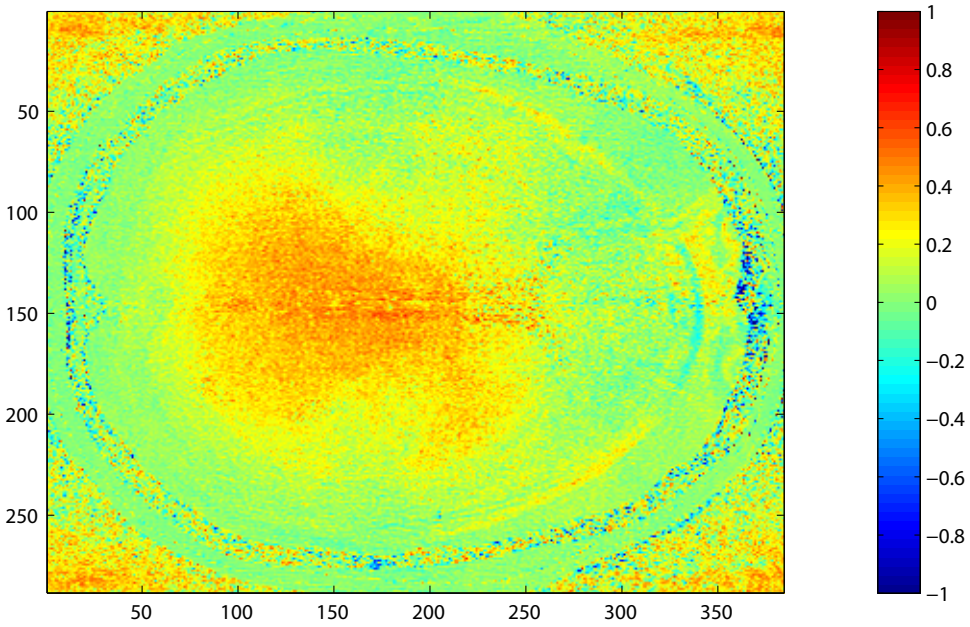

Figure 2.4: The normalized ratio of the difference between the single-band standard image and the simulated multiband image to the single-band standard image (slice of a representative subject) indicates that the slice-GRAPPA algorithm sufficiently separates the superimposed slices, but has reduced sensitivity in the center of the brain.

nSI in the MB MS case clearly shows the presence of additional in-flow in thinner slab acquisitions. Another result of the additional in-flow contrast is the better vessel sharpness in the MB MS acquisition. The generally higher intensities of the vessels will support steeper slopes of the linear regression. The slightly higher FWHM of the MB MS acquisition corroborates this finding. In line with the quantitative results is the visual grading indicating slightly worse image quality of the MB MS acquisition due to increased noise, but similar vessel visibility. The high variances in table 2.1 and 2.2 indicate that the selection of vessels to be evaluated in the analysis is inhomogeneous. The sizes range over a broad interval which represents the actual distribution within the brain.

In this work, a three-fold acceleration was performed. However, depending on the experiment higher multiband factors are generally possible. In fact, MB factors of up to 8 have already been successfully used in practice [154]. But first, very high MB factors in 3D acquisitions would eventually result in thin slices making isotropic resolution rather difficult and second also enforce very thin slabs which will have unacceptable excitation profiles. Hence, in order to achieve a suitable slab thickness, very high MB factors are not useful for 3D acquisitions.

More general limitations for high multiband factors would be RF pulse related SAR problems or peak voltage clipping. These are well known multiband issues and have been focus of research. Therefore, to work around the SAR limit one could use PINS pulses [102] and a way to deal with the peak voltage would be a phase-optimization. [53][61] Another limit is the separation of the simultaneously excited slabs which can be improved by the use of CAIPIRINHA [19] and better interslice leakage artifact reduction techniques [26]. The application of the slice-GRAPPA algorithm in MB MS 3D TOF-MRA is so far unproblematic and expected to also perform sufficiently for higher multiband factors if the inter-slab distance is not decreased.

In order to perform multiband imaging and apply the slice-GRAPPA technique, a sufficient number of receiver coils is necessary as for all parallel imaging techniques. For a low number of receiver channels, MB MS 3D TOF-MRA is therefore not applicable.

The simultaneous and periodic excitation of slabs makes MB MS 3D TOF-MRA generally attractive to applications of greater body coverage in which a high number of slabs is desired, like imaging upper and lower limbs. In fact, for application where motion is unproblematic, a future perspective would be to combine MB MS 3D TOF-MRA with large FOV coils [46] to further benefit from its high time-efficiency.

2.5. Conclusion

In this work, the proof-of-concept of the MB MS technique was demonstrated and evaluated in comparison to a clinical standard protocol focusing on whole brain coverage.
MB MS images and angiograms gave reliable results which are comparable to single-band standard 3D TOF-MRA acquisitions. The technique shortens acquisition times by a factor roughly equal to the number of simultaneously acquired slabs. As opposed to MOTSA-type sequences, 3D MB MS TOF-MRA maintains CNR and the high spatial resolution of a 3D acquisition while also having the contrast advantage associated with thinner slab acquisitions. Additional MTC contrast increases soft tissue suppression, and the MB reconstruction does not introduce excessive noise. Further work would be required to assess robustness and improvements in vessel detectability in a clinical context.

Chapter 3

Multiband echo shifted echo planar imaging

Rasim Boyacioğlu[1], **Jenni Schulz**[1], David G Norris[1,2]

[1]Donders Institute for Brain, Cognition and Behaviour, Radboud University Nijmegen, The Netherlands

[2]Erwin L. Hahn Institute for Magnetic Resonance Imaging, University Duisburg-Essen, Essen, Germany

Magn Reson Med (2016). doi: 10.1002/mrm.26289

Abstract

Purpose: To propose the technique multiband echo-shifted (MESH) echo planar imaging (EPI), which combines the principles of echo-shifted acquisition for two-dimensional multislice EPI, with both in-plane and multiband acceleration by means of partial parallel imaging techniques.
Methods: MESH EPI is suitable for functional MRI (fMRI) in situations where there is sufficient time to insert an additional EPI readout in the dead time between slice selection and the standard EPI readout. In such situations, MESH EPI can further accelerate data acquisition compared with standard multiband techniques. The method is particularly well suited for low static magnetic field strengths and lower spatial resolutions. We compared MESH with multiband and standard EPI with temporal signal-to-noise ratio (tSNR) measurements and resting state fMRI data.
Results: Results obtained at 1.5 T from healthy subjects revealed that the additional gradient switching did not additionally affect time course SNR over and above the reduction inherent to multiband imaging. Functional results were qualitatively similar between methods. MESH was not affected by the tSNR reduction and echo shifting gradients. The MESH data were acquired at a factor 2 or 3 faster than corresponding multiband acquisitions for echo shift factors of 1 and 2, respectively.
Conclusion: MESH can offer further acceleration of image acquisition for fMRI at no loss in sensitivity.

3.1. Introduction

Multiband (MB) imaging, also referred to as simultaneous multislice imaging, has rapidly established itself as a standard method for functional MRI (fMRI) and diffusion-weighted imaging of the brain [76][45][97], due in large part to the central role it has played in the Human Connectome Project [42]. It has also proven beneficial in a range of other applications, which together with acquisition and reconstruction techniques have been reviewed recently [8].

For functional MRI (fMRI) and other applications that require acquisition at a fixed echo time (TE) such as diffusion-weighted imaging MB imaging offers an acceleration factor that is given by the number of slices acquired simultaneously. The maximum acceleration factor is then constrained by the degree of g-noise present [123]. Use of the CAIPIRINHA (controlled aliasing in parallel imaging results in higher acceleration) technique [19], in the form of blipped-CAIPI [138] for echo planar imaging (EPI), can reduce the g-noise by shifting adjacent excited slices relative to each other in the phase encoding direction, and has established itself as a standard technique for MB imaging. The increase in acquisition speed through MB imaging has been shown to be beneficial for fMRI, primarily through the increased ability to reduce physiological noise [45][54][16]. Further acceleration beyond that already achieved by MB imaging would be possible through the incorporation of echo shifting techniques [98][157], reviewed by van Gelderen et al. [156], that eliminate the dead time between excitation and readout in blood oxygen level-dependent weighted EPI experiments. In the context of echo-shifted EPI, it is clear that this is only a realistic possibility if the condition $3 \times ETL < 2 \times TE$ is satisfied (where the echo train length [ETL] is the duration of the EPI readout), because only then will it be possible to introduce an extra EPI readout. For gradient echo (GE)-based fMRI, the optimal sensitivity is achieved when TE$\approx$T2*, thus imposing an additional constraint on the acquisition. An alternative way of using the dead time is to use multiecho EPI, but this approach provides additional information rather than an acceleration. For echo shifting to be feasible for most commonly encountered static magnetic field strengths and desired spatial resolutions, some degree of in-plane parallel imaging will have to be applied to shorten the ETL to meet the above requirements.

The most common technique for applying echo shifting is PRESTO [98][157]. This is generally applied in a 3D acquisition mode in which all radiofrequency (RF) pulses are applied to the same volume. Only low flip angles can be employed, and there is a danger of signal being generated from coherence pathways representing spin and stimulated echoes generated by the multiple

RF pulses used. An alternative echo-shifting approach was first proposed and demonstrated by Gibson et al. [50], who used slice-selective excitation in a standard two-dimensional (2D) EPI multislice acquisition such that after the excitation of one slice, the signal from another is read out. The advantage of this approach is that there is no direct constraint on the flip angles used, and the TE can be shifted by integer multiples of the interslice repetition time (TR). In the previous implementation, no partial parallel imaging was used, resulting in long TE acquisitions.
In this report, we explore the initial application of partial parallel imaging, both in-plane and in the slice direction, to 2D echo-shifted EPI, a technique we have termed multiband echo-shifted (MESH) EPI. We employed the relatively low static magnetic field of 1.5 T, as we can explore acquisition protocols using several echo shift (ES) factors at realistic TE values. We compared MESH with MB EPI and standard EPI with respect to temporal SNR and the sensitivity for measuring resting state networks (RSN).

3.2. Methods

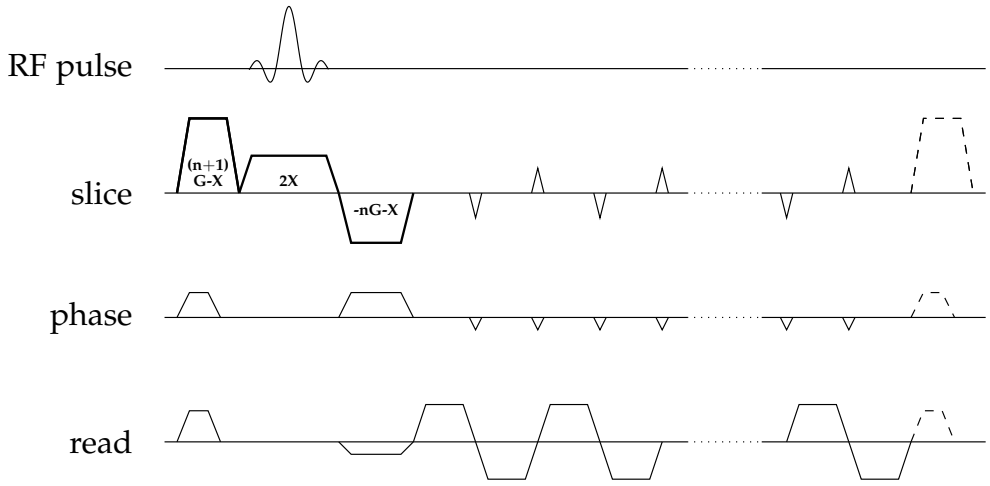

Figure 3.1: Echo shifting scheme. Two additional crusher gradients are implemented along the slice direction. $2X$ is the total gradient moment for the slice selection. The slice rephase gradient will then have a moment of $(nG_{shift} + X)$. The crusher before the excitation pulse will consist of a moment of $(n+1)G_{shift}X$. The gradients applied along the read- and phase-encoding axes just before each RF pulse are necessary to ensure that the total gradient along these axes is zero between successive RF pulses.

In order to obtain a multiband EPI (MB-EPI) and multiband echo-shifted EPI (MESH) sequence, a standard Siemens EPI sequence was modified as follows. For the MB-EPI sequence, standard

MB excitation pulses were incorporated. The MB pulses consist of complex-summed individually modulated RF pulses [76][97][100]. To improve the quality of the reconstruction of the aliased slices, blipped CAIPI [138] was also implemented, shifting individual slices in the field of view (FOV) along the phase-encode direction. To achieve the echo-shifting in the MESH sequence, two additional crusher gradients were implemented along the slice direction (figure 3.1). The slice rephase gradient after the excitation pulse dephases the magnetization by an additional factor of nG_{shift} where n is the number of echoes shifted and Gshift is the strength of the echo-shift gradient. If $2X$ is the total gradient moment for the slice selection gradient alone, then the slice rephase gradient will have a total gradient moment that is equal to $(nG_{shift} + X)$. Ultimately, the additional crusher before the excitation pulse will carry a moment of $(n + 1)G_{shift}X$, with the result that each additional slice gradient complex experienced by the transverse magnetization rephases it by a factor G_{shift}. In addition, rewinder gradients were applied along all three gradient axes after the EPI readout to ensure that the 0th moment of all the imaging gradients was zero in each TR period.

Data were collected from six healthy subjects using a 1.5 T Avanto scanner (Siemens Healthcare, Erlangen, Germany) with a 32-channel head coil after obtaining informed consent. For (tSNR) comparison, three protocols with two different effective TEs were compared: standard EPI, MB-EPI (MB factor 3, blipped CAIPI FOV/2 shift, no ES), and MESH (MB factor 3, blipped CAIPI FOV/2 shift, ES factors 1 and 2). To achieve an unbiased comparison, the TR was kept constant and the total number of slices was adjusted accordingly for each protocol. This way, the comparison was independent of the square root of TR corrections and effects arising from different Ernst angles. The two ES factors correspond to effective TEs of 30 and 49 ms. In order to minimize the interslice TR, no fat saturation was performed. The relevant acquisition parameters of the different protocols are shown in table 3.1.

For the resting state fMRI comparison, we compared standard EPI, MB-EPI, and MESH at a TE of 49 ms. All protocols had whole brain coverage and a total acquisition time of 7 min, for which the number of measurements was adjusted accordingly. The scan order was randomized. Furthermore, the flip angle (FA) was set to account for the different TR values. For all cases, it is slightly below the Ernst angle. The specific acquisition parameters are also shown in table 3.1.

Data were reconstructed offline with MATLAB (MathWorks, Natick, Massachusetts, USA). They were first reconstructed along the phase encoding direction with the GRAPPA algorithm (3×2 kernel) [55] with the autocalibration data (ACS lines) acquired prior to the MB acquisition within

Table 3.1: Acquisition parameters for ES 1 tSNR, ES 2 tSNR and ES 2 fMRI datasets.

ES 1 tSNR	**TR** (ms)	**TE** (ms)	**eff TE** (ms)	**ES**	**GRAPPA**	**MB**	**FA**	**BW** (Hz/px)	**slice gap**	**res** (mm)	**volumes**
EPI	232	30	30	0	3 (AP)	-	30°	2480	200%	3 iso	100
MB-EPI	232	30	30	0		3 (axial)			-		100
MESH	232	11	30	1		3 (axial)			-		100

ES 2 tSNR	**TR** (ms)	**TE** (ms)	**eff TE** (ms)	**ES**	**GRAPPA**	**MB**	**FA**	**BW** (Hz/px)	**slice gap**	**res** (mm)	**volumes**
EPI	232	49	49	0	3 (AP)	-	30°	2480	200%	3 iso	100
MB-EPI	232	49	49	0		3 (axial)			-		100
MESH	232	11	49	2		3 (axial)			-		100

ES 2 fMRI	**TR** (ms)	**TE** (ms)	**eff TE** (ms)	**ES**	**GRAPPA**	**MB**	**FA**	**BW** (Hz/px)	**slice gap**	**res** (mm)	**volumes**
EPI	2030	49	49	0	3 (AP)	-	74°	2480	-	3 iso	201
MB-EPI	688	49	49	0		3 (axial)	49°		-		600
MESH	232	11	49	2		3 (axial)	30°		-		1787

the same scan. This was followed by separation of the aliased slices with the leak-Block slice-GRAPPA algorithm (4×3 kernel) [26]. The reference data for the MB reconstruction was a single-volume standard EPI image with in-plane acceleration factor of 3. The tSNR maps were calculated from 100 time points by dividing the mean of the time series by the temporal standard deviation. The tSNR averages included all voxels within the individual brain masks.

MELODIC (FSL, http://www.fmrib.ox.ac.uk/fsl/) was used to perform Independent Component Analysis (ICA) on the group level RS data with 30 components and the following standard preprocessing steps: spatial smoothing (5 mm kernel), drift removal, MCFLIRT motion correction and registration to T1-weighted anatomical images. After dual regression analysis [138] with the eight most common RSNs (http://www.fmrib.ox.ac.uk/analysis/royalsoc8/) mixture modeling was applied to correct for inflated z-scores of low TR protocols. DICE scores [34][15] were calculated for all subjects and networks from the corresponding dual regression maps with the corrected thresholds.

3.3. Results

The reconstructed MB and MESH images are shown in figure 3.2 for two representative subjects. The corresponding tSNR maps appear next to the individual images for ES1 (above) and ES2 (below). tSNR dropped rapidly at the center of the brain for all cases due to the well-known

deterioration of sensitivity profiles with the increasing distance from the receiver coils [123].

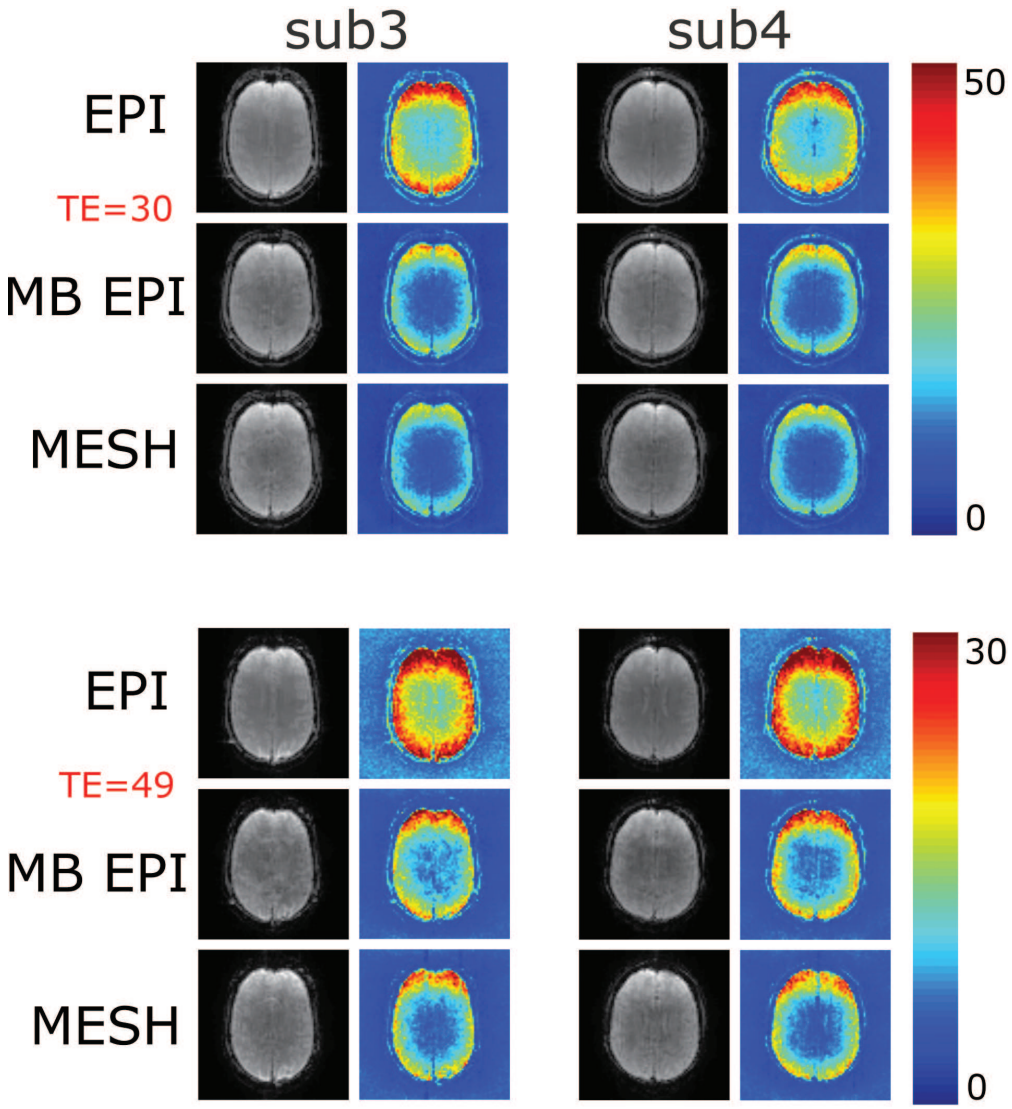

Figure 3.2: Single-slice example images and corresponding tSNR maps. Note the different maximum values set for tSNR maps of ES1 and ES2 cases. MB acquisition results in a tSNR drop. The introduction of echo shifting does not further decrease tSNR beyond that introduced by MB.

The mean tSNR values for all the subjects are listed in table 3.2 for a quantitative comparison. Two observations are noteworthy. First, there is no significant difference in tSNR between the standard MB-EPI (ES 0) and the corresponding ES 1 and ES 2 cases. Thus, the additional crusher gradients used for the echo shifting do not affect tSNR. The other important outcome concerns the decrease in tSNR with MB. Only the difference between columns 1 and 2 is significant for both ES factors. Standard group level RSNs such as visual, motor, default mode, and (fronto-)parietal obtained with the three protocols are shown in figure 3.3. Similarity of RSN maps between the protocols

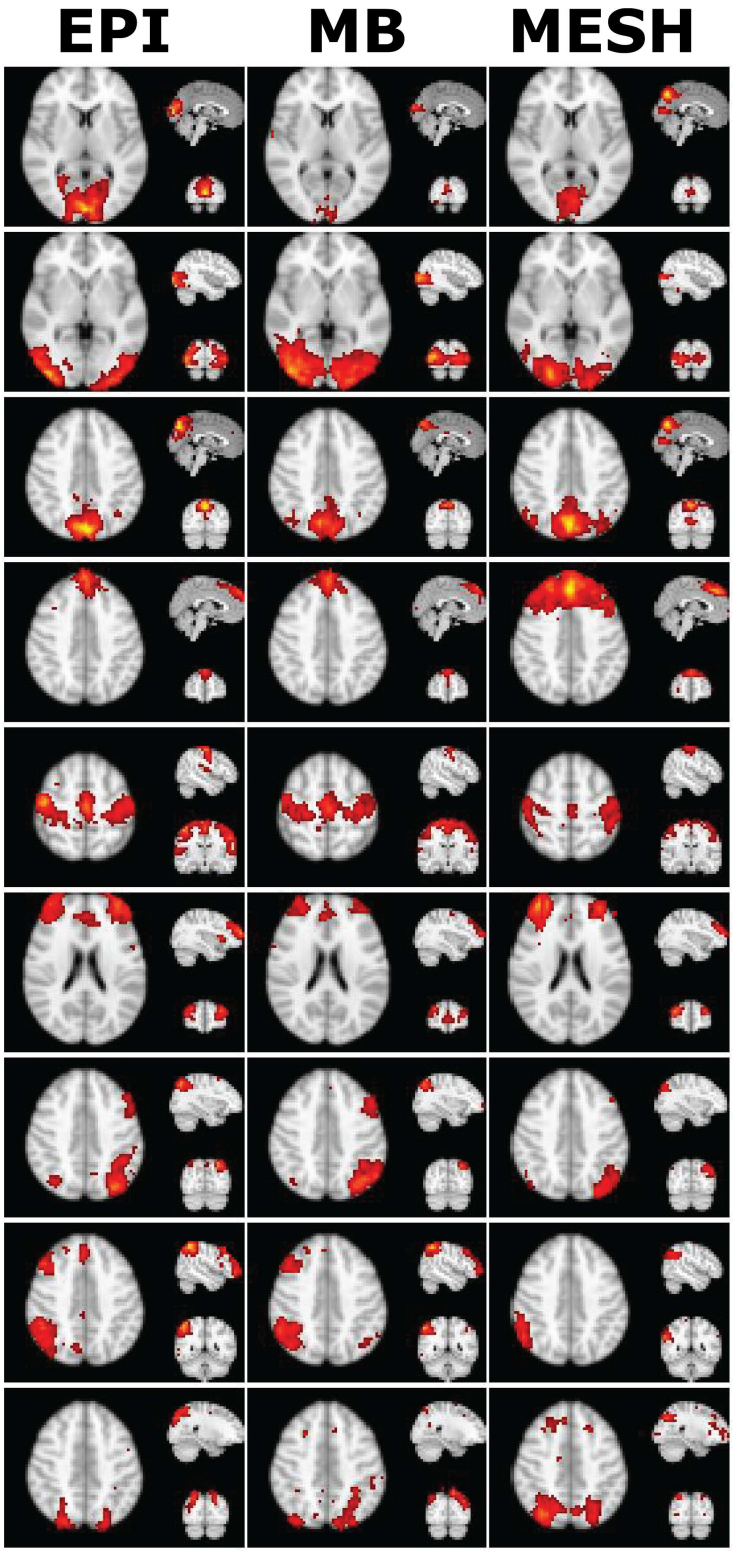

Figure 3.3: Standard RSNs from the group level ICA for all the protocols are shown in representative slices.

Table 3.2: Mean tSNR values for all subjects and acquisitions.

	TE = 30ms ES1			TE = 49ms ES2		
subject	**EPI**	**MB-EPI**	**MESH**	**EPI**	**MB-EPI**	**MESH**
1	13.1	9.3	9.5	11.1	9.6	8.3
2	22.9	13.7	15.2	19.3	10.9	11.5
3	25.8	15.7	14.1	19.4	12.7	11.6
4	24.4	15.9	14.5	19.1	12.9	11.5
5	22.1	14.9	15.7	20.8	11.3	11.6
6	23.2	13.2	12.9	17.2	10.2	9.4
average$\pm$std	21.9 ± 4.5	21.9 ± 4.5	21.9 ± 4.5	21.9 ± 4.5	21.9 ± 4.5	21.9 ± 4.5

indicates that functional results do not suffer from the reduced tSNR of MB and MESH. The DICE scores listed in table 3.3 quantitatively show the match between the subject level and the standard space for the eight most common RSNs. The DICE scores are similar to those reported in the literature [15][48]. Other than frontal (MESH versus standard EPI) and fronto-parietal (MESH and MB EPI versus standard EPI), the DICE score differences between the protocols are not significant. Dual regression maps provide the individual subject level results, which are linked to the same standard space maps and are therefore still comparable between methods. As an example, default mode network dual regression maps are illustrated in figure 3.4. Qualitatively, it can be seen that the maps are spatially similar but with increased average z scores for MESH.

3.4. Discussion

MESH combines MB, in-plane acceleration, and echo shifting. The dead time between the RF pulse and the echo is avoided, giving rise to significant reductions in volume TRs for some protocols. The true acceleration factors achieved in this study are listed in table 3.4. MESH fMRI data with ES 2 provide 3 or 9 times lower TRs with respect to MB EPI and EPI, respectively. The optimal contrast for fMRI with GE EPI is obtained when TE equals T2*. Consequently, low field strengths benefit more from MESH because the optimum echo times become considerably longer with the decreasing field strength. High-field ($\geq$7 T) acquisitions concentrate on high resolution, and thus longer readouts (ETLs).

The main benefit from MB imaging at constant TE is the high acceleration factors that are attainable, whereas for conventional acquisition schemes in-plane acceleration only results in marginal increases in speed. With MESH both in-plane and slice acceleration result in reduced acquisition

Table 3.3: DICE score results for all subjects and most commonly found 8 RSNs. Reported values are comparable with those reported in the literature. Significant differences of MESH vs standard EPI are marked with *.

	visual medial			**default mode**		
subject	**EPI**	**MB-EPI**	**MESH**	**EPI**	**MB-EPI**	**MESH**
1	0.43	0.40	0.49	0.22	0.37	0.34
2	0.42	0.30	0.41	0.45	0.37	0.44
3	0.47	0.44	0.55	0.25	0.37	0.37
4	0.23	0.45	0.32	0.24	0.05	0.13
5	0.13	0.43	0.46	0.41	0.32	0.33
6	0.45	0.27	0.41	0.26	0.34	0.33
average±std	0.36±0.14	0.38±0.08	0.44±0.08	0.31±0.10	0.30±0.12	0.32±0.10

	visual lateral			**frontal**		
1	0.10	0.28	0.41	0.18	0.18	0.30
2	0.18	0.25	0.37	0.10	0.15	0.17
3	0.33	0.42	0.34	0.11	0.15	0.33
4	0.22	0.14	0.08	0.04	0.19	0.12
5	0.25	0.37	0.38	0.14	0.14	0.14
6	0.34	0.32	0.39	0.14	0.14	0.21
average±std	0.24±0.09	0.30±0.10	0.33±0.12	0.12±0.05	0.16±0.02	0.21±0.09*

	auditory			**fronto-parietal (right)**		
1	0.27	0.16	0.28	0.30	0.07	0.37
2	0.15	0.08	0.17	0.27	0.33	0.13
3	0.32	0.21	0.36	0.30	0.24	0.19
4	0.10	0.05	0.01	0.27	0.16	0.14
5	0.27	0.25	0.36	0.31	0.25	0.30
6	0.08	0.23	0.16	0.19	0.27	0.29
average±std	0.20±0.10	0.16±0.08	0.22±0.14	0.28±0.04	0.22±0.09	0.24±0.10

	sensory motor			**fronto-parietal (left)**		
1	0.22	0.47	0.51	0.20	0.36	0.39
2	0.50	0.27	0.51	0.07	0.34	0.34
3	0.43	0.54	0.42	0.35	0.31	0.35
4	0.07	0.23	0.44	0.02	0.23	0.16
5	0.39	0.29	0.26	0.29	0.36	0.40
6	0.47	0.46	0.33	0.08	0.31	0.42
average±std	0.35±0.17	0.38±0.13	0.41±0.10	0.17±0.13	0.32±0.05*	0.34±0.09*

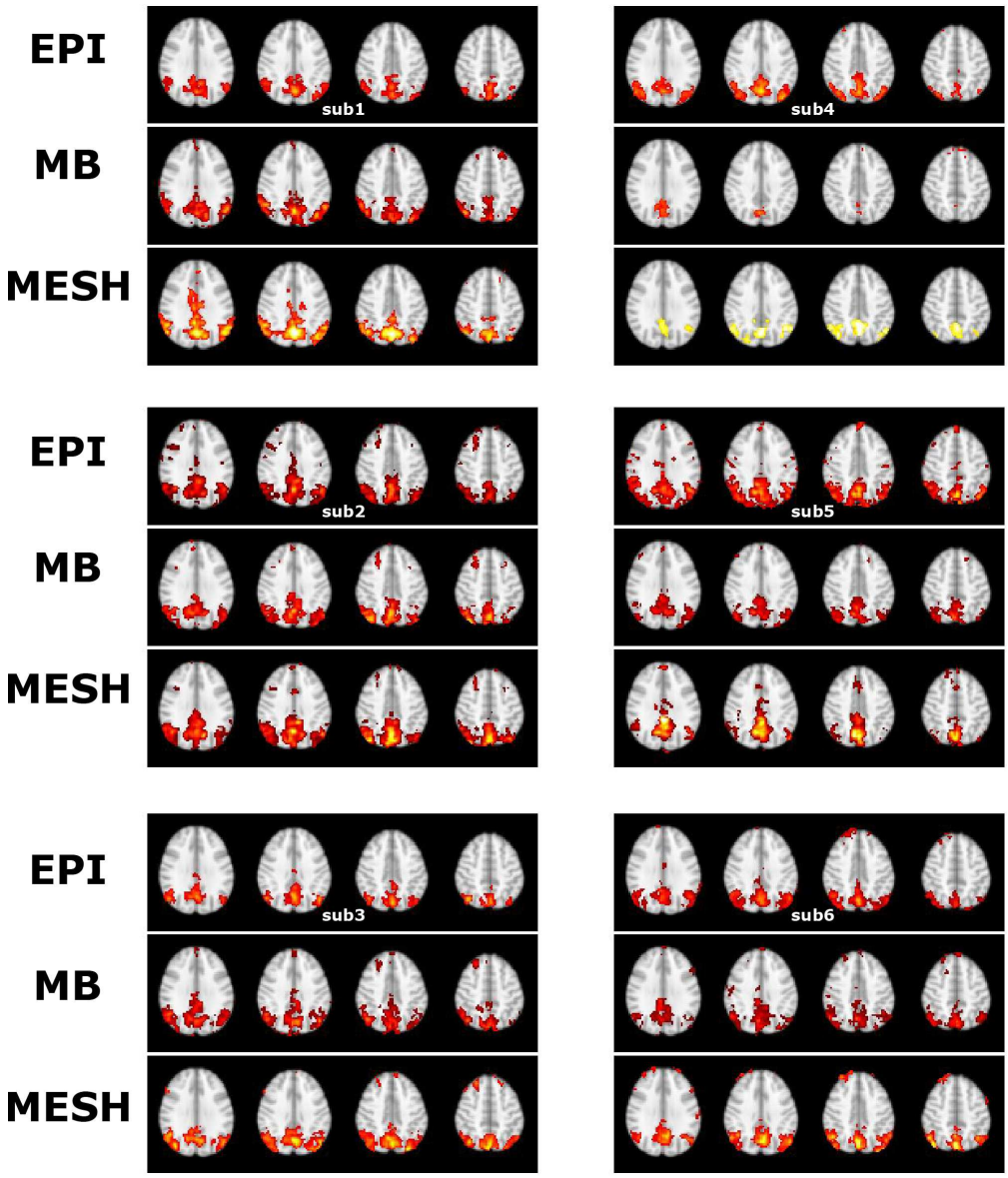

Figure 3.4: Dual regression maps for default mode network are overlaid on MNI standard space images for four representative slices. Note the increased z scores for MESH. Thus, mixture modeling is crucial to estimate the true thresholds for a fair comparison.

Table 3.4: Number of slices per unit time and the corresponding true acceleration factors with respect to standard EPI.

	ES 1			ES 2		
	EPI	**MB-EPI**	**MESH**	**EPI**	**MB-EPI**	**MESH**
number of slices	6	18	36	4	12	36
acceleration factor	1	3	6	1	3	9

times: in the former case by increasing the ES factor that can be employed. Multiband acceleration reduces the time spent on slice selection and hence always accelerates the total acquisition. In-plane acceleration instead of MB acceleration will reduce the ETL but increase the fraction of time spent on slice selection. In-plane acceleration does however have the additional benefit of reducing distortion. As ever, the total acceleration factor is limited by g-noise to a value of less than about ten.

The fact that there is no significant difference between MB EPI and MESH for ES 1 and 2 suggests that the further addition of echo-shifting to MB acquisition does not reduce tSNR. In fact, the drop in tSNR happens when MB is introduced (table 3.2). This confirms that the tSNR drop is purely due to the nature of MB reconstruction [28]. The tSNR maps of whole brain MB and MESH fMRI data, with square root of TR correction, are compared in figure 3.5. It can be observed that there is no discernible effect of the echo shifting between different brain regions. Recent advances in the acquisition of calibration scans for EPI [119] and MB image reconstruction [72] could potentially further improve the tSNR maps. MESH RS results are qualitatively similar to MB EPI on the group and subject level, providing further evidence that echo shifting gradients do not have any additional negative effect on data quality. The increases in z scores obtained with MESH compared with MB are in line with those previously reported for MB compared with standard EPI [45].

PRESTO and its variant 3D echo shifting sequences are known to produce ambiguous contrast images, but this is avoided with 2D echo shifting [50] and hence with MESH. With volume TR > T2, MESH images will have standard GE EPI (T2*) contrast (as seen in example images of figure 3.1) unless the sequence is pushed to the limit such that the TR becomes comparable to T2. Similarly, the motion sensitivity of PRESTO, expressed as ghosting and blurring in the whole 3D image and phase instability between the echoes, is essentially a feature of 3D acquisition and does not apply to MESH [50].

Echo shifting has also been combined with inverse imaging methods to provide highly accelerated acquisition [83][27]. Other recent developments provide improved spatial resolutions with whole brain TRs shorter than 100 ms using inverse imaging [14] and stacks of spirals [3]. Combined EEG-fMRI [79] and resting state frequency studies [15] are typical applications of such ultrafast techniques, but at present the effective spatial resolution and stability of such methods is inadequate for standard fMRI studies. As shown in table 3.5, low spatial resolution studies with MESH can enable volume TRs that are not much greater than these ultrafast techniques,

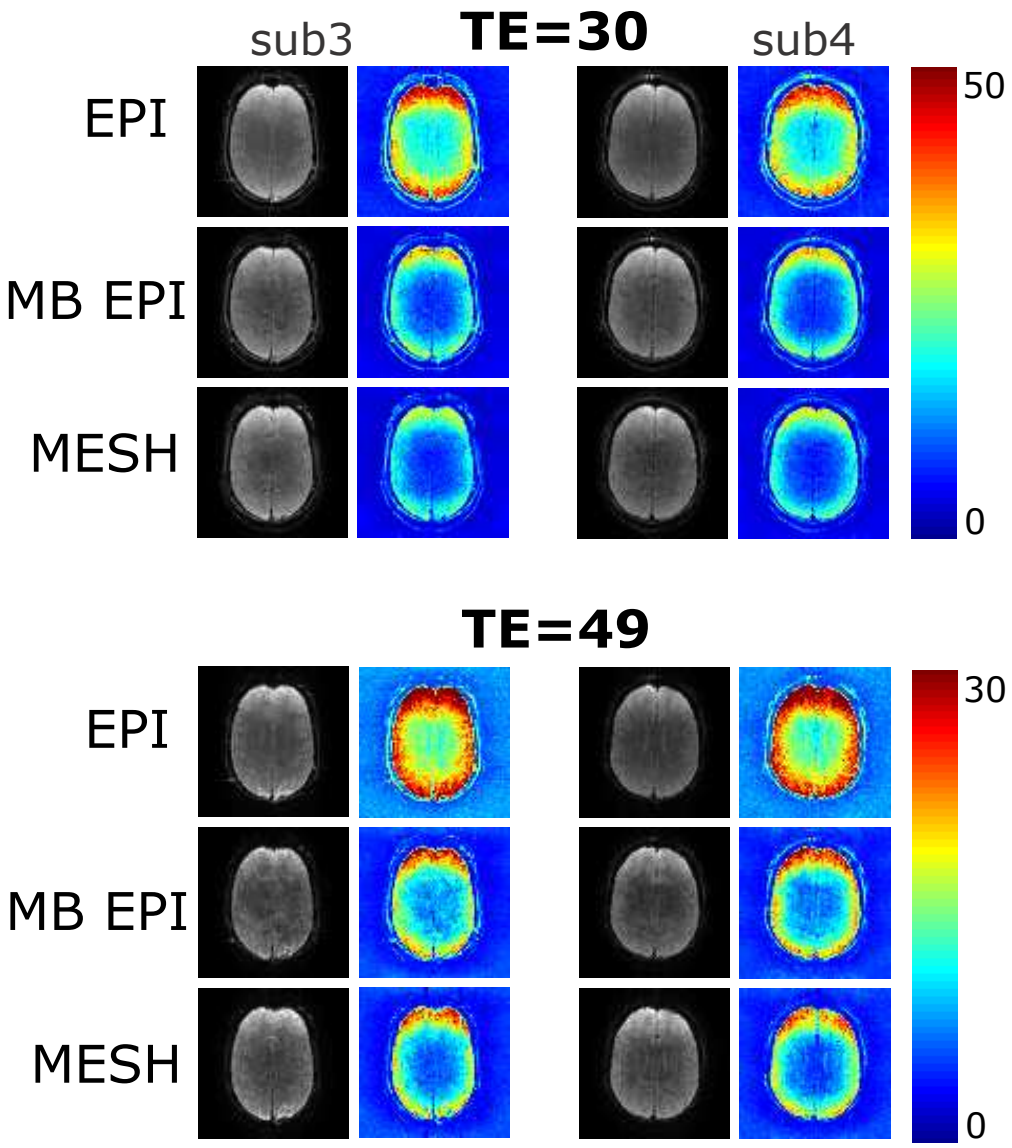

Figure 3.5: tSNR maps of whole brain EPI, MB, and MESH fMRI data with square root of TR correction. Similar tSNR values between different brain regions for MESH prove that the additional gradients do not have spatially varying effects on the image quality.

Table 3.5: The acquisition parameters with lower resolution MESH. Please note the same volume TRs are possible with effective TEs of 30 and 49 with echo shift factors of 1 and 2, respectively.

isotropic resolution (mm)	**volume TR** (ms)	**FOV read & phase** (mm)	**number of slices**	**coverage in slice direction** (mm)
3	232	216	36	108
4	155	216	27	108
5	117	220	21	105

opening up the possibility of short TR acquisitions without the need for complex reconstruction algorithms. Moreover, unlike inverse imaging-based methods, MESH provides homogeneous spatial resolution. The second regression of the dual regression process is effectively a GLM with the time course of the RSN acting as a regressor. This provides an illustration as to how MESH would perform with task fMRI. As expected from any lower TR fMRI protocol, z scores are increased with MESH without any visible artifacts.

In conclusion, in favorable circumstances, MESH offers a further acceleration in image acquisition for fMRI at no loss in sensitivity compared with MB. Future work will explore its use at 3T, the benefits for low TR imaging, and the ideal combinations of in-plane and MB acceleration factors.

Chapter 4

Whole brain, high resolution multiband spin-echo EPI fMRI at 7T: A comparison with gradient-echo EPI using a color-word Stroop task

Rasim Boyacioğlu[1], **Jenni Schulz**[1], Nils CJ Müller[1], Peter J Koopmans[1,2], Markus Barth[1,2], David G Norris[1,2]

[1]Donders Institute for Brain, Cognition and Behaviour, Radboud University Nijmegen, The Netherlands

[2]Erwin L. Hahn Institute for Magnetic Resonance Imaging, University Duisburg-Essen, Essen, Germany

Neuroimage (2014);97:142-50. doi: 10.1016/j.neuroimage.2014.04.011

Abstract

A whole brain, multiband spin-echo (SE) echo planar imaging (EPI) sequence employing a high spatial (1.5 mm isotropic) and temporal (TR of 2 s) resolution was implemented at 7T. Its overall performance (tSNR, sensitivity and CNR) was assessed and compared to a geometrically matched gradient-echo (GE) EPI multiband sequence (TR of 1.4 s) using a color-word Stroop task. PINS RF pulses were used for refocusing to reduce RF amplitude requirements and SAR, summed and phase-optimized standard pulses were used for excitation enabling a transverse or oblique slice orientation. The distortions were minimized with the use of parallel imaging in the phase encoding direction and a post-acquisition distortion correction. In general, GE-EPI shows higher efficiency and higher CNR in most brain areas except in some parts of the visual cortex and superior frontal pole at both the group and individual-subject levels. Gradient-echo EPI was able to detect robust activation near the air/tissue interfaces such as the orbito-frontal and subcortical regions due to reduced intra-voxel dephasing because of the thin slices used and high in-plane resolution.

4.1. Introduction

Functional magnetic resonance imaging (fMRI) with blood oxygenation level dependent (BOLD) contrast has been the most popular tool for mapping brain activation for the neuroscience community for more than two decades. [109] The BOLD contrast results from the interplay between cerebral blood volume, blood flow, and oxygen consumption: all triggered by the underlying neuronal activity. The BOLD response is generated by four possible contrast mechanisms, namely extravascular dynamic/static dephasing and intravascular dynamic/static dephasing, the relative contributions of which depend on main magnetic field strength (B0), spatial resolution and vessel size. It is widely accepted that the extravascular component becomes much more prominent at high field (7T or above). [36][108] Spin-echo (SE) based sequences refocus the static effects, and the transverse relaxation time, T2, of venous blood shortens very rapidly with increasing field strength. At 7T it is very short ($\sim$ 10-15ms) compared to the optimal (for gray matter) echo times (TE) of SE echo planar imaging (EPI) sequences at high field. [80][153] This suggests that the SE EPI BOLD response at 7T originates solely from the extravascular dynamic dephasing component and thus, from capillaries and smaller post capillary vessels. Given that gradient echo (GE) EPI BOLD contrast is augmented by the dephasing from the venous blood (draining vessels), GE EPI and SE EPI have been labeled as being more sensitive and more specific to the true site of neuronal activation, respectively [104], [111], [113], [155] and [166].

Similar to BOLD contrast mechanisms, the noise characteristics of SE and GE EPI are also complex and differ from each other. Acquisition parameters (TE, voxel volume) and the field strength play a major role in the effect size of the physiological component (breathing, heart beat) of the noise. It is well established for GE EPI that with increasing field strength and voxel volume the physiological noise dominates over the thermal noise. [150] Triantafyllou et al. have also demonstrated almost the same behavior for SE EPI as GE EPI at 3 and 7T with different coils and spatial resolutions [151]. However, in an earlier study it was suggested that in a SE EPI experiment the ratio between physiological and thermal noise is independent of the voxel size. [166]

Even though multiband (also called simultaneous multi-slice, SMS) imaging was first proposed [76] shortly after the now commonly used parallel imaging techniques (GRAPPA ([55]), SENSE [123] and SMASH [141]), it took almost a decade to receive any attention and interest from the MR community. [45][97] Multiband imaging provided the opportunity for 2D sequences to accelerate in the slice direction by acquiring data from N slices simultaneously without the penalty of a

$\sqrt{N}$ reduction in signal to noise ratio (SNR). Initially an image domain reconstruction similar to SENSE was used for multiband reconstruction [76]; however, recently the slice GRAPPA algorithm with the blipped CAIPIRINHA approach [138] has proven to be very useful in facilitating an improved reconstruction by making use of the coil sensitivity information in the unaccelerated direction. However, one has to be careful in choosing the right combination of acceleration and shift factors. [139]

Common multiband RF pulses are the complex sums of the individual RF pulses of each of the excited slices . [92][100] For non-overlapping slices the RF amplitude and power needed are linearly proportional to the number of slices excited simultaneously. Evidently, this poses problems for SE EPI at high field due to the high specific absorption rate (SAR) of the refocusing pulses. Recently, to overcome this SAR limitation problem, Power Independent Number of Slices (PINS) pulses [102] were introduced and have been used in a high resolution SE EPI resting state (RS) study at 7T [71], with Turbo Spin Echo (TSE) imaging of the head at 3 and 7T [101] and for high spatial resolution DWI also at 7T [39]. Due to the periodic excitation profile of the PINS pulses, a sagittal acquisition scheme was adopted for the SE EPI RS study. We have implemented a high spatial and temporal resolution SE EPI sequence by employing standard multiband pulses for excitation and PINS pulses for refocusing, so that the acquisition in any slice orientation is possible. It is thus now possible to perform whole brain SE EPI at 7T with good spatial and temporal resolution. It is hence highly relevant to examine the relative overall performance of GE and SE EPI at 7T in order to make an informed choice of pulse sequence for performing standard activation studies (i.e. excluding specialized studies of cortical layers or columns).

It is generally accepted that GE is more sensitive than SE, and this has indeed been shown in a few studies at 7T and above. [21][58] However, there are also many studies that argue that SE should be the method of choice at 7T because of its better spatial specificity [166][167][111] and for a detailed review see reference [104]). With the relatively new possibility to perform high resolution, whole brain SE-EPI without SAR constraints the researcher has the flexibility to also use a SE-EPI protocol at 7T for a cognitive neuroscience study. Hitherto such comparisons have not been in the whole brain and have been confined to regions where a priori strong stimulus evoked response could be expected. Rather than proving the well studied specificity of SE, we investigated the general applicability of SE-EPI at high field using a standard cognitive task that elicits widespread activity throughout the whole brain. With lower levels of signal change it might not be possible with SE EPI to detect activation with demanding cognitive paradigms.

Another point not discussed in the literature [21][58] is the origin of activated SE EPI voxels that are incongruent to GE EPI. The incongruent GE voxels are easily identified and labeled as coming from veins but it is not so clear for SE incongruent voxels: fueling the suspicion that SE EPI is vulnerable to CSF signal and inflow effects. We hence also implemented a matched multiband GE EPI sequence and compare here the two pulse sequences in terms of signal and noise levels, sensitivity and contrast to noise ratio (CNR) using a color-word Stroop functional paradigm. The Stroop task generates activation in a broad range of brain regions including the orbito-frontal areas where SE EPI has previously been found to outperform GE EPI at lower static magnetic field strengths and coarser spatial resolutions. [106][136] We chose to perform the experiments at a nominal spatial resolution of 1.5mm, as this is finer than the expected width of the hemodynamic response function at this field strength for both gradient- and spin-echo [41]; see reference [103] for review.

4.2. Theory and Methods

4.2.1. Acquisition

Data were collected from 6 healthy subjects (4 male, 2 female, age 25.8 $\pm$ 3.4 years) after obtaining informed consent, using a 7T Magnetom scanner (Siemens Healthcare, Erlangen, Germany) with a 32 channel head coil (Nova Medical, Wilmington, USA). Prior to the functional GE EPI and SE EPI scans, 5 matched reference scans with full FOV and without multiband acceleration were obtained for the estimation of the reconstruction kernel in the phase encoding (PE) and slice direction. Geometrical parameters were kept identical between SE EPI and GE EPI such as: FOV 224$\times$224 mm^2, 69 slices, PE direction AP, in-plane acceleration factor (AF) 3, multiband factor 3, bandwidth 1960 Hz/Px, resolution 1.5$\times$1.5$\times$1.3 mm^3, slice gap 15%, matrix 150$\times$150. We have used almost the same parameters as a previous multiband SE EPI study with PINS pulses [71]. The TE for SE EPI is close to gray matter T2 [30] which is the widely accepted optimal value. It has recently been shown that large variations in echo times lead to no change in BOLD signal change for short readouts (similar to this study, optimal due to reduced T2* weighting, Fig. 4.6b of [21]). Table 4.1 shows the remaining acquisition parameters of SE EPI and GE EPI scans. Structural scans for 5 subjects were obtained using MP2RAGE [91] with the following parameters: matrix 256$\times$240$\times$160, resolution 1$\times$1$\times$1 mm^3, acquisition time 10:42s, flip angles 4°and 6°, inversion

times 900ms and 3200ms, TE 1.89ms, TR 5000ms, bandwidth 240 Hz/Px. The structural scan of one subject was already available from a 3T scanner (Tim Trio, Siemens Healthcare, Erlangen, Germany) with matrix size 256×256×192, resolution 1×1×1 mm^3, acquisition time 5:21s, flip angle 8°, inversion time 1100 ms, TE 3.03ms, TR 2300ms, bandwidth 130 Hz/Px.

Table 4.1: Acquisition parameters of SE EPI and GE EPI.

	TR (s)	TE (ms)	excitation FA	BW (Hz/px)	SAR	# of volumes
SE SMS	1.97	53	130	1960	92%	206
GE SMS	1.39	27	40	1960	47%	300

In a previous study [71], PINS pulses were employed in a SE EPI sequence both for excitation and refocusing. This excludes slice orientations having a gradient component along the z-axis (i.e. only coronal or sagittal slice orientations are permitted) as otherwise signals from the neck region, and possibly beyond, will contribute to the aliased slice due to the infinite excitation profile of PINS pulses. In this study, we have used standard (summed) multiband pulses for excitation and PINS pulses for the refocusing of the SE sequence, enabling axial slice orientation. The phases of the individual excitation pulses have been optimized to reduce the peak power. [53][61] PINS pulses consist of a series of RF hard pulses interleaved with slice selective gradient blips. Each individual blip de-phases the signal by 2π over the defined slice spacing creating a periodic slice profile. The amplitude of each hard pulse can be determined by a Fourier series expansion of the desired slice profile. Although periodicity seems to imply an infinite number of slices, this is in practice limited by the extent of the subject or the transmit/receive volumes of the coils. Compared to a single slice pulse, there is some increase in SAR for PINS when using the same pulse duration. [102] This arises from spending some time of the RF duration only on gradient switching instead of RF transmission. However, this increase is significantly smaller than the increase in power deposition of a conventional summed multiband pulse which is proportional to the number of simultaneously excited slices. Due to slew rate limitations, PINS pulses have a relatively low bandwidth-time product (BWTP). To compensate for this, RF pulse durations of 7.68ms were used for all RF pulses in order to achieve the desired slice thickness of 1.3 mm. This allowed for 31 PINS sub-pulses resulting in a BWTP of 1.12 which was matched to the standard multiband pulses.

4.2.2. Reconstruction and registration

The reconstruction was performed offline in MATLAB. First, both the reference data and the multiband data were unfolded in the phase encoding direction with the GRAPPA algorithm (5×4 kernel) [55]. Then, multiplexed slices were unaliased with the SENSE-GRAPPA algorithm (3×2 kernel) [11]. The mean of the reconstructed EPI volumes was coregistered to the corresponding anatomical scan using an in-house developed distortion correction and coregistration algorithm for each subject [160], which simultaneously estimates the transformation matrices in all directions: non-linear in the AP PE direction (deformation due to EPI) and linear in the other directions (rigid-body) [146]. The degree of distortion and the corrected mean images for SE EPI and GE EPI for a representative subject can be seen in Fig. 4.1 and Fig. 4.2, respectively.

4.2.3. Functional task and analysis

The functional task was the same for SE EPI and GE EPI scans: the color-word interference Stroop task, which is widely used by the neuroscience community and known to induce consistent (de-)activation in the whole brain and especially in orbito-frontal regions. For each trial (1.5s), two words were presented above each other on a gray screen (in text: blue, red, green or yellow), the one below in black and the one above in color (blue, red, green, or yellow). The subjects were told to press a button when the meaning of the word in black (below) was matched by the color of the above word, regardless of its meaning. There were 10 ON blocks (30s, 20 trials) in each run with an initial 20s and 10 other (10s) OFF blocks in-between. During the OFF blocks subjects were told to fixate on a red cross at the center of the screen. The total duration of each run was 7min and the order of acquisition was alternated between subjects to counter balance habituation effects. Thus, three subjects started with SE EPI scan and then GE EPI while the other three first performed the task while being scanned with GE EPI and then SE EPI.
The functional analysis was carried out with FEAT (v5.98, http://www.fmrib.ox.ac.uk/fsl/) with the following preprocessing steps: spatial smoothing (3 mm kernel), drift removal, MCFLIRT motion correction and prewhitening. Higher-level analysis was carried out using FLAME (FMRIB's Local Analysis of Mixed Effects) stage 1 and stage 2. [9][164][165] Z (Gaussianised T/F) statistic images were thresholded using clusters determined by $Z > 2.3$ and a (corrected) cluster significance threshold of $p = 0.05$.

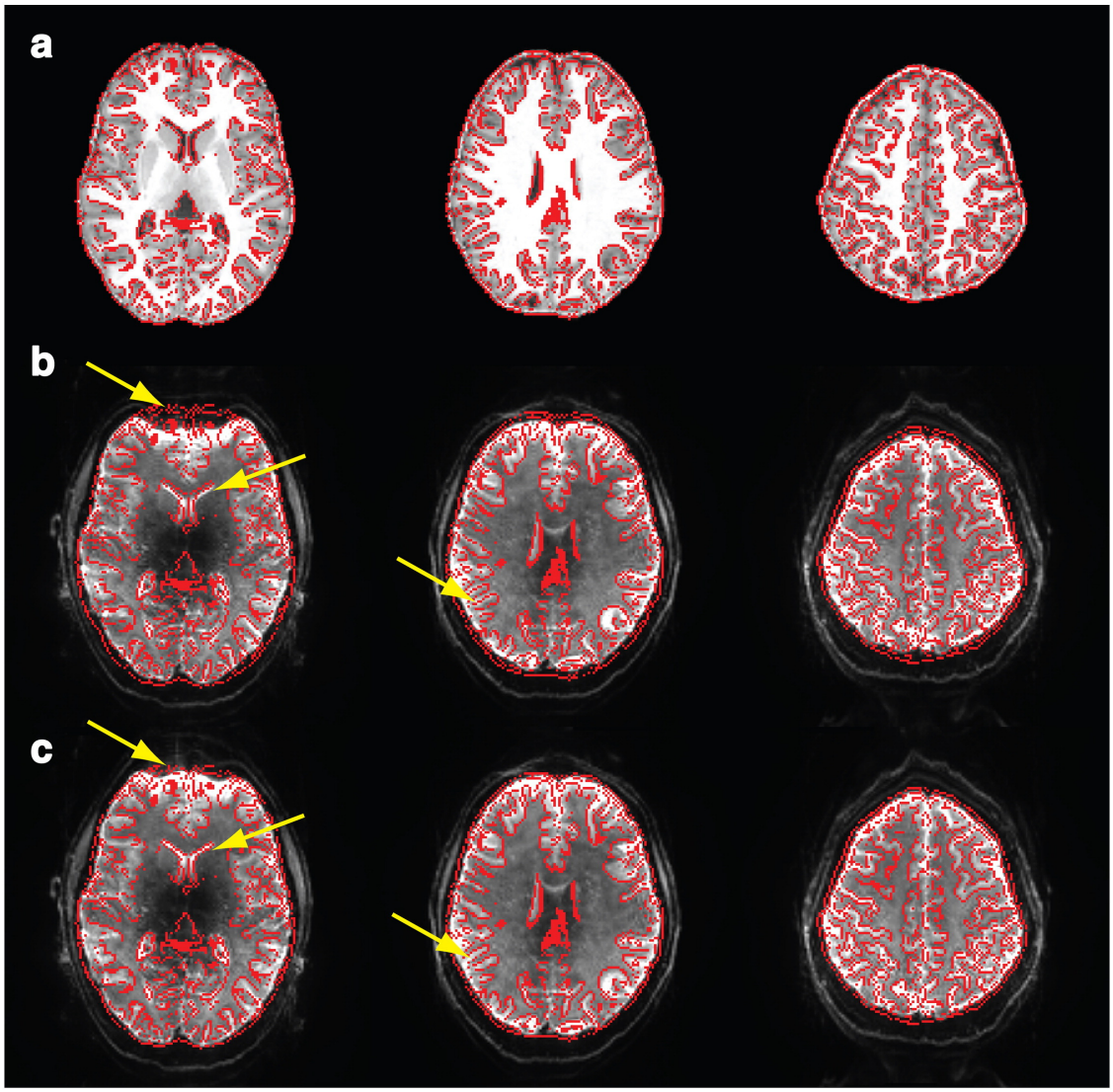

Figure 4.1: Three slices from (a) anatomical T1, (b) SE EPI mean raw and (c) distortion corrected volumes. The frontal and occipital regions benefit the most from distortion correction. Note the improvement in areas depicted by the yellow arrows.

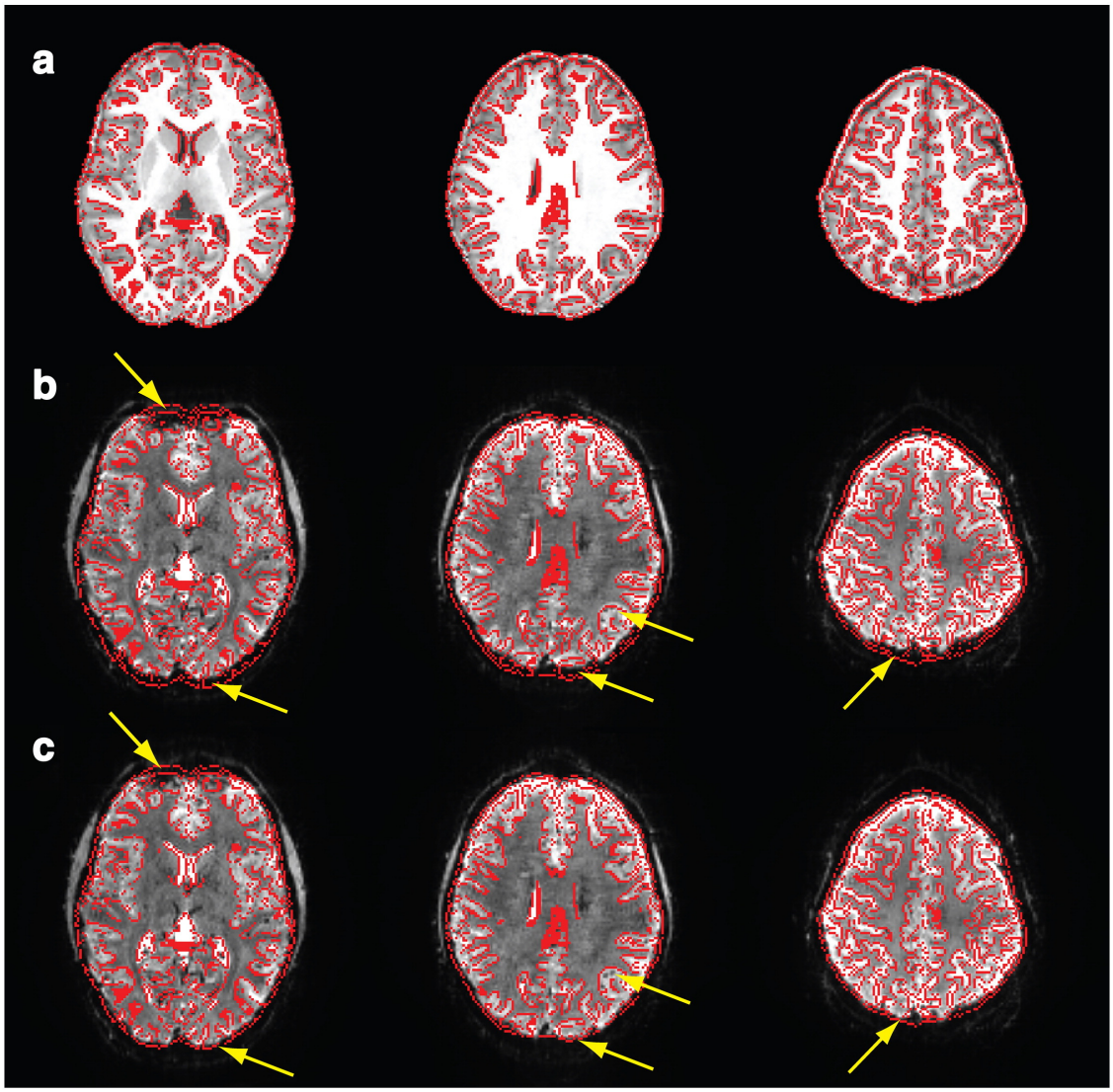

Figure 4.2: Three slices from (a) anatomical T1, (b) GE EPI mean raw and (c) distortion corrected volumes. The frontal and occipital regions benefit the most from distortion correction. Note the improvement in areas depicted by the yellow arrows.

The temporal signal to noise ratio (tSNR) maps were corrected for different TRs of SE and GE EPI to obtain sequence efficiency. In other words, tSNR of a voxel is its mean divided by the standard deviation and the square root of the TR of the sequence. Contrast to noise ratio (CNR) maps were obtained from the z-score statistical maps considering the accurate transition of individual subject results to the group level (with FLAME 1 + 2). The regions having higher z-score (for both contrasts combined) for one modality compared to the other one were mapped for both GE and SE EPI. The individual subject and group results were masked with the brain masks obtained from the mean EPI image and the MNI template, respectively. The percentages of activated voxels for SE and GE EPI in the gray matter, white matter and CSF were calculated with the following pipeline. The tissue masks were obtained by segmenting the structural scan with FSL's FAST (http://www.fmrib.ox.ac.uk/fsl/FAST) after mapping it onto the functional space. Subject specific statistical thresholds were calculated with mixture modeling with the assumption that false positives are more prominent than false negatives.

4.3. Results

Reconstructed SE EPI and GE EPI single time point images of a representative subject are shown in Fig. 4.3. SE EPI suffers from reduced signal intensity at the center of the brain due to B1 inhomogeneity, whereas it is superior to GE EPI in recovering the signal in the orbito-frontal areas. The signal losses can also be observed from the mask (see the first slice of the GE EPI and central regions of SE EPI) applied to the tSNR maps of the corresponding slices shown in Fig. 4.4. GE EPI has higher tSNR with respect to SE EPI in the whole brain for the single subject case and in the group average. Fig. 4.5 shows that the superior tSNR of GE EPI also translates to higher

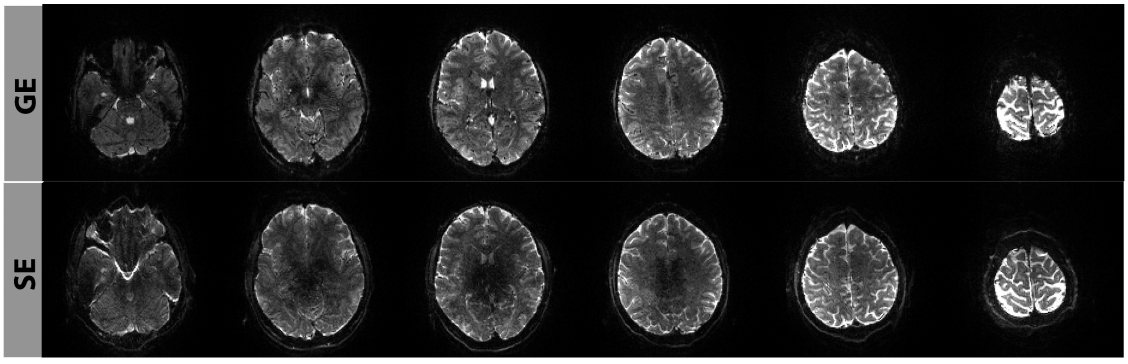

Figure 4.3: GE EPI and SE EPI single time point images of a representative subject.

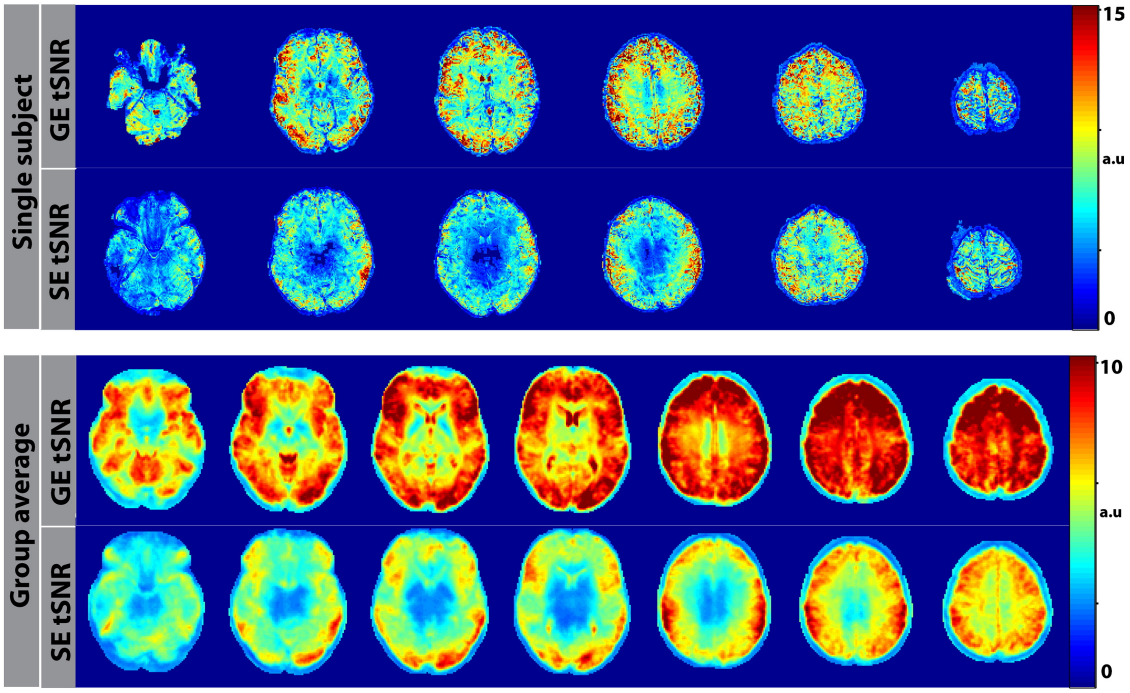

Figure 4.4: Single subject and group average tSNR maps in arbitrary units. GE has, in general, higher tSNR.

functional sensitivity compared to SE EPI. Numbers of (de)activated voxels and the maximum z-scores in the group level are listed in Table 4.2. GE EPI is able to detect whole brain activation (red-yellow) and deactivation (blue) including in problematic regions such as the orbito-frontal regions and hippocampus. However, SE EPI surprisingly has comparable sensitivity within the visual cortex. For comparison, the activated regions where GE EPI and SE EPI perform better in terms of CNR are plotted in Figs. 4.6a and b respectively. Except for some parts of the visual cortex and (superior) frontal pole, GE EPI has higher CNR. In addition, the signal change (ΔS) and the noise (σ) levels for SE and GE EPI can be seen in Fig. 4.7. GE EPI has considerably higher signal change but also higher noise in the visual areas. The number and percentages of activated voxels for SE and GE EPI in different tissue compartments are listed in Table 4.3. Comparing the ratios, GE EPI has significantly less ($p < 0.05$) activation in CSF and significantly more ($p < 0.05$) activation in the gray matter.

4.4. Discussion

SE EPI at high field is challenging to perform mainly due to SAR limitations leading to partial brain coverage and/or increased TR. SE EPI with multiband approaches only exacerbates the

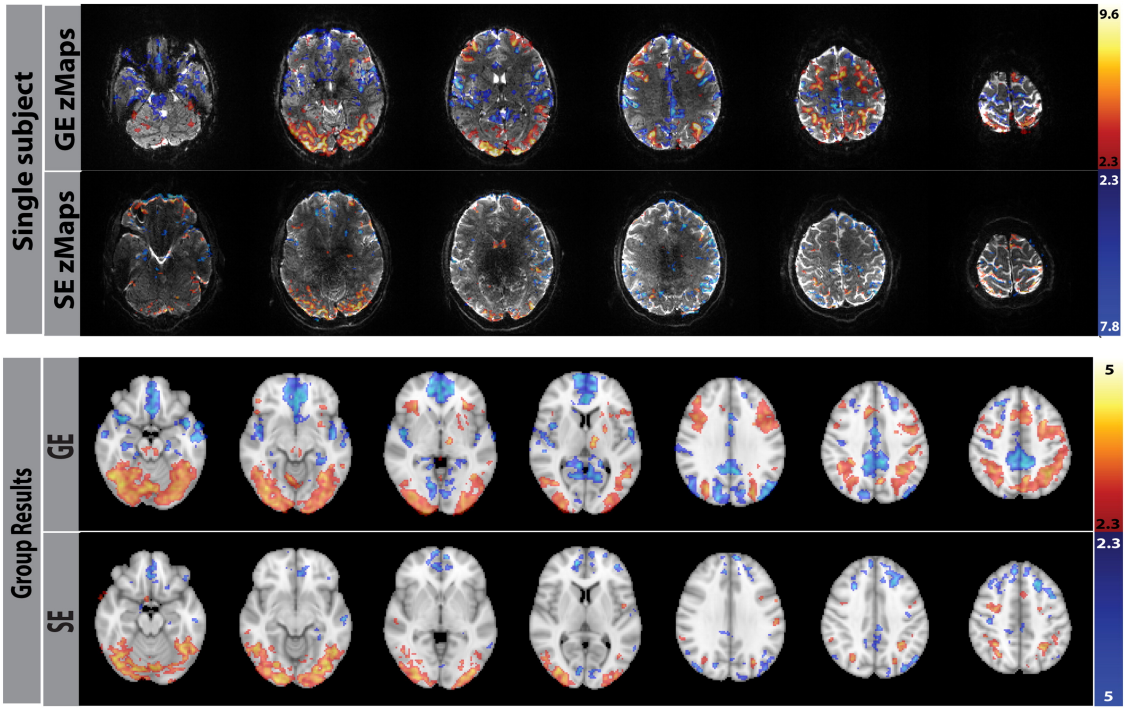

Figure 4.5: Z-score maps of the Stroop task for GE EPI and SE EPI for a representative single subject and at the group level. Two contrasts, activation (red-yellow) and deactivation (blue) are shown. Overall, GE EPI has higher sensitivity compared to SE EPI.

Table 4.2: Group level cluster sizes and maximum z-scores for GE and SE EPI.

	SE EPI	GE EPI
# of activated voxels	6703	10.750
# of deactivated voxels	2729	10.753
max. z-score of activated voxels	5.37	4.98
max. z-score of deactivated voxels	4.45	5.13

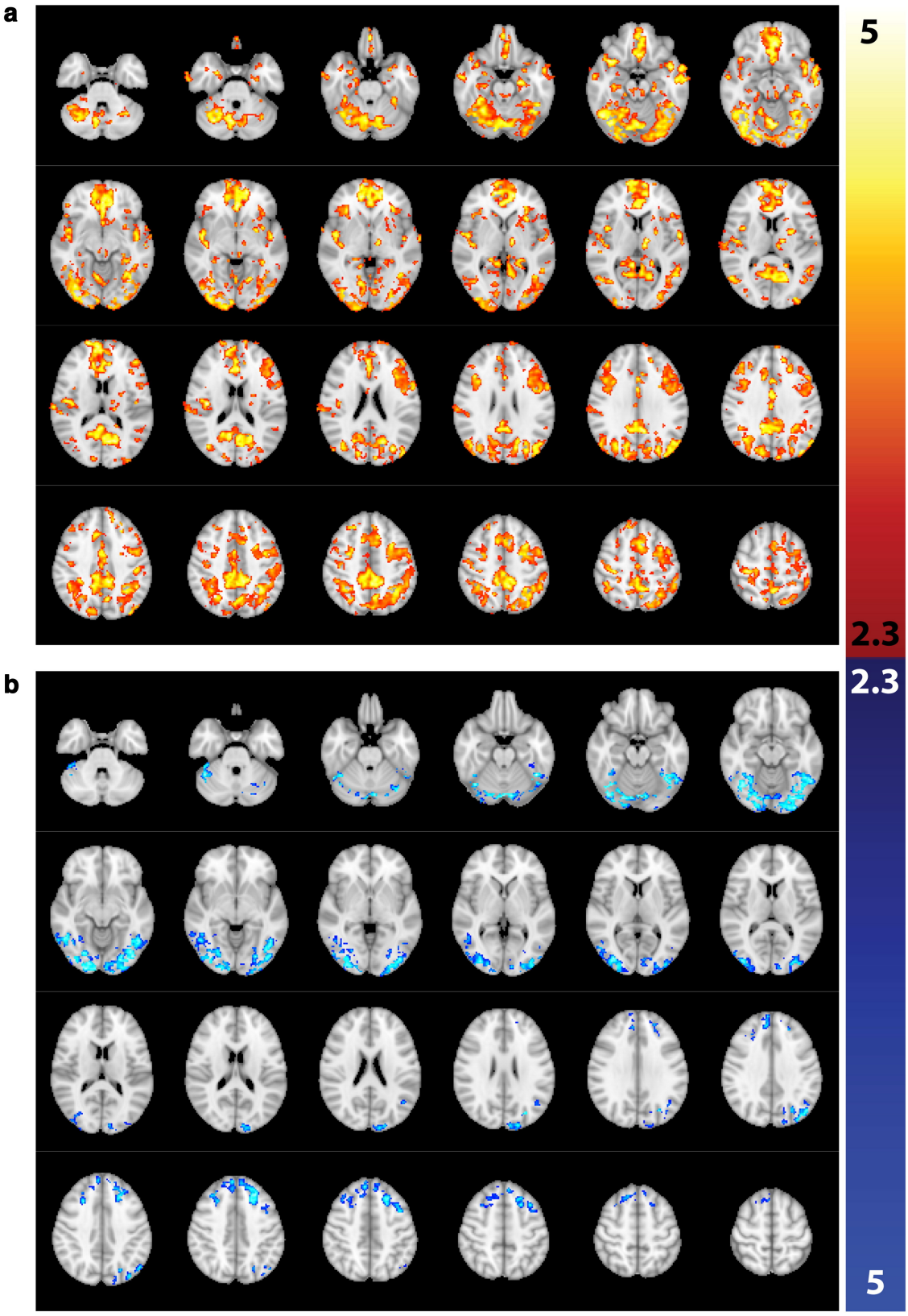

Figure 4.6: Comparison of SE EPI and GE EPI CNR (in z-scores): a) activated regions (both contrasts) with GE EPI having higher z-scores and b) activated regions (both contrasts) where SE has higher z-scores.

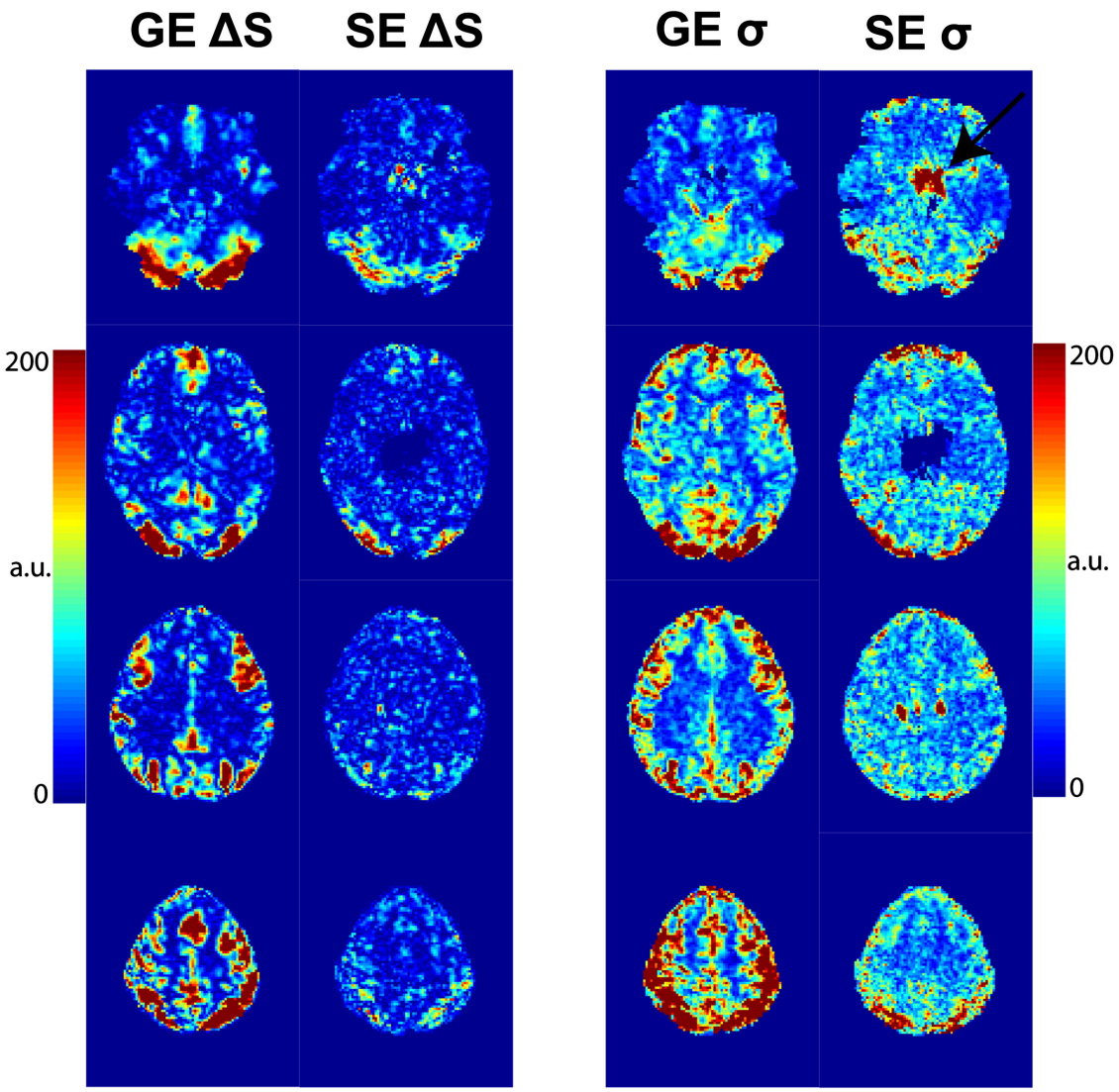

Figure 4.7: Signal change (ΔS) and noise (σ) levels for SE and GE EPI in arbitrary units for four representative slices. In general, GE EPI has higher signal change and noise compared to SE EPI. The arrow in the top slice of SE noise column depicts the noise introduced by the arterial blood.

Table 4.3: The number and percentages of activated voxels present in the gray matter, white matter and CSF.

subject	GE threshold	GE GM	GE WM	GE CSF
1	2.62/2.69	57.191 66.2%	16.723 19.4%	12.472 14.4%
2	2.65/2.76	49.485 66.5%	17.128 23.0%	7771 10.5%
3	2.68/2.64	51.514 61.9%	21.098 25.3%	10.648 12.8%
4	2.74/2.99	26.052 55.8%	15.005 32.1%	5624 12.1%
5	2.50/2.84	62.577 62.0%	24.703 24.5%	13.685 13.5%
6	2.71/2.76	34.981 65.2%	12.422 23.2%	6247 11.6%
average $\pm$ std		63.3 $\pm$ 4.0%	24 $\pm$ 4.2%	12.7 $\pm$ 1.4%

subject	SE threshold	SE GM	SE WM	SE CSF
1	3.35/3.70	1340 55.6%	311 12.9%	761 31.5%
2	2.95/3.35	10.194 64.0%	3478 21.8%	2265 14.2%
3	2.83/3.35	8770 53.5%	4443 27.0%	3194 19.5%
4	2.91/4.36	4218 53.8%	1933 24.7%	1686 21.5%
5	2.88/3.05	12.465 59.7%	4176 20.0%	4253 20.3%
6	3.15/3.85	5253 57.6%	2345 25.7%	1514 16.6%
average $\pm$ std		58.2 $\pm$ 4.0%	23.0 $\pm$ 5.2%	18.8 $\pm$ 6.0%

SAR problem as the RF power per unit time linearly increases with the acceleration factor. Power deposition of PINS pulses is independent of the number of multiband slices, currently making them a natural option for SE EPI at 7T. Another limitation related to the hardware rather than the safety limits is the peak voltage which also increases linearly with the flip angle and the number of slices. In this study, in line with previously reported RF peak power reduction methods [4][53][61] we optimized the phases of the multiplexed slices along the lines of Wong (2012) and achieved a 26% decrease in the RF peak amplitude. The low signal intensity observed at the center of SE EPI images is caused by B1 inhomogeneity which is a typical feature of high field. Even though for this specific study the Stroop task does not show activation close to the center of the brain, this issue should be resolved by recent advances in SMS parallel transmission ([120]) or better RF shimming [68][32].

The possible acceleration in one direction is determined by the independent information (i.e. reconstruction power) that is available from the coil channels in that specific direction. The reconstruction power can be transferred from the PE direction to the multiband direction with the blipped CAIPIRINHA [138] approach by shifting the slices with respect to each other in the PE direction in a controlled fashion and thus maximizing the distance between aliased voxels. This allows higher acceleration factors in the multiband direction. Alternatively, one can accelerate in

the PE direction by skipping some of the PE lines periodically as in this study. In this case, the shortened readout train also results in slightly lower image TR but the real benefit is the reduced EPI distortion. Furthermore, the minimum achievable TE potentially decreases and provides the opportunity, especially for GE EPI, to diminish dropout and signal loss due to intra-voxel spin dephasing with shorter TEs [47][111] [127][133] or indeed to acquire multi-echo data [121][142].
The color-word Stroop task is a stable and consistent fMRI paradigm generating robust BOLD activation in many brain regions including the orbito-frontal areas [168]. As expected, SE EPI and GE EPI detected activation at the same locations but with different cluster sizes. Owing to its higher functional sensitivity, GE EPI has larger cluster sizes and higher z-scores in almost the whole brain. One of the surprising results of this study is the significant activation observed with GE EPI in the frontal and sub-cortical regions. Several studies have hypothesized and shown the poor performance of GE EPI within regions prone to susceptibility artifacts [106][136]. On the other hand, GE EPI has been the workhorse of fMRI research and thus many methods to cope with and reduce those susceptibility related artifacts have been investigated. Z-shimming ([52]) and tailored RF pulses [51][145] help to reduce dephasing in the slice direction. Data quality can also be improved by just optimizing/adjusting the slice orientation [33]. Two studies at 3 T reported the benefit of increasing spatial resolution. By reducing the slice thickness, they obtained comparable (with respect to SE EPI) GE EPI activation in the temporal lobe and orbito-frontal cortex [133] and increased functional contrast in the amygdala [127]. In light of the mechanisms described above, the activation observed with GE EPI near air/tissue interfaces results from a combination of high spatial resolution (thinner slices) and higher sensitivity at 7T even though inhomogeneity effects due to susceptibility gradients are much stronger.
With regard to differences between SE EPI and GE EPI for fMRI, the measure of interest is CNR rather than tSNR or activation cluster size. The CNR difference maps in Fig. 4.6 reveal that in general, GE EPI is superior to SE EPI with the exception of some parts of the visual cortex and frontal lobe. When further investigated, we found that GE EPI has higher signal change but also higher residuals (Fig. 4.7) which might explain the comparable CNR of GE EPI and SE EPI in the visual cortex. The difference in contrast between SE EPI and GE EPI at high field is generally attributed to the fact that GE EPI BOLD signal is formed by all the 4 contrast mechanisms whereas only the extravascular dynamic averaging plays a role in SE EPI BOLD signal. This argument is also the basis for SE signal being considered as strongly weighted by the microvascular contribution and, thus being more specific to the true activation site. A recent

study [21] has shown that the ratio of micro- to macrovascular signals is around 0.6 for GE EPI and between 0.75 and 1.02 for SE EPI at 9.4T. These values are much lower than those indicated by previous simulation results [155] and the ratios will only be lower at 7T. The authors listed the possible reasons as the T2* weighting (due to the EPI readout), T2 values of venous blood not being as short as previously reported [49][58] and inflow effects due to the limited FOV. In the same paper, it was also demonstrated that shorter readout times and longer echo times increase the microvascular contribution to the SE signal. The protocol used in our study makes it possible to reduce the possible artifacts associated with SE EPI by acquiring whole brain SE EPI data (effectively reducing inflow effects) at 7T. Furthermore, the potential SNR increase from the MB excitation can be traded in for acceleration in the PE direction and hence shorter readouts (higher in plane acceleration factors). The echo time can also be increased if needed as with MB acceleration volume TR will still be sufficient.

The physiological and BOLD noise of SE EPI and GE EPI are comprised of different effects. The non-T2 effects contribute a small portion of the SE EPI signal and mostly originate from CSF and inflow effects [166], e.g., the region pointed with the arrow in Fig. reffig:figure7 suffers from the noise coming from the arterial blood. It can be argued that the mechanisms associated with the lower SE EPI BOLD signal are also responsible for reducing the physiological fluctuations, hence the almost homogeneous noise profile for SE EPI (cf. Fig. 4.7). The high noise level and the signal change in the visual areas for SE and GE EPI suggest that non-task related BOLD noise contributes to the overall noise. GE EPI noise is greatest in the gray matter. This is to be expected, because for GE EPI with increasing field strength and voxel dimensions, the physiological noise dominates over the thermal noise [150]. The increased noise of GE EPI suggests that the physiological noise (pulsation, breathing) compartment still contributes to the overall noise. In fact, both GE EPI and SE EPI data with this specific resolution fall under the physiological noise regime as previously demonstrated. [151][166] While one expects a certain inaccuracy due to the partial volume effects and suboptimal segmentation, results shown in Table 4.3 also have interesting implications for the choice between whole brain fMRI studies at 7T: not only is GE-EPI more sensitive, in the analysis of our experiments GE-EPI has relatively more activation in GM compared to SE-EPI. It also shows that there are relatively more activated voxels in CSF of SE-EPI compared to GE-EPI potentially due to the strong relative weighting of CSF in the SE-EPI images combined with dynamic averaging effects around large “activated” veins embedded in CSF [118] plus the additional GE weighting due to the finite duration of the EPI readout. The significant difference in CSF suggests that SE

EPI signal may have a greater contribution from the pial vessels. The residual activation in the white matter can be attributed to the partial volume effects, and suboptimal segmentation due to the relatively low resolution and smoothing. It should be noted that the ratio of activated voxels within the white matter compared to the gray matter and CSF gradually decreased as the thresholds were increased. This observation was reflected in the mixture modeling by choosing a threshold which ensures that the number of false positives is significantly less (by a factor of 3) than false negatives and produces meaningful clusters.

Although there is considerable evidence for an improved spatial specificity of SE fMRI over GE fMRI in the literature [21][36][166], hitherto all studies have been confined to primary cortical areas and relatively strong activation paradigms. Here we surprisingly found no evidence for improved spatial specificity of spin-echo EPI even when we examined those regions with comparable sensitivity with GE-EPI (results not shown). The results from this study, which to our knowledge is the first to compare GE and SE at 7T using a more standard cognitive paradigm, would seem to indicate that there is little benefit to using SE-EPI, as the sensitivity is considerably lower and there is no obvious improvement in spatial specificity. The results of the present study are however in line with recent work indicating that the T2 of venous blood may not be as short as previously thought. [49][82] Of itself the higher contribution from CSF to the SE-EPI signal may not be inconsistent with a higher spatial specificity for SE-EPI within the gray matter, as the activated voxels in CSF would be unlikely to affect retinotopic mapping experiments [110] which constitute the gold standard for determining the spatial PSF in vivo.

Chapter 5

Clinical application of Half Fourier Acquisition Single Shot Turbo Spin Echo (HASTE) imaging accelerated by simultaneous multi-slice acquisition

Jenni Schulz[1], Jose P Marques[1], Annemieke ter Telgte[1,2], Anouk van Dorst[3], Frank-Erik de Leeuw[1,2], Frederick JA Meijer[4], David G Norris[1,5]

[1]Donders Institute for Brain, Cognition and Behaviour, Radboud University Nijmegen, The Netherlands

[2]Department of Neurology, Radboud University Medical Centre Nijmegen, The Netherlands

[3]Department of Radiology and Nuclear Medicine, Jeroen Bosch Hospital, 's Hertogenbosch, The Netherlands

[4]Department of Radiology and Nuclear Medicine, Radboud University Medical Centre Nijmegen, The Netherlands

[5]Erwin L. Hahn Institute for Magnetic Resonance Imaging, University Duisburg-Essen, Essen, Germany

Abstract

Purpose: As a single-shot sequence with a long train of refocusing pulses, Half-Fourier Acquisition Single-Shot Turbo-Spin-Echo (HASTE) suffers from high power deposition limiting use at high resolutions and high field strengths, particularly if combined with acceleration techniques such as simultaneous multi-slice (SMS) imaging. Using a combination of multiband (MB)-excitation and PINS-refocusing pulses will effectively accelerate the acquisition time while staying within the SAR limitations. In particular, uncooperative and young patients will profit from the speed of the MB-PINS HASTE sequence, as clinical diagnosis can be possible without sedation.

Materials and Methods: MB-excitation and PINS-refocusing pulses were incorporated into a HASTE-sequence with blipped CAIPIRINHA and TRAPS including an internal FLASH reference scan for online reconstruction. Whole brain MB-PINS HASTE data were acquired on a Siemens 3T-Prisma system from 10 individuals and compared to a clinical HASTE protocol.

Results: The proposed MB-PINS HASTE protocol accelerates the acquisition by about a factor 2 compared to the clinical HASTE. The diagnostic image quality proved to be comparable for both sequences for the evaluation of the overall aspect of the brain, the detection of white matter changes and areas of tissue loss, and for the evaluation of the CSF spaces although artifacts were more frequently encountered with MB-PINS HASTE.

Conclusion: MB-PINS HASTE enables acquisition of slice accelerated highly T2-weighted images and provides good diagnostic image quality while reducing acquisition time.

5.1. Introduction

Half-Fourier acquisition single-shot turbo spin-echo (HASTE) is the single-shot form of the widely used rapid acquisition with relaxation enhancement (RARE [62]) technique, also called fast spin-echo (FSE) or turbo spin-echo (TSE). It is nowadays routinely used in clinical practice because of its short acquisition time combined with diagnostic T2 contrast image quality. [99] HASTE makes exclusive use of spin echoes [56] which reverse the effect of T2 relaxation and eliminate the inhomogeneity effects of the static magnetic field. Due to the high number of 180°refocusing pulses used in the extended echo train, HASTE sequences have high radiofrequency (RF) power depositions. This is especially problematic at high spatial resolutions (requiring many refocusing pulses) and high field strength (where the power deposition per pulse is higher).

Several methods have been developed to reduce the power deposition in conventional TSE/HASTE sequences. A straightforward solution is to reduce the flip angle of the 180°refocusing pulses. [60] To improve the signal at low refocusing angles and regain sensitivity, the refocusing pulse angles can be tailored to approach a suitable equilibrium. [131] Taking the steady state nature of TSE into account [2], one obtains the greatest signal if the magnetization is continuously in a pseudostatic steady state. [63] In long echo trains, high signal intensity can be obtained for the k-space center lines and low signal intensity for the outer parts of k-space by using this approach, which is called transition between pseudo steady states (TRAPS). [63]

Recently, Norris et al [101] have shown that it is possible to reduce the power deposition in TSE to a level where it becomes applicable at 7T. They investigated the orthogonal approach of simultaneous multi-slice (SMS) imaging, also called multiband imaging (MB), using power independent of number of slices (PINS) pulses for excitation and refocusing. [102] Besides TSE, PINS pulses have also been successfully applied to high spatial resolution resting state fMRI using SE-EPI at 7T [71] and high resolution DWI [39].

SMS imaging was first proposed by Larkman [76] in 2001 and provides the possibility to accelerate acquisition in the slice direction by exciting and acquiring N slices simultaneously without the penalty of a sqrt(N)-reduction in signal to noise ratio. [45][97] For a recent review on SMS imaging see Barth et al [8].

A restriction in SMS-imaging which needs to be considered for the protocol setup is that the total number of acquired slices needs to be a multiple of the MB-factor. Since the power deposition and amplitude of the MB pulses depends linearly on the number of simultaneously excited slices,

MB RF pulses become rather demanding especially when high MB-factors are used. Due to the long echo-train used in HASTE imaging, the major power deposition in a HASTE acquisition is deposited by the many refocusing pulses. It is therefore not critical to adjust or optimize the excitation pulse in terms of power deposition, as its contribution is negligible.
PINS pulses rely on periodic excitation to circumvent the increased power deposition of the traditional approach. This way, the number of simultaneously excited slices is only limited by the dimensions of the RF coils or the size of the body. In fact, the higher the number of simultaneously excited slices, the higher is the reduction in power deposition. Recently, a combination of MB and PINS pulses has also been introduced called MultiPINS. [40] In this context, it is further advisable to also apply blipped CAIPIRINHA to minimize the distance between simultaneously excited slices at constant G-noise. [138] This method shifts individual slices within the FOV by a defined shift factor FOV /x improving image quality and allowing closer gaps between adjacent slices.
Because of the short acquisition time, T2 HASTE is commonly used in neuroimaging of uncooperative patients, unsedated children (usually below 6 years of age), or for dynamic image acquisitions. The overall aspect of the brain and the CSF spaces can be adequately evaluated for the diagnosis and follow-up of hydrocephalus [114], and gross pathology such as large space occupying lesions or areas of tissue loss [147]. In comparison to a T2 TSE sequence, small lesions and small areas of tissue signal intensity changes may, however, be overlooked with a T2-HASTE sequence [57]. T2 HASTE can also be applied for imaging other parts of the body, such as the spine, abdomen (imaging moving organs such as bowel) or fetal imaging. [148][24][35][132]
In this work, we present an ultrafast whole brain high resolution HASTE acquisition with standard MB excitation and PINS refocusing pulses combined with blipped CAIPIRINHA and TRAPS which speeds up the acquisition compared to a standard clinical HASTE protocol.

5.2. Methods

5.2.1. Design of sequence

MB excitation pulses and PINS refocusing pulses were incorporated into a standard Siemens HASTE sequence. The MB pulses consist of complex-summed [97] individually modulated RF pulses. The MB excitation pulse duration was prolonged to 3.5ms compared to 2.0ms for the standard Siemens HASTE in order to obtain an adequate slice profile. The PINS refocusing pulses

had a slightly prolonged duration of 2.3ms, instead of 2.0ms in the original HASTE sequence to allow some extra time for the slew rate demanding PINS gradient blips and still accommodate 11 PINS-subpulses. In prior simulations using IDL (Harris Geospatial Solutions, Boulder Colorado), the 11 sub-pulses were optimized to obtain the best possible slice profile for a given ratio of "slice spacing/slice thickness = N". The simulation showed that the use of 11 sub-pulses set a maximum value of 11 for the value of N: thinner slices were not possible. The bandwidth (BW) of the PINS pulses depends on N and is given by:

$$\text{BW(PINS)} = 1/\text{duration} \times \text{no of subpulses} \times (\text{slice thickness})/(\text{slice spacing}) \tag{5.1}$$

It is therefore desirable to keep N as small as possible, but even when pushing it to its limits in terms of reconstruction feasibility, PINS remain low BW RF pulses.

To avoid off-resonance artifacts, the BW of the MB excitation pulse was matched to the BW of the PINS pulses. In any case, the slice profile of the PINS should not influence the actual slice profile to a great extent since the actual slice profile will be mainly defined by the MB excitation RF pulse which was additionally slice profile optimized.

In order to fulfill the CPMG condition, the phase ramps of the MB pulse had 0 phase at the center of the pulse and the phase ramp applied to the individual PINS sub-pulses was implemented yielding zero phase for the central sub-pulse ensuring a 90°phase offset between the centers of excitation and refocusing pulses.

The gradient moments necessary for the application of the blipped CAIPIRINHA technique were combined with the spoiler gradients around the refocusing RF pulses to ensure the shortest possible echo spacing.

Unlike segmented TSE acquisitions [101], HASTE acquisitions, as a single-shot acquisition, have a long echo-train. Therefore, it is necessary to incorporate in-plane parallel imaging techniques such as GRAPPA [55] into the protocol to shorten the echo-train length (ETL). The low BW pulses lead to a significant chemical shift displacement error for the fat signal which in combination with parallel imaging leads to parallel imaging artifacts caused by the physical separation of the fat and water slices, which makes fat saturation essential in SMS protocols. [8] To decrease the power deposited along the echo-train, the TRAPS option was implemented. [63] This way only the center of k-space +3 lines would experience the full 180°flip angles followed by a ramp of 6-10 echoes. All other refocusing pulses had the indicated target TRAPS flip angle.

The entire sequence diagram is shown in figure 5.1. In SMS imaging, it is advisable to acquire an

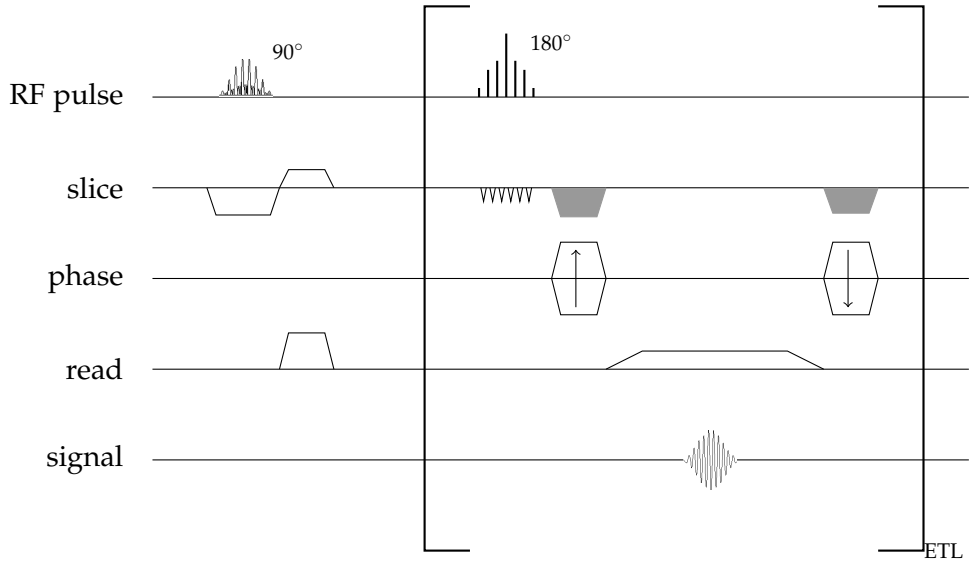

Figure 5.1: Sequence diagram of the implemented HASTE sequence. It consists of a 90°MB excitation pulse followed by an echo train of slice profile optimized 180°PINS refocusing pulses (ETL: echo train length). The blipped CAIPRINHA method has been implemented in combination with the spoilers along the slice direction.

odd number of slices in interleaved series mode to avoid adjacent slices being excited immediately one after another. [137] The application of PINS refocusing pulses can lead to a degraded slice profile which can affect and saturate neighboring slices. An interleaved slice order, an increased slice gap and a slightly prolonged TR all help in avoiding saturation effects.

For the protocol setup, it is additionally necessary to consider the reconstruction feasibility of the aliased slices. To be able to cleanly disentangle the simultaneously acquired slices, the slice spacing cannot be arbitrarily small, but usually remains around 27-30mm for brain imaging with the commonly used 32 channel receiver coils. To enable online reconstruction, a gradient echo reference scan was incorporated at the beginning of the sequence before the actual HASTE acquisition.

Owing to the constraints described above, we aimed to develop the best possible MB-PINS HASTE protocol which is drastically reducing the acquisition time while giving best image quality and to compare it with a standard clinical protocol. This led to some key imaging parameters differing from each other (as shown in table 5.1), as otherwise there would have been artifacts in the MB-PINS HASTE images.

Table 5.1: Protocol parameters of the whole brain acquisitions of the standard clinical HASTE, the accelerated MB-PINS HASTE and the T2-TSE reference. Note that 'TR' in HASTE (single shot) protocols is the time interval between the excitation of consecutive slices while in a TSE sequence it refers to the time interval between consecutive excitation of the same slice (with a different phase encoding).

	TAcq	TR/TE	matrix	FatSat	iPAT	PF	FA
clinical HASTE	18.2 s 14.7 s 19.6 s	700/92 ms	320x243	no	2	5/8	150°
MB-PINS HASTE	9 s	1000/91 ms	320x243	yes	2	5/8	TRAPS 90°
T2-TSE	86 s	6000/99 ms	640x640	no	2	-	150°

	MB	CAIPI	slice spacing	slices	gap	resolution
clinical HASTE	-	-	-	trans 26 sag 21 cor 28	20%	0.8x0.8x5.0mm^3
MB-PINS HASTE	3	3	54 mm	trans 27 sag 27 cor 27	33%	0.8x0.8x4.5mm^3
T2-TSE	-	-	-	trans 29	25%	0.3x0.3x4.0mm^3

5.2.2. Data acquisition

Data were acquired on a 3T MR system (Magnetom Prisma, Siemens AG, Healthcare Sector, Erlangen, Germany) using a 32-channel head coil.

To evaluate the diagnostic image quality, the MB-PINS HASTE sequence was compared to a standard HASTE protocol for brain imaging as it is pre-installed on the Magnetom Prisma by Siemens. [115] Whole brain acquisitions were obtained for both protocols in transversal, sagittal and coronal orientations. The protocol parameters of the clinical HASTE and the MB-PINS HASTE are shown in table 1. The parameters were matched as closely as possible under consideration of the MB- and PINS-related restrictions outlined above.

Additionally, a standard T2-TSE protocol was acquired in transversal orientation serving as a reference for the evaluation of the diagnostic quality of the HASTE acquisitions. The T2-TSE acquisition parameters are also shown in table 5.1.

5.2.3. Study population

Experiments are reported here from 10 participants (gender: 5 male and 5 female, age: 63-74 years). Individuals were participants in an internal study with the aim to investigate the origin and consequences of cerebral small vessel disease. [158] All subjects had moderate to severe cerebral small vessel disease (CSVD) including white matter hyperintensities and/or lacunar infarcts. Exclusion criteria are dementia and Parkinson's disease. The study was approved by the medical ethics committee region Arnhem-Nijmegen and individuals gave prior written informed consent.

5.2.4. Evaluation of diagnostic image quality

Diagnostic image quality was independently rated in different categories by a neuroradiologist and a neuroradiologist in training. First, images were evaluated for artifacts and overall image quality on 4- and 5-point scales respectively. Next, diagnostic image quality was scored for the evaluation of the overall brain parenchyma, gyration pattern, white matter changes (both diagnostic image quality and Fazekas score [44]), CSF spaces (peripheral / ventricular system / perivascular spaces) and intracranial vascular flow voids. The following rating scales were used:

Artifacts

0 - no artifacts
1 - little artifacts, not hampering image evaluation
2 - artifacts, hampering image evaluation
3 - severe artifacts, no diagnostic evaluation possible

Image quality

1 - not diagnostic
2 - moderate
3 - fair
4 - good
5 - excellent

Deep white matter changes score ([44])

0 - absent

1 - punctate foci

2 - beginning confluence

3 - large confluent areas

5.3. Results

We were able to run the implemented MB-PINS HASTE sequence with a protocol similar to the standard clinical HASTE protocol, but with an acceleration factor of 2 for the transversal protocol, 1.6 for the sagittal and 2.2 for the coronal acquisition. (The non-integer values for the acceleration are due to the differences in total number of slices and TR.)

An example of three simultaneously excited slices from a representative subject is shown in figure 5.2 together with the corresponding slices of the clinical HASTE and T2 TSE sequences. The MB-PINS HASTE images show good image quality regarding the overall aspect of the brain demonstrating that the overlapping slices were satisfactorily separated. The main difference between the protocols arises from the fat saturation pulse used in the MB-PINS HASTE sequence that results in an image without subcutaneous fat and bone marrow signal.

The diagnostic quality evaluation scores of the two raters are shown in table 5.2. For each item rated, an average score including the standard deviation (std) was calculated. Artifacts were more

Table 5.2: Evaluation of the diagnostic image quality independently rated by a neuroradiologist (1) and a neuroradiologist in training (2) in categories: artifacts, overall image quality, gyration pattern, white matter changes(image quality / Fazekas[44]), overall brain parenchyma, CSF (peripheral /ventricular system/ perivascular spaces), vascular flow voids. Artifacts-scale 0-3; image quality-scale 1-5; Fazekas white matter changes-scale 0-3 (individual subject results not included).

clinical HASTE	artifacts	image quality	CSF		
			peripheral	ventricular	perivascular
(1) average $\pm$ std	0.1 ± 0.3	3.9 ± 0.3	5.0 ± 0.0	5.0 ± 0.0	3.6 ± 0.5
(2) average $\pm$ std	0.2 ± 0.4	3.8 ± 0.6	4.7 ± 0.7	4.6 ± 0.7	4.7 ± 0.7
MB-PINS HASTE					
(1) average $\pm$ std	0.6 ± 0.5	3.9 ± 0.3	5.0 ± 0.0	5.0 ± 0.0	3.9 ± 0.3
(2) average $\pm$ std	0.7 ± 0.5	3.4 ± 1.0	4.4 ± 0.7	4.7 ± 0.5	3.9 ± 1.0

clinical HASTE	gyration pattern	brain parenchyma	white matter changes	flow voids
(1) average $\pm$ std	4.9 ± 0.3	3.7 ± 0.5	3.6 ± 0.5	3.2 ± 0.6
(2) average $\pm$ std	4.0 ± 0.8	3.6 ± 0.5	3.2 ± 0.9	3.5 ± 0.7
MB-PINS HASTE				
(1) average $\pm$ std	4.9 ± 0.3	3.9 ± 0.3	4.0 ± 0.5	3.1 ± 0.3
(2) average $\pm$ std	4.1 ± 0.9	3.6 ± 1.0	3.7 ± 1.3	3.2 ± 0.9

frequently encountered on MB-PINS HASTE compared to the clinical HASTE. They were concave

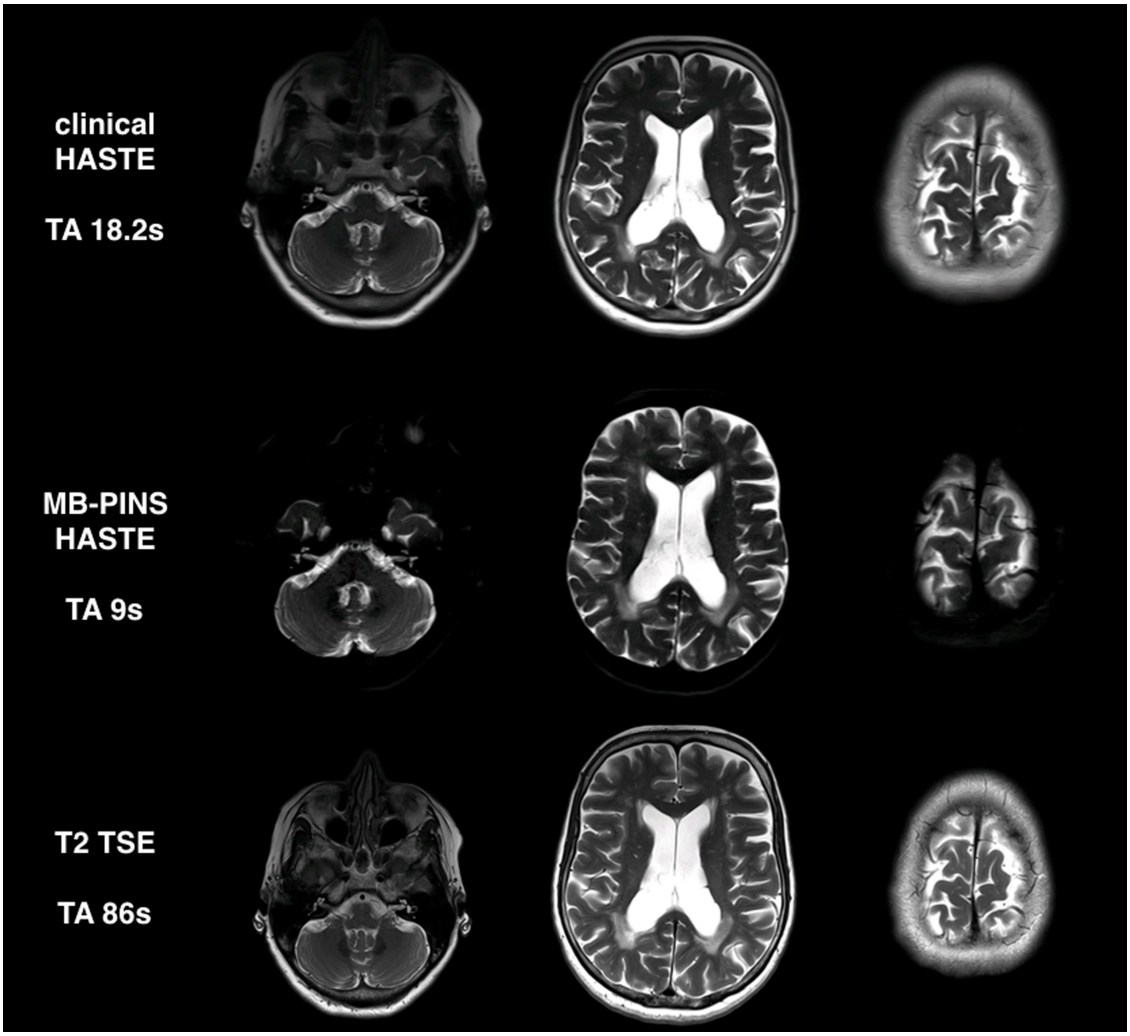

Figure 5.2: Three example slices from a representative subject which were simultaneously excited in the MB-PINS HASTE sequence (middle). For the clinical HASTE (top) and T2-TSE (bottom) sequence the corresponding slices are shown. Additionally, acquisition times for the whole brain acquisition are given. (W/L settings were comparable for the different sequences. Due to the differences in the acquisition protocol, contrast and brightness are not fully identical.)

overlying the insular region, not resembling any clinically encountered disease and therefore not hampering diagnostic image quality. Overall image quality, gyration pattern, brain parenchyma, CSF spaces and intracranial vascular flow voids were scored as comparable for both sequences. However, the diagnostic image quality for the evaluation of cerebral white matter changes on MB-PINS HASTE had a slightly higher score than the clinical HASTE series for both raters.
Figure 5.3 demonstrates examples in transversal, sagittal and coronal orientation of a representative subject, including the T2 TSE as the reference standard. For this participant, areas of tissue loss can be observed throughout the brain, consistent with prior infarctions, as well as cerebral white matter changes. These can be adequately depicted on the MB-PINS HASTE sequence.

5.4. Discussion

In this study, we demonstrated that whole brain imaging using a MB-PINS HASTE sequence at 3T is feasible. MB-PINS HASTE enables acquisition of slice accelerated highly T2-weighted images within SAR limitations and therefore ultrafast spin- echo imaging can be performed to acquire anatomical T2-weighted images.
We have shown that the diagnostic image quality of the MB-PINS HASTE sequence is comparable to the clinical T2 HASTE protocol. The higher frequency of artifacts in the MB-PINS HASTE did not detract from the diagnostic utility. Tissue contrast for the evaluation of cerebral white matter changes seems possibly even superior on the MB-PINS HASTE in comparison to the clinical HASTE sequence, though this would need to be verified in a larger cohort of subjects.
With the application of the multiband technique, the acquisition time of the MB-PINS HASTE sequence can be decreased considerably. In principle, for protocols which are identical in TR and total number of slices, the acquisition is sped up by the multiband factor. In this work, the total number of slices between the clinical protocol and the MB-PINS HASTE somewhat differs due to the limitation that the total number of slices in a multiband acquisition needs to be a multiple of the multiband factor (which ensured in all cases a larger brain coverage when using the MB-PINS HASTE sequence). Also, the TR was slightly increased in the MB-PINS HASTE acquisition. Considering the total number of slices, the possible slice spacing, slice thickness and gap, it seemed sensible to choose a multiband factor of 3. In total, this results in this case in an acceleration factor of around 2 for the three acquisitions.
Taking the acceleration due to the parallel imaging into account, the absolute acceleration of the

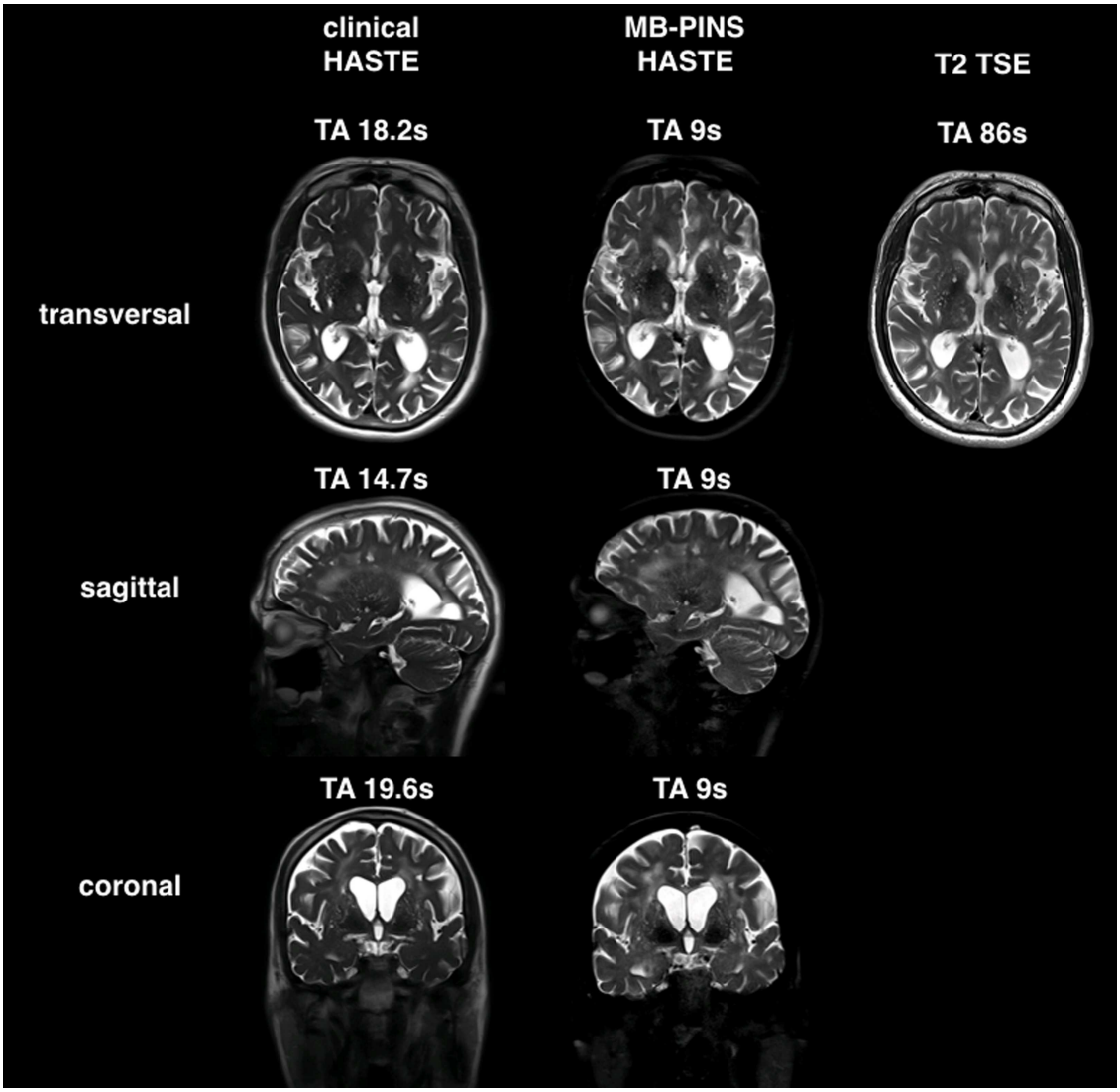

Figure 5.3: Transversal (top), sagittal (middle) and coronal (bottom) orientation comparison of the clinical HASTE and MB-PINS HASTE with whole brain acquisition times. The T2-TSE sequence is additionally shown in transversal orientation serving as a reference. (W/L settings were comparable for the different sequences. Due to the differences in the acquisition protocol, contrast and brightness are not fully identical.)

MB-PINS HASTE acquisition sums up to a factor of 6 (simultaneous multi-slice 3 times in-plane acceleration 2) which can be implemented with a 32 channel coil without severe penalty in SNR (g-factor noise amplification [123]) and imaging artifacts related to the reconstruction. With the MB-PINS HASTE sequence, it is in principle possible to also acquire pure T2 fMRI images. The application of HASTE fMRI would be especially interesting at high magnetic field strengths. Further, MB-PINS HASTE could be a useful tool to speed up and improve whole body diffusion imaging [70]. Additionally, this type of fast single shot imaging with anisotropic voxels could be used in combination with super-resolution as used in fetal imaging [130]. It could further find application in for instance abdomino-pelvic imaging [86].

5.5. Conclusion

In conclusion, MB-PINS HASTE enables acquisition of slice accelerated highly T2-weighted images and provides good diagnostic image quality while reducing acquisition time. It offers the possibility of using ultrafast spin-echo imaging to acquire anatomical T2-weighted images and potentially to follow dynamic signal changes.

Chapter 6

Reduced peak power in paired excitation and refocusing multiband pulses by quadratic phase modulation

Jenni Schulz[1], David G Norris[1,2]

[1]Donders Institute for Brain, Cognition and Behaviour, Radboud University Nijmegen, The Netherlands

[2]Erwin L. Hahn Institute for Magnetic Resonance Imaging, University Duisburg-Essen, Essen, Germany

Abstract

Purpose: The amplitude of an RF-pulse is limited by the maximum transmit voltage of the system. In multiband imaging, the peak voltage depends linearly on the number of simultaneously excited slices and high RF-amplitudes can limit the application of multiband imaging, especially when high multiband factors are required. In this work, we propose a solution based on quadratic phase modulation in the spatial domain to reduce the peak voltage in multiband spin-echo sequences.
Theory and Methods: Using the Bloch equations, the quadratic phase modulation is applied to the Fourier transform of a standard Shinnar-Le-Roux pulse. As a single pulse with a quadratic phase modulation cannot be rephased by application of a linear magnetic field gradient pulse, the pulses are played out as excitation-refocusing pairs ensuring that all transverse magnetization can be refocused in the spin-echo.
Results: Applying a quadratic phase modulation can drastically reduce the peak voltage by up to 50-60%. Additionally applying the Wong phase optimization scheme will lead to even further peak voltage reduction of in total up to 70-80%. The generated slice profiles show a rather smooth plateau.
Conclusion: The proposed technique offers the possibility to reduce the peak voltage of an RF-pulse by applying a quadratic phase-modulation in the spatial domain. This is especially useful when multiband imaging is applied in SE-sequences.

6.1. Introduction

In 2D imaging, parallel imaging techniques can only accelerate an acquisition in-plane. Multiband imaging, however, enables an acceleration along the slice direction. First proposed in 2001 by Larkman et al [76], multiband (MB) (also called simultaneous multi-slice (SMS)) imaging provides the possibility to accelerate acquisition in the slice direction by exciting and acquiring N slices simultaneously without the penalty of a $\sqrt{N}$-reduction in signal to noise ratio. [45][97] The superimposed slices can consequently be reconstructed using a SENSE [123] or slice-GRAPPA [138] algorithm.

To excite multiple slices simultaneously, the original RF pulse needs to be modified. Traditionally, a linear phase ramp is applied to an individual RF pulse to shift the slice to the desired location. All individually modified RF pulses are subsequently complex-summed [97] to form the new multiband RF pulse. Both, the power deposition and amplitude of the RF pulse, depend linearly on the number of simultaneously excited slices making MB pulses rather demanding. The RF amplitude is limited by the maximal transmit voltage of the system. Therefore, a number of solutions have been proposed to reduce the peak voltage because high power deposition and/or high peak voltages limit the usability of MB pulses especially at high field strength, and particularly for spin-echo (SE) based acquisitions using 180°refocusing pulses.

Wong suggested to decrease the peak voltage by applying an optimized phase scheme to each of the individual RF-pulses. [163] A different approach by Auerbach et al is to time-shift the individual pulses and therefore avoid overlaying of the individual RF pulse peak voltages. [4] This however requires attention to the resulting different refocusing times. Similar methods to the Wong solution have previously been proposed by Hennig [61] and Goelman [53].

The variable-rate selective excitation (VERSE [29]) algorithm can reduce peak voltage and energy transmission by using a time-varying gradient waveform and a modified RF waveform. However, it may not offer sufficient power reduction for MB-pulses at high fields. Recently, also "power independent of number of slices" (PINS) [102] and MultiPINS [40] pulses (a combination of PINS and MB-pulses) have been introduced. PINS-pulses are strictly speaking an extreme version of a VERSE pulse. Their main characteristic is a periodic excitation profile. So far, PINS-pulses have been successfully applied in multiband SE functional MRI [71], high-resolution diffusion [39] and turbo-spin echo imaging [101] , also at high fields. Unfortunately, PINS pulses do not have a continuous gradient waveform, but consist of alternating RF-sub-pulses and gradient

blips. Therefore, the slew rate becomes a limiting factor and traversal of k-space is very slow. For traditional MB-imaging, MB factors of up to 12 have been reported, but smaller factors are more common as with current receiver coil configurations G-noise becomes the limiting factor from MB factors of about 8 upwards.
Schulte et al. have shown that higher-order polynomial-phase functions can be combined with the Shinnar-Le Roux (SLR) transformation. [134]
Sharma et al. previously proposed a root-flipped MB RF-pulse design method for low peak power pulses for SMS spin-echo MR. By using a Monte-Carlo algorithm, patterns of Shinnar-Le Roux (SLR) β polynomials root flips were determined leading to a uniform distribution of RF energy in time which has some similarities with a quadratic phase pulse and reduces the peak power. [140] However, this technique also suffers from either long excitation pulses, differences in slices' TE or different refocusing times similar to Auerbach's work.
In this work, we propose a method to explore the use of quadratic phase modulation in the spatial domain for reducing peak voltage in MB SE-experiments.

6.2. Theory and Methods

As basis for the quadratic phase modulation, a standard Shinnar-le Roux (SLR, [117]) pulse was used generated by Siemens. The amplitude and phase values of the SLR pulse were extracted from 'pulsetool' in IDEA (Siemens) containing 256 samples and a bandwidth-time-product (BWTP) of 12 being optimized for a flip angle of 90°.
The basic SLR pulse was consequently modified in IDL (Boulder, Colorado, USA). In order to realize a smooth quadratic phase modulation ensuring a proper transmission of the rather long pulses, the SLR pulse was at first scaled up to 2560 samples. The quadratic phase modulation $\phi(t)$ could be applied to the Fourier transform of the RF-pulse according to

$$\phi(t) = c\ t^2\ \omega(t) \tag{6.1}$$

where c is a constant ranging here from 0 to 18 and t is the time. The pulses were initially generated as 90deg pulses. For large flip angles, this is an approximation which however still works well for small phase gradients.
After the quadratic phase modulation, the QUAD-pulses can be extended to MB-pulses. Therefore,

each QUAD-pulse was additionally modulated by a linear phase ramp to apply the corresponding shift and the individual modulated QUAD-pulses were complex-summed to create the final QUAD-MB pulse. As a further addition to reduce the peak voltage, the Wong phase-optimization scheme was also applied to the QUAD-MB pulses. [163]

Quadratic phase-modulated pulses cannot be used for single pulse excitation because the quadratic phase gradient will dephase the signal which cannot be rephased by a conventional gradient. To avoid dephasing and therefore signal loss, QUAD-pulses need to appear as an excitation-refocusing pair. To refocus all transverse magnetization in the spin-echo, the phase of the refocusing pulse must be half of the phase of the excitation pulse according to:

$$\phi_{ref}(t) = 1/2 \cdot \phi_{exc}(t). \tag{6.2}$$

This technique differs with respect to the work of Auerbach et al [4] in terms of the application of the quadratic phase modulation. In contrast to this work, Auerbach simply shifted the pulses in time and superposed them. This is similar to earlier work of Norris [105] applying a quadratic phase over multiple slices. The presented QUAD-MB pulse implementation does not imply a temporal shift of the individual RF-pulses. Therefore, all slices refocus at the same time and the read-out remains unaffected.

All simulations in this work were done in MATLAB (Release 2012b, The MathWorks, Inc., Natick, Massachusetts, United States) using the Bloch simulator which is publically made available by Brian Hargreaves at: http://mrsrl.stanford.edu/ brian/mritools.html.

To investigate the imaging characteristics of the generated QUAD-pulses, the pulses were implemented into a standard Siemens spin-echo (SE) sequence. Here, the highest applicable phase modulation to the excitation pulse corresponds to c=18 (QUAD18) and for the refocusing pulse to c=9 (QUAD9).

Measurements were performed using a standard 32-channel head coil with an oil phantom on a 7T whole-body research MR system (MAGNETOM 7T; Siemens Health-care, Erlangen, Germany). The pulse profiles were acquired by applying the read-out gradient of the SE-sequence in slice direction. If not indicated otherwise, the general RF-pulse settings were: FA 90°excitation, FA 180°refocusing, duration=5120μs, slice thickness=5mm, slice spacing=6*slice thickness. The protocol parameters used in the SE-sequence were: TE 70ms, TR 1240ms, resolution 2.1x0.4x3.0mm, base resolution 512, phase resolution 20%, bandwidth 130 Hz/px, reference voltage 230V.

6.3. Results

Figure 6.1 shows the amplitude and phases of a QUAD0 (left) and QUAD18 (middle) pulse (MB1, 90°) and the simulated pulse profiles. On the right of figure 6.1 the pulse and profiles for the matching QUAD9 180°pulse are demonstrated. With increasing phase modulation, the RF

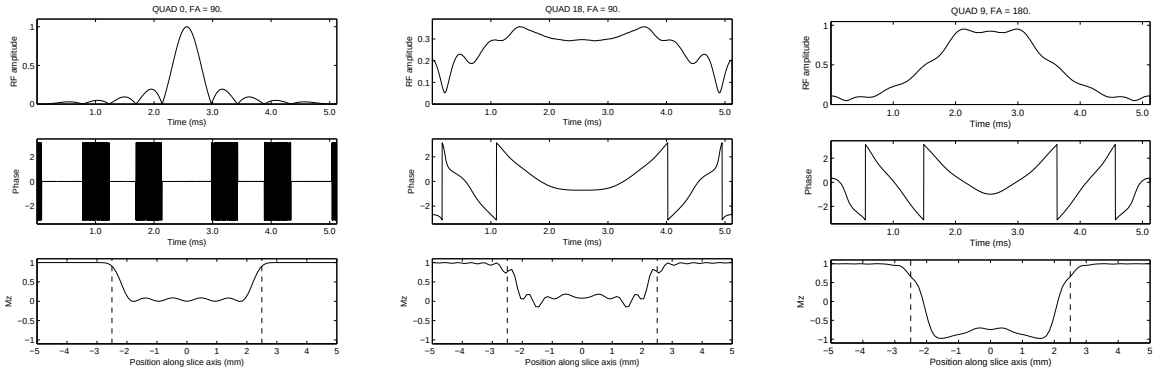

Figure 6.1: Amplitude, phase and simulated profiles for a QUAD0 (left), QUAD18 (middle) and QUAD9 (right) RF-pulses. The RF-amplitude values are normalized with 1 corresponding to the maximal amplitude of a QUAD0 MB1 FA90 pulse. For the Mz-amplitude, 1 unit corresponds to 90 degrees flip.

pulse shape starts to deviate from the original QUAD0 pulse and the simulated pulse profile shape appears less smooth with an increased number of ripples. For the shown QUAD18 RF-pulse, the maximum difference in Mz-amplitude of the plateau is about 15%. However, the additional application of the multiband technique does not have any significant impact on the pulse profile as shown in figure 6.2.

Figure 6.3 shows the peak voltages for different quadratic-phase-modulated pulses and different MB-factors including and excluding the Wong-optimization scheme. The pulses have a flip angle of 90°. In a standard experiment under these conditions, the basic 180°SLR pulse would already clip for a multiband factor of 2. This means that only a MB1 experiment could be realized without increasing the duration of the RF-pulse. However, using a QUAD18/QUAD9 pulse-pair, the peak voltage can be decreased by 52% for the excitation and about 64% for the refocusing pulse respectively which would allow MB-factors up to 3. When additionally applying the WONG phase-optimization to the QUAD-pulses, MB-factors up to 5 (with a slightly decreased refocusing

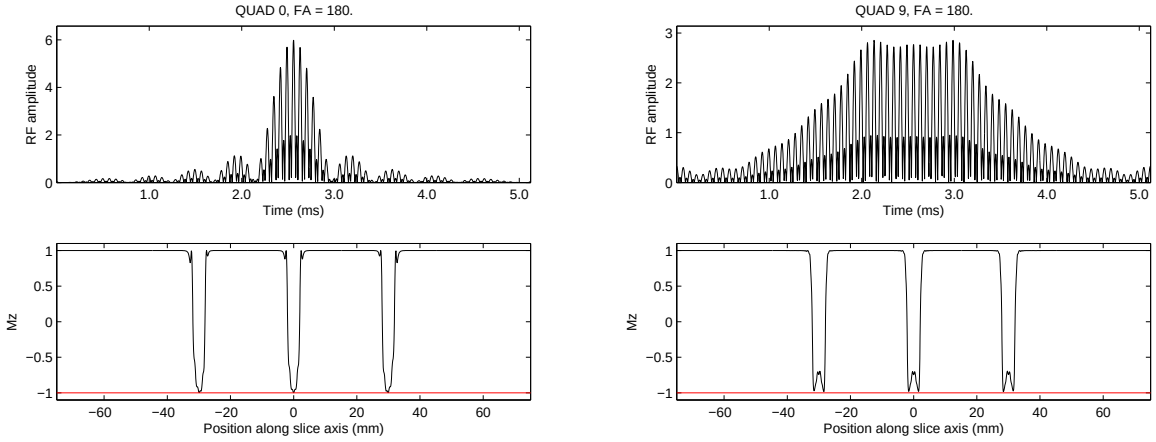

Figure 6.2: QUAD0 (left) and QUAD9 (right) MB3 pulse form (top) and simulated profiles (bottom)

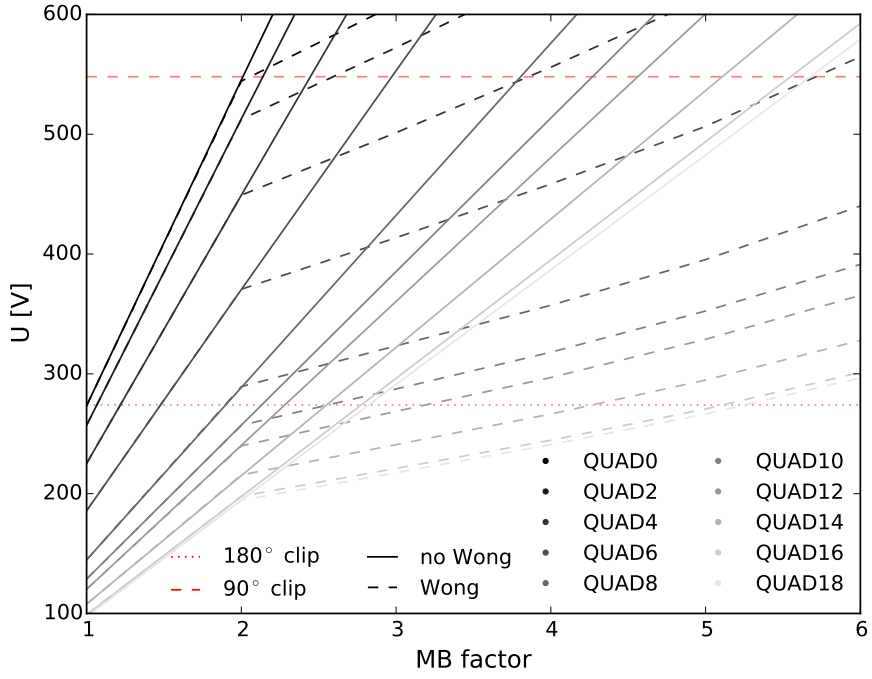

Figure 6.3: The peak voltage in dependence of the MB-factor for different phase modulations excluding and including the Wong phase-optimization. All pulses are 90°pulses, the red lines are indicating the 90°and 180°clipping for a pulse duration of 5120μs and a reference voltage of 230V.

pulse flip angle or increased pulse duration) are possible achieving a total RF peak voltage reduction of 75% for the excitation and about 82% for the refocusing pulse. An example of an QUAD18/9-MB5 RF-pulse with WONG-optimization is shown in figure 6.4

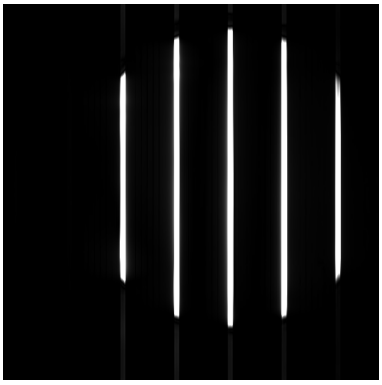

Figure 6.4: Example of the QUAD18-QUAD9 pulse-pair using a multiband factor of 5, WONG optimization and a slice spacing of 10*slice thickness with a slice thickness of 3mm.

In figure 6.5, the measured slice profiles of the QUAD0/0 and QUAD18/9 pulse-pairs are shown. The plateau of the slice profiles appears smooth. The increased number of ripples shown in the simulations cannot be observed in the combined QUAD18-QUAD9 experiment with respect to the QUAD0-QUAD0 acquisition. In the bottom row of figure 6.5, it is demonstrated that the application of multiband imaging does not influence the slice profiles of the off-resonance slices.

6.4. Discussion

The simulations and experimental results show that the peak voltage of an RF-pulse can be reduced by applying a quadratic phase modulation in the spatial domain which is particularly useful in the context of multiband imaging. Instead of applying the pulse with reduced peak voltage, it is also possible to maintain (or only partly reduce) the voltage while shortening the RF-pulse duration accordingly.

It is an advantage that this technique can easily be combined with other peak voltage reduction methods, such as the Wong phase optimization scheme, to achieve additional peak voltage reduction.

Taken as an excitation-refocusing pulse-pair, QUAD-MB pulses offer advantages over previous solutions for reducing the peak RF power such as work from Auerbach [4] and Sharma [140] as the implementation remains on the RF-pulse side and differences in TE or refocusing times do not

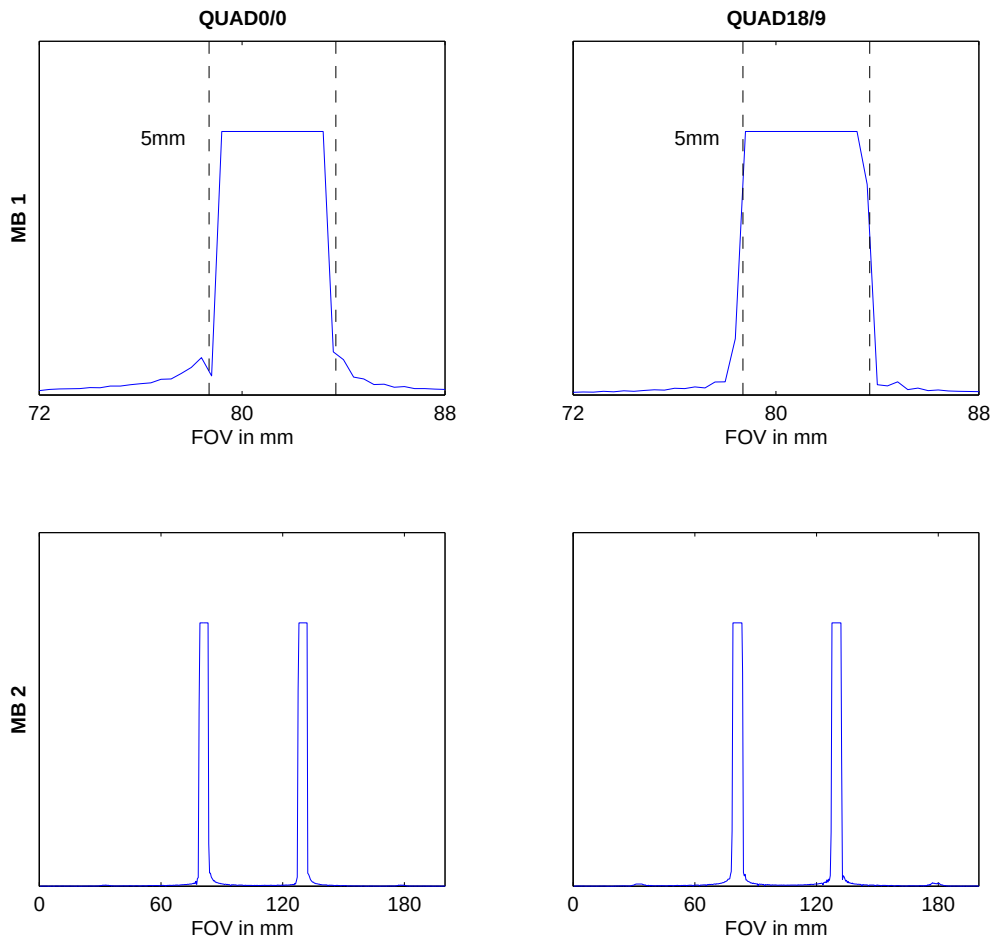

Figure 6.5: Measured slice profiles of the QUAD 0/0 and QUAD 18/9 pulse-pairs. On the top, a zoomed profile of an MB1 acquisition is shown. The bottom row shows the measured results of an MB 2 acquisition.

have to be taken into account.
Due to the quadratic nature of the QUAD-pulses, they can however only be applied in single SE-sequences. It is neither possible to apply a single excitation for gradient-echo acquisitions, nor multiple refocusing pulses as it is necessary in turbo-spin echo/RARE imaging.
Simulations have shown a decreased slice profile quality for highly phase-modulated pulses. In the measurements, we however obtain smooth profiles suggesting that the decreased slice profile quality of the excitation pulse can be compensated by the less phase-modulated refocussing pulse profile.
The main problem with the current implementation is the use of the Fourier transform domain as a proxy for the spatial domain. At high phase modulations and large pulse angles this remains a crude approximation, and should be replaced with a superior design strategy .
The quadratic phase does slightly degrade the slice profile of the RF-pulse. This is probably due to the fact that the SLR algorithm is designed for flat phase pulses. There is however a an algorithm that could be used to generate better pulses. [85]

6.5. Conclusion

This technique offers the possibility of drastically reducing the peak voltage of an RF-pulse by applying a quadratic phase-modulation in the spatial domain. This is especially useful when multiband imaging is applied in SE-sequences.

Chapter 7

Summary

Ever since MR imaging was invented, accelerating acquisitions has been a hot topic. Many different techniques have been developed and some of them are meanwhile well established in every-day scanning methods. For more than a decade, multiband (MB) or simultaneous multi-slice (SMS) imaging has now been applied in different forms and sequences to speed-up acquisitions without the penalty of a $\sqrt{N}$-reduction in signal-to-noise ratio.

Chapter 2 and 3 of this thesis gave examples of how traditional multiband imaging can easily be used to accelerate and improve standard acquisitions. In chapter 2, MB imaging is applied in a 3D TOF-MRA sequence. In chapter 3, an example of accelerating EPI with multiband imaging in combination with echo-shifting was given. Chapter 4 compared an SMS SE-EPI to a standard SMS GE-EPI sequence at 7T in a typical fMRI experiment. The following chapter 5 showed a clinical application of a combination of traditional multiband imaging and PINS pulses to effectively reduce acquisition time while staying within the SAR limitations. The last chapter 6 dealt with the RF pulse design of a new form of multiband pulse reducing peak power which can be applied as an excitation-refocusing pulse pair in SE-based sequences.

CHAPTER 2: Multiband multislab 3D time-of-flight magnetic resonance angiography for reduced acquisition time and improved sensitivity

While mainly used in 2D imaging, multiband imaging is actually not only an acceleration technique which is restricted to slice-by-slice (2D) imaging, but is in certain situations a useful tool to speed-up 3D acquisitions as well. The specific motivation in chapter 2 was not only to use multiband imaging to reduce the rather long acquisition time (TA) of 3D time-of-flight magnetic resonance angiography (TOF-MRA) acquisitions, but to also improve the inflow contrast which is essential for the signal formation in 3D TOF-MRA sequences.

The basis of TOF-MRA is that stationary tissue is partially saturated by the application of multiple RF pulses, whereas inflowing blood has a lower or no partial saturation, and hence gives a relative signal enhancement. This is called inflow contrast. With the MB technique, it is possible to improve the inflow contrast. Instead of acquiring data in a slab-by-slab manner (multislab acquisition) as it is traditionally done in 3D TOF-MRA imaging, it is possible to divide the thick slabs into thinner slabs and acquire several thinner slabs simultaneously. This way, each thin slab will be provided by fresh blood reaching the imaging plane which improves the inflow contrast. We called this new technique multiband multislab 3D time-of-flight magnetic resonance angiography (MB MS 3D TOF-MRA).

In this work, instead of acquiring three rather thick slabs to cover the whole brain, MB MS 3D TOF-MRA acquired three times three slabs simultaneously with a slab thickness reduced by a factor of 3. This also reduced the acquisition time by a factor of 3 while still covering the same whole brain field-of-view (FOV).

Data were acquired and evaluated from 6 subjects and showed that contrast-to-noise ratio could be maintained which leads to an increase in $\mathrm{CNR}/\sqrt{TA}$ compared to data acquired with the standard protocol. Due to the simultaneous acquisition of several thinner slabs, a strong inflow contrast could be observed in the MB-MS 3D TOF-MRA images. Additionally, the MB excitation pulses cause increased magnetization transfer contrast (MTC). Both characteristics lead to an improvement of the sharpness of the vessel borders which is reflected by higher full-width-at-half-maximum values of the vessel size and higher slopes of the vessel borders in the acquired images. In this chapter, it could therefore be shown that multiband imaging is capable of appreciably

accelerating acquisition times, and can combine the high spatial resolution of 3D imaging with the additional inflow contrast advantage of thinner slab acquisitions without introducing excessive noise arising from the MB reconstruction.

CHAPTER 3: Multiband echo shifted echo planar imaging

In chapter 2, the MB-technique was used to achieve several advantages with respect to the equivalent non-MB acquisition. Chapter 3 slightly changes the focus and showed how MB-imaging offers the possibility to use it in combination with other techniques to further push the acceleration capabilities.

While traditional multiband imaging will usually accelerate acquisitions by a factor equal to the multiband factor applied, it can however in certain situations be useful to combine the multiband technique with other methods to achieve an even higher acceleration factor.

In chapter 3, an application of multiband imaging was presented which combined the principles of echo-shifted acquisition for two-dimensional multislice EPI with both in-plane and multiband acceleration by means of partial parallel imaging techniques. We called this techniques multiband echo-shifted (MESH) echo planar imaging (EPI).

In some EPI acquisitions, there is sufficient dead time in between slice selection and the EPI readout to insert an additional EPI readout. The crusher gradients before the excitation pulse are then used to "select" a specific slice to be acquired. In combination with MB imaging, this will lead to higher acceleration factors for the MESH-EPI compared to standard MB-EPI acquisitions. For MESH-EPI to efficiently work, it is mandatory to provide enough "dead time" between an excitation and its matching read-out, therefore typical applications for MESH-EPI would be functional MRI (fMRI) experiments. Since the optimal contrast for fMRI with gradient echo EPI is obtained for $TE = T_2^*$ and the optimum echo times become considerably longer with decreasing field strength, MESH-EPI is particularly well suited for low field strengths and lower spatial resolutions.

To evaluate the implemented MESH-EPI sequence, data (acquired at 1.5T) were analysed from 6 subjects and compared to a standard EPI and MB-EPI sequence by means of temporal signal-to-noise (tSNR) measurements and resting state fMRI data. Data were acquired at 3mm isotropic resolution and an in-plane acceleration factor of 3 for all protocols. The MB-factor was 3 and MESH echo-shift (ES) factors were 1 and 2 respectively. It could be shown that the additional

gradient switching did not affect tSNR and further that functional results are qualitatively similar between the three methods.
Since the true acceleration factor in the MESH-EPI is consequently a combination of the multiband factor and the echo-shift factor, MESH-EPI would in this work accelerate the acquisition by a factor of 6 compared to the standard EPI for ES1 and even a factor of 9 for ES2.
It is further remarkable that for low resolution acquisitions, MESH-EPI is able to achieve very short volume TRs comparable entering the regime of ultrafast acquisition techniques such as inverse imaging ([83][27]). With the 3mm isotropic resolution, the volume TR was 232ms. However, going to lower resolutions such as 4mm/5mm isotropic while covering a similar field-of-view, the volume TR would decrease to 155ms/117ms, opening up the the possibility of short TR acquisitions without the need for complex reconstruction algorithms.
In this chapter, it could therefore be shown that a clever combination of the MB-technique with echo-shifting created an additional tool to standard MB-EPI which offers, in favorable circumstances, a further acceleration in image acquisition for fMRI at no loss in sensitivity.

CHAPTER 4: Whole brain, high resolution multiband spin-echo EPI fMRI at 7T: A comparison with gradient-echo EPI using a color-word Stroop task

In previous chapters, multiband imaging has only been applied in gradient-echo (GE) sequences. Since gradient-echo sequences only use a single excitation pulse, MB-pulses were solely applied. Applying SMS imaging techniques in spin-echo (SE) sequences, however, need further considerations.
The amplitude of the MB-pulse scales linearly with the multiband factor applied. Therefore, MB-pulses get easily demanding in terms of peak voltage, but also in terms of power deposition, especially when high multiband factors or high field strengths are used. Since power deposition is anyways a critical factor in spin-echo sequences, it is not possible to apply multiband excitation along with multiband refocusing pulses in a SE-sequence at 7T while setting up a suitable whole brain, high resolution fMRI-protocol.
In this chapter, we therefore used low SAR PINS ([102]) pulses as refocusing pulses. In combination with the MB-excitation pulse, arbitrary user-defined slice orientations are maintained and

comparable fMRI protocols for SMS spin-echo EPI and SMS gradient-echo EPI fMRI protocols could be realized.

This work was motivated by a previous successful SE EPI resting state fMRI study: "Whole brain, high resolution spin-echo resting state fMRI using PINS multiplexing at 7T" [71].

SE imaging at 7T is actually known for its specificity. However, in GE imaging all 4 BOLD contrast mechanisms contribute to the signal and it therefore profits from increased sensitivity. To compare the two sequences with whole brain task fMRI, data from 6 subjects were acquired at 7T while doing a color-word Stroop task. The color-word stroop task is known to give reliable activation in many regions of the brain including the frontal lobe. [106][136]

With an in-plane resolution of 1.5×1.5 mm^2 and a through-plane resolution of 1.3mm, both SE- and GE-EPI data have been shown to lie in the physiological noise regime. [151] Results showed that with respect to temporal efficiency, SMS GE-EPI has a higher tSNR compared to SMS SE-EPI at both the group and the individual subject level. GE also showed higher sensitivity due to mainly larger clusters than SE and higher CNR in the whole brain except for the visual cortex. The similarities between SMS SE-EPI and SMS GE-EPI in the visual cortex area could be caused by a high noise level in the SMS GE-EPI acquisition which could be seen from the residuals of the GLM. In SMS SE-EPI, signal changes and noise levels were generally lower compared to the SMS GE-EPI supporting the idea that the mechanism "extravascular dynamic dephasing" defining the SE-signal is further responsible for low noise levels. The remaining 3 contrast mechanisms seem neither to have an influence on the noise, nor on the signal changes.

Unexpectedly, we could show that SMS GE-EPI performed better in areas with large susceptibility gradients (inferior and anterior regions). Due to the fact that previous studies ([133], [127]) showed a benefit of thinner slices for reduced intra-voxel dephasing especially around air/tissue interfaces, our unexpected result could be caused by the high spatial resolution in the slice direction and the high sensitivity of 7T.

It could be concluded that SMS GE-EPI is an alternative to the theoretical advantages of SMS SE-EPI imaging for whole brain, high resolution, and task fMRI studies at 7T.

In the context of this thesis, however, it is noticeable that the combination of applying MB-pulses for excitation and PINS-pulses for refocusing, an SMS SE-EPI sequence could be created which is able to acquire whole brain fMRI data with a protocol not constrained by SAR-limitations.

CHAPTER 5: Clinical application of Half Fourier Acquisition Single Shot Turbo Spin Echo (HASTE) imaging accelerated by simultaneous multi-slice acquisition

As a SE-based sequence, HASTE acquisitions are easily limited by its high power deposition. This is particularly relevant at high spatial resolutions and high magnetic field strength. As introduced in chapter 4, it is possible to use a combination of traditional MB excitation and PINS refocusing pulses to effectively accelerate acquisition time of a sequence while staying within the SAR limitations.

The motivation for chapter 5 of this thesis was further given by previous work on "Application of PINS radiofrequency pulses to reduce power deposition in RARE/turbo spin echo imaging of the human head" [101].

The HASTE sequence used for this study was not only modified in terms of MB excitation and PINS refocusing pulses, but blipped CAIPIRINHA [138] and TRAPS [63] were additionally implemented. While blipped CAIPIRINHA improved the image reconstruction quality by shifting individual slices in the field-of-view, TRAPS reduced the applied flip angles along the echo train and therefore the power deposition. Compared to previous SMS-implementations of this thesis, it was possible to reconstruct this MB-PINS HASTE sequence online on the scanner due to a FLASH reference scan introduced at the beginning of the sequence.

In this chapter, a rather clinically oriented application of SMS HASTE imaging was presented. In the study, we evaluated whole brain MB-PINS HASTE data from 10 individuals and compared images in terms of diagnostic quality to a clinical HASTE protocol using an additional standard T2-TSE acquisition as reference. We aimed to develop the best possible MB-PINS HASTE protocol considering typical SMS imaging restrictions. While being similar to the clinical HASTE protocol, the focus with respect to the MB-PINS HASTE protocol was to drastically reduce the acquisition time giving best image quality. This led to some key imaging parameters differing from each other, as otherwise there would have been artefacts in the MB-PINS HASTE images.

It was shown that the MB-PINS HASTE sequence could not only effectively accelerate acquisition time, but image quality was comparable in both sequences. In fact, despite the fact that the MB-PINS HASTE sequence had a somewhat higher artefact level, the image quality in the perivascular CSF regions even proved to be better compared to the clinical HASTE.

The developed method will in particular be beneficial for uncooperative and young patients who could be diagnosed without the need for sedation. Further applications besides clinical T2-weighted imaging could be T2 fMRI acquisitions and diffusion weighted imaging. MB-PINS HASTE would also be suited to be applied in other parts of the body such as for instance the abdomen or the liver.

CHAPTER 6: Reduced peak power in paired excitation and refocusing multiband pulses by quadratic phase modulation

In traditional multiband imaging, both, the power deposition and amplitude of the RF pulse, depend linearly on the number of simultaneously excited slices making MB pulses rather demanding. Whereas the maximal power deposition is restricted by the specific absorption rate defined by the International Commission on Non-Ionizing Radiation Protection (ICNIRP) guidelines, the amplitude of the RF-pulses is limited by the maximal transmit voltage of the system. When high multiband factors are used, the maximum transmit voltage can easily be reached and clipping occurs. Therefore, several techniques have been introduced to reduce the peak voltage in multiband imaging.

In chapter 6, the focus was not mainly on the sequence implementation and application of the sequence as in previous chapters, but rather on the specific design of an RF-pulse which can be used to reduce the peak voltage in multiband imaging. The newly developed pulse is based on quadratic phase-modulations. By applying the modulation in the spatial domain to the Fourier transform of a standard Shinnar-Le-Roux pulse, the peak voltage could be drastically reduced by up to 50-60%. Additional peak voltage reduction methods, such as the Wong phase optimization scheme, are compatible with this technique and further voltage reduction of up to 70-80% in total could be achieved.

To avoid dephasing and signal loss, the pulses are restricted to spin-echo sequences only and need to be applied in matching excitation-refocusing pulse-pairs. It could however be seen that the generated slice profiles are of good quality showing a smooth plateau.

By introducing different simultaneous multi-slice techniques for MRI acquisitions, this thesis contributes to the ongoing research in the field of accelerating MRI acquisitions. Each chapter presents knowledge with results from SMS design, implementation, application and analysis. The presented work can in the future not only be used to improve acquisitions, but can also serve as a basis for further developments. With this ongoing research, magnetic resonance imaging will remain a power tool in future medical imaging and research.

Hoofdstuk 8

Samenvatting

Sinds de uitvinding van MRI scanners is het versnellen van de acquisitie een belangrijk verbeterpunt. Er zijn veel verschillende technieken ontwikkeld die dagelijks gebruikt worden bij het scannen. De 'multiband' (MB) en 'simultaneous multi-slice' (SMS) versnellingsmethoden worden al ruim tien jaar gebruikt in verschillende vormen om de $\sqrt{N}$ verlaging in signaal-ruisverhouding tegen te gaan.

Hoofdstuk 2 en 3 van dit proefschrift geven voorbeelden van hoe traditionele multiband acquisitie makkelijk gebruikt kan worden om de huidige standaarden te verbeteren. In hoofdstuk 2 wordt multiband beeldvorming toegepast in een 3D TOF-MRA sequentie. Hoofdstuk 3 beschrijft een voorbeeld van het versnellen van EPI met multiband beeldvorming in combinatie met echo-verschuiving. Hoofdstuk 4 vergelijkt SMS SE-EPI met een standaard SMS GE-EPI sequentie op 7T in een standaard fMRI experiment. Het volgende hoofdstuk 5 beschrijft een klinische toepassing van de combinatie van traditionele multiband en PINS pulsen om de acquisitietijd substantieel te verlagen zonder de SAR grenzen te overschrijden. Het laatste hoofdstuk 6 gaat over RF puls ontwerp van een nieuwe vorm van multiband pulsen om het maximale vermogen te verlagen dat toegepast kan worden als een excitatie-heroriëntatie puls paar in SE-gebaseerde sequenties.

CHAPTER 2: Multiband multislab 3D time-of-flight magnetic resonance angiography for reduced acquisition time and improved sensitivity

Multiband wordt vooral in 2D beeldvorming toegepast. Desondanks is deze versnellingstechniek niet beperkt tot laag-voor-laag (2D) beeldvorming, maar kan deze in sommige gevallen ook een nuttige manier zijn om 3D acquisities te versnellen.
De specifieke motivatie voor hoofdstuk 2 was niet alleen het gebruik van multiband beeldvorming om de lange acquisitietijd (TA) te verlagen van de 3D 'time-of-flight' magnetische resonantie angiografie, maar ook om het instroomcontrast te verbeteren, hetgeen essentieel is voor de signaalformatie van 3D TOF-MRA sequenties.
De basis van TOF-MRA is dat stationair weefsel gedeeltelijk verzadigd is door herhaaldelijk gebruik van RF pulsen, terwijl binnenstromend bloed een lagere of geen verzadiging, en daardoor een relatief groot aandeel in het signaal, heeft. Dit wordt het instroomcontrast genoemd. Met een MB techniek is het mogelijk om het instroomcontrast te verbeteren. In plaats van het gehele volume op een laag-voor-laag manier (multislab acquisitie) te verkrijgen, zoals traditioneel gedaan wordt in 3D TOF-MRA, is het mogelijk dikke lagen te verdelen in enkele dunnere lagen, en die dunnere lagen tegelijkertijd te scannen. Op deze manier wordt iedere dunne laag voorzien van vers bloed wat het instroomcontrast bevordert. Deze techniek hebben we 'multiband multislab 3D time-of-flight magnetic resonance angiography' (MB MS 3D TOF-MRA) genoemd.
Met een MB MS 3D TOF-MRA acquisitie kunnen we in plaats van drie dikke lagen die het hele brein beslaan, drie keer drie lagen tegelijkertijd scannen, die afzonderlijk drie keer zo dun zijn. Dit verlaagt de acquisitietijd met een factor drie, maar heeft een even groot gescand volume.
Scans zijn uitgevoerd op 6 proefpersonen. Analyse van deze data toonde aan dat de contrast-ruis verhouding behouden kon worden wat leidt tot een verhoogde contrast-ruis verhouding per tijdseenheid vergeleken met data uit een standaard protocol. Door het gelijktijdig verkrijgen van enkele dunne lagen konden we een stek instroomcontrast zien in de MB-MS 3D TOF-MRA beelden. Daarnaast bleken de MB excitatie pulsen een verhoogd magnetisatie overdracht contrast op te leveren. Beide karakteristieken leiden tot een verbetering van de scherpte van de bloedvat randen, wat te zien is aan een hogere halfwaardebreedte van de bloedvatdikte en stijlere hellingen van de bloedvatranden in de beelden.

In dit hoofdstuk hebben we dus aangetoond dat het mogelijk is met multiband beeldvorming de acquisitie met een factor drie te versnellen met behoud van de hoge resolutie van 3D beeldvorming en met het bijkomend voordeel van een verhoogd instroomcontrast van de dunnere lagen, zonder excessieve ruis te introduceren.

CHAPTER 3: Multiband echo shifted echo planar imaging

In hoofdstuk 2 hebben we een MB techniek gebruikt om enkele voordelen te behalen vergeleken met niet-MB sequenties. Hoofdstuk 3 verlegt de focus een beetje, en laat zien hoe MB beeldvorming de mogelijkheid geeft om gebruikt te worden in combinatie met andere technieken die samen een nog hogere versnelling van de aquisitie geven.
Waar traditionele multiband beeldvorming over het algemeen acquisities versnelt met een factor die even groot is als de multiband factor, kan het in sommige situaties ook nuttig zijn om multiband te combineren met andere methodes om een nog hogere versnelling te bewerkstelligen. In hoofdstuk 3 presenteerden we een toepassing van multiband beeldvorming die de principes van echo-verschuiving combineerde met twee-dimensionaal multi-laag EPI in zowel de binnenlaagse als multiband versnelling door het gebruik van patiële parallelle beeldvorming technieken. We hebben deze techniek 'multiband echo-shifted' (MESH) 'echo planar imaging' (EPI) genoemd.
In sommige EPI acquisities is er voldoende dode tijd tussen de laag selectie en de EPI uitlezing om een extra EPI uitlezing in te voegen. De Crusher gradiënten voor de excitatie puls worden dan gebruikt om een specifieke laag te "selecteren". In combinatie met MB beeldvorming kan dit leiden tot hogere versnelling factoren voor de MERSH-EPI vergeleken met standaard MB-EPI acquisities.
Om MESH-EPI efficiënt te laten werken moet er wel genoeg "dode tijd" tussen de excitatie en de bijbehorende uitlezing zitten. Daarom zijn voor de hand liggende toepassingen de functionele MRI (fMRI). Omdat het optimale contrast voor fMRI met gradiënt echo ligt bij een echotijd die gelijk is aan $TE = T_2^*$, en deze optimale echotijd ruim langer is bij lagere veldsterktes, is MESH-EPI zeer geschikt voor lage veldsterktes en lage spatiële resoluties.
Om de geïmplementeerde MESH-EPI sequentie te toetsen is de data van zes proefpersonen (op een veldsterkte van 1.5 Tesla) geanalyseerd en vergeleken met een standaard EPI en MB-EPI sequentie door midden van een temporele signaal-ruis analyse en fMRI in rusttoestand. De data werd gescand met een isotropische resolutie van 3 mm en een binnenlaagse versnellingsfactor

van drie, voor alle protocollen. De Multiband factor was drie en de MESH echoverschuiving factoren waren 1 en 2. We konden aantonen dat de extra gradiëntwisseling geen verschil maakt voor de tSNR en dat verdere functionele resultaten kwalitatief vergelijkbaar waren tussen de drie methodes.
Doordat de daadwerkelijke versnellingsfactor in de MESH-EPI een combinatie is van de multiband factor en de echoverschuivingsfactor, is de eigenlijke versnelling van MESH-EPI een factor 6 vergeleken met de standaard EPI voor ES1 en zelfs een factor 9 voor ES2.
Verder is het opmerkelijk dat de MESH-EPI zeer korte volume repetitietijden kan behalen op lage resoluties, die in de buurt komen van vergelijkbare ultrasnelle acquisities zoals inversie beeldvorming ([83][27]). Met de 3 mm isotropische resoluties was de volume TR 232 ms. Als je echter naar nog lagere resoluties gaat, zoals 4 mm of 5 mm met hetzelfde scanvolume, dan kan de TR verlaagd worden naar 155 ms/ 117 ms, wat de mogelijkheid biedt voor lagere TR acquisities zonder dat complexe reconstructie algoritmes noodzakelijk zijn.
In dit hoofdstuk hebben we aldus laten zien dat een slimme combinatie van de multiband techniek en echoverschuiving een nieuwe manier geeft om standaard MB-EPI nog meer te versnellen voor fMRI zonder een verlies in sensitiviteit.

CHAPTER 4: Whole brain, high resolution multiband spin-echo EPI fMRI at 7T: A comparison with gradient-echo EPI using a color-word Stroop task

In de vorige hoofdstukken is multiband beeldvorming alleen toegepast op gradiënt echo (GE) sequenties. Omdat gradiënt echo sequenties slechts een enkele excitatiepuls gebruiken was alleen een MB puls toegepast. Het gebruiken van SMS technieken in spin-echo (echo) sequenties vergt echter meer overweging.
De amplitude van de MB pulsen schaalt lineair met de toegepaste multiband factor. Daarom worden MB pulsen makkelijk veeleisend in termen van het piek voltage, maar ook in termen van vermogen depositie, vooral wanneer hoge multiband factoren or hoge veldsterktes gebruikt worden. Omdat de vermogen depositie sowieso een kritieke factor is bij spin-echo sequenties is het niet mogelijk multiband excitatie te gebruiken in combinatie met een multiband heroriëntatiepuls in een SE sequentie op 7T als men het gehele brein op hoge resolutie wil scannen.

In dit hoofdstuk hebben we daarom lage SAR PINS ([102]) pulsen gebruikt als heroriëntatie pulsen. In combinatie met de MB excitatie puls kan een willekeurig door de gebruiker gespecificeerd oriëntatie behouden blijven in vergelijkbare fMRI protocollen en kunnen SMS spin-echo EPI en SMS gradiënt echo EPI fMRI gerealiseerd worden.

Aan de basis van dit werk ligt een eerdere succesvolle SE EPI fMRI studie in rusttoestand: "Whole brain, high resolution spin-echo resting state fMRI using PINS multiplexing at 7T" [71].

SE beeldvorming op 7T staat bekend om zijn specificiteit. Echter, in GE beeldvorming dragen alle vier verschillende BOLD contrast mechanismen bij aan het signaal en heeft het daardoor meer sensitiviteit.

Om de twee sequenties te vergelijken met fMRI in het hele brein, is dat van 6 proefpersonen gescand op 7T terwijl ze een kleur-woord Stroop taak deden. Deze kleur-woord Stroop taak is een betrouwbare manier om activiteit te meten in veel regio's in het hele brein, inclusief de frontaalkwab [106][136]

Met een binnenlaagse resolutie van 1.5×1.5 mm^2 en tussenlaagse resolutie van 1.3 mm liggen zowel SE als GE EPI in het fysiologische ruis regime [151]. De resultaten lieten zien dat SMS GE-EPI een hogere tSNR heeft vergeleken met SMS SE-EPI op zowel individueel niveau als groepsniveau, bij een vergelijking van de temporele efficiëntie. GE liet ook een hogere sensitiviteit zien, vooral vanwege grotere clusters, dan SE en hogere CNR in het hele brein behalve de visuele cortex. De overeenkomsten tussen SMS SE-EPI en SMS GE-EPI in de visuele cortex zouden veroorzaakt kunnen zijn door een hoog ruis-niveau in de SMS GE-EPI acquisitie, zoals te zien valt in de residuen van de GLM.

In SMS SE-EPI waren de signaalverschillen en ruisniveaus over het algemeen lager vergeleken met SMS GE-EPI, hetgeen het idee ondersteunt dat het mechanisme 'extravasculaire dynamische uitfasering', wat het SE signaal definieert, verder verantwoordelijk is voor het lage ruisniveau. De overgebleven drie contrast mechanismen lijken geen invloed te hebben op de ruis en ook niet op de signaalverschillen.

We konden onverwachts aantonen dat SMS GE-EPI beter presteerde in regio's met hoge susceptibiliteitgradiënten (inferiore en anteriore regio's). Omdat eerder studies ([133], [127]) aangetoond hebben dat dunnere lagen de intra-voxel uitfasering verlaagt, vooral rondom lucht/weefsel oppervlakte, kan dit onverwachte resultaat veroorzaakt worden door de hoge resolutie in de laag-richting en de hoge sensitiviteit van 7T.

Het kan geconcludeerd worden dat SMS GE-EPI een alternatief is voor het theoretische voordeel

van SMS SE-EPI voor het scannen van het hele brein op hoge resolutie en taak-fMRI studies op 7T. In de context van dit proefschrift is het opmerkelijk dat met de gecombineerde toepassing van MB pulsen voor excitatie en PINS pulsen voor heroriëntatie een SMS SE-EPI sequentie gecreëerd kon worden die de acquisitie van het hele brein in fMRI data kan bewerkstelligen met een protocol dat niet beperkt is door SAR.

CHAPTER 5: Clinical application of Half Fourier Acquisition Single Shot Turbo Spin Echo (HASTE) imaging accelerated by simultaneous multi-slice acquisition

De HASTE sequentie is, als SE gebaseerde sequentie, makkelijk gelimiteerd door de hoge vermogen depositie. Dit is bijzonder relevant op hoge spatiële resolutie en hoge veldsterkte. Zoals hoofdstuk 4 heeft geïntroduceerd is het mogelijk om een combinatie van traditionele multiband excitatie en PINS heroriëntatie pulsen te gebruiken om de acquisitietijd van een sequentie effectief te verlagen, maar toch binnen de SAR beperkingen te blijven.
Hoodfstuk 5 van dit proefschrift was verder gemotiveerd door eerder werk in "Application of PINS radiofrequency pulses to reduce power deposition in RARE/turbo spin echo imaging of the human head" [101].
De HASTE sequentie die gebruikt is voor deze studie is niet alleen aangepast in termen van MB excitatie en PINS heroriëntatie, maar 'blipped CAIPIRINHA [138] en TRAPS [63] zijn ook geïmplementeerd. Waar blipped CAIPIRINHA de reconstructie van de beelden verbetert door de individuele lagen ten opzichte van elkaar te verschuiven binnen het gescande volume, verlaagt TRAPS de gebruikte fliphoek over de echo rij en daarmee de vermogen depositie. Vergeleken met eerdere implementaties van SMS in dit proefschrift was het mogelijk om de MB-INS HASTE sequentie online te reconstrueren bij de scanner, gebruik makend van de FLASH referentie scan die toegevoegd was aan het begin van de sequentie.
In dit hoofdstuk wordt een klinisch georiënteerde toepassing van SMS HASTE beeldvorming gepresenteerd. In deze studie hebben we heel-brein MB-PINS HASTE data van 10 proefpersonen geëvalueerd en hebben we de beelden vergeleken in termen van diagnosticeerbare kwaliteiten met een klinisch HASTE protocol, gebruik makend van een extra standaard T2-TSE acquisitie als referentie. Ons doel was het ontwikkelen van het best mogelijke MB-PINS HASTE protocol,

met in acht neming van typische SMS beeldvorming beperkingen. Al was het klinische protocol zeer gelijkend op het MB-PINS protocol, het laatste reduceert de acquisitietijd drastisch en geeft betere beeldkwaliteit. Hierbij moesten een aantal belangrijke parameters veranderd worden, om artefacten in de MB-PINS HASTE beelden te voorkomen.
We hebben aangetoond dat de MB-PINS HASTE sequentie niet alleen de acquisitietijd versnelt, maar ook de beeldkwaliteit in beide sequenties behoudt. Daarbij komt nog dat ondanks het iets hogere artefactniveau de perivasculaire CSF regio's beter bleken te zijn dan in de klinische HASTE.
Deze ontwikkelde methode zal bij uitstek voordelig zijn bij oncoöperatieve en jonge patiënten die hiermee gediagnostiseerd kunnen worden zonder een noodzaak voor narcose. Andere toepassingen naast klinische T2-gewogen beelden kunnen gevonden worden in T2 functionele MRI acquisities en diffusie beeldvorming. MB-PINS HASTE kan ook makkelijk gebruikt worden in andere delen van het lichaam dan het brein, zoals bijvoorbeeld de onderbuik of de lever.

CHAPTER 6: Reduced peak power in paired excitation and refocusing multiband pulses by quadratic phase modulation

In traditionele MB beeldvorming zijn zowel de vermogen depositie als de amplitude van de RF puls lineair afhankelijk van het aantal gelijktijdig geëxiteerde lagen, waardoor MB pulsen behoorlijk veeleisend zijn. Waar de maximale vermogen depositie beperkt is door de specifieke absorptie snelheid (SAR), die gedefinieerd is door de regelgeving van de Internationale Commissie voor niet-ioniserende straling bescherming (ICNIRP), is de amplitude van de RF pulsen gelimiteerd door het maximale zendvoltage van het systeem. Wanneer hoge multiband factoren gebruikt worden kan het maximum zendvoltage makkelijk bereikt worden. Om dit te voorkomen zijn er enkele technieken geïntroduceerd om het piekvoltage te reduceren.
In hoofdstuk 6 lag de focus niet zozeer op de implementatie en toepassing van de sequentie, zoals in de vorige hoofdstukken, maar meer op het specifieke ontwerp van een RF puls die gebruikt kan worden om het piekvoltage te reduceren in multiband beeldvorming. De nieuw ontworpen puls is gebaseerd op kwadratische fase modulatie. Door het toepassen van een modulatie in het spatiële domein van de Fourier transformatie van een standaard Shinnar-Le Roux puls kan het

piekvoltage drastisch gereduceerd worden, tot wel 50-60%. Verdere piekreductie technieken, zoals een Wong fase optimalisatie schema, zijn verenigbaar met deze techniek en kunnen leiden tot een verdere voltagereductie van 70-80%.
Om signaalverlies en uit fase raken te voorkomen, zijn de pulsen gelimiteerd tot alleen spin-echo sequenties en moeten ze toegepast worden in gekoppelde excitatie-heroriëntatie puls paren. Het werd echter duidelijk dat de gegenereerde laagprofielen van goede kwaliteit waren en een glad plateau vormen.

Met het introduceren van verschillende 'simultaneous multi-slice' technieken aan MRI acquisities draagt dit proefschrift bij aan het lopende onderzoek in het veld van MRI acquisitieversnelling. Ieder hoofdstuk presenteert kennis met resultaten van SMS ontwerp, implementatie, toepassing en analyse. Dit werk kan niet alleen gebruikt worden voor het verbeteren van de acquisitie, het kan ook de basis vormen van verdere ontwikkelingen. Met dit voortdurende onderzoek kan magnetische resonantie beeldvorming een belangrijk middel blijven voor toekomstige medische beeldvorming en onderzoek.

Bibliography

[1] T. Ai, J. N. Morelli, X. Hu, D. Hao, F. L. Goerner, B. Ager, and V. M. Runge. A historical overview of magnetic resonance imaging, focusing on technological innovations. *Investigative radiology*, 47(12):725–741, 2012.

[2] D. C. Alsop. The sensitivity of low flip angle RARE imaging. *Magnetic Resonance in Medicine*, 37(2):176–184, feb 1997.

[3] J. Assländer, B. Zahneisen, T. Hugger, M. Reisert, H.-L. Lee, P. LeVan, and J. Hennig. Single shot whole brain imaging using spherical stack of spirals trajectories. *NeuroImage*, 73:59–70, jun 2013.

[4] E. J. Auerbach, J. Xu, E. Yacoub, S. Moeller, and K. Uğurbil. Multiband accelerated spin-echo echo planar imaging with reduced peak rf power using time-shifted rf pulses. *Magnetic Resonance in Medicine*, 69(5):1261–1267, 2013.

[5] L. Axel. Blood flow effects in magnetic resonance imaging. *American Journal of Roentgenology*, 143(6):1157–1166, dec 1984.

[6] P. Balchandani, J. Pauly, and D. Spielman. Designing adiabatic radio frequency pulses using the shinnar-le roux algorithm. *Magn Reson Med*, 64(3):843–851, Sept. 2010.

[7] P. A. Bandettini, E. C. Wong, R. S. Hinks, R. S. Tikofsky, and J. S. Hyde. Time course epi of human brain function during task activation. *Magn Reson Med*, 25(2):390–7, Jun 1992.

[8] M. Barth, F. Breuer, P. J. Koopmans, D. G. Norris, and B. A. Poser. Simultaneous multislice (SMS) imaging techniques. *Magnetic Resonance in Medicine*, 75(1):63–81, aug 2015.

[9] C. F. Beckmann, M. Jenkinson, and S. M. Smith. General multilevel linear modeling for group analysis in FMRI. *NeuroImage*, 20(2):1052–1063, oct 2003.

[10] M. A. Bernstein, K. F. King, and X. J. Zhou. *Handbook of MRI pulse sequences*. Elsevier, 2004.

[11] M. Blaimer, F. A. Breuer, N. Seiberlich, M. F. Mueller, R. M. Heidemann, V. Jellus, G. Wiggins, L. L. Wald, M. A. Griswold, and P. M. Jakob. Accelerated volumetric MRI with a SENSE/GRAPPA combination. *Journal of Magnetic Resonance Imaging*, 24(2):444–450, 2006.

[12] A. M. Blamire, S. Ogawa, K. Ugurbil, D. Rothman, G. McCarthy, J. M. Ellermann, F. Hyder, Z. Rattner, and R. G. Shulman. Dynamic mapping of the human visual cortex by high-speed magnetic resonance imaging. *Proc Natl Acad Sci U S A*, 89(22):11069–73, Nov 1992.

[13] F. Bloch. Nuclear induction. *Physical review*, 70(7-8):460, 1946.

[14] R. Boyacioğlu and M. Barth. Generalized iNverse imaging (GIN): Ultrafast fMRI with physiological noise correction. *Magnetic Resonance in Medicine*, 70(4):962–971, oct 2012.

[15] R. Boyacioğlu, C. F. Beckmann, and M. Barth. An investigation of RSN frequency spectra using ultra-fast generalized inverse imaging. *Frontiers in Human Neuroscience*, 7, 2013.

[16] R. Boyacioğlu, J. Schulz, P. J. Koopmans, M. Barth, and D. G. Norris. Improved sensitivity and specificity for resting state and task fMRI with multiband multi-echo EPI compared to multi-echo EPI at 7T. *NeuroImage*, 119:352–361, oct 2015.

[17] R. Boyacioğlu, J. Schulz, and D. G. Norris. Multiband echo-shifted echo planar imaging. *Magnetic Resonance in Medicine*, jun 2016.

[18] M. Brant-Zawadzki and G. Gillan. Extracranial carotid magnetic resonance angiography. *Cardiovascular and Interventional Radiology*, 15(1):82–90, feb 1992.

[19] F. Breuer, M. Blaimer, R. Heidemann, M. Mueller, M. Griswold, and P. Jakob. Controlled aliasing in parallel imaging results in higher acceleration (caipirinha) for multi-slice imaging. *Magn Reson Med*, 53:684–691, 2005.

[20] R. W. Brown, Y.-C. N. Cheng, E. M. Haacke, M. R. Thompson, and R. Venkatesan. *Magnetic resonance imaging: physical principles and sequence design*. John Wiley & Sons, 2014.

[21] J. Budde, G. Shajan, M. Zaitsev, K. Scheffler, and R. Pohmann. Functional MRI in human subjects with gradient-echo and spin-echo EPI at 9.4 T. *Magnetic Resonance in Medicine*, 71(1):209–218, feb 2013.

[22] R. B. Buxton. The elusive initial dip. *Neuroimage*, 13(6 Pt 1):953–8, Jun 2001.

[23] R. B. Buxton, E. C. Wong, and L. R. Frank. Dynamics of blood flow and oxygenation changes during brain activation: the balloon model. *Magn Reson Med*, 39(6):855–64, Jun 1998.

[24] S. Byott and I. Harris. Rapid acquisition axial and coronal t2 HASTE MR in the evaluation of acute abdominal pain. *European Journal of Radiology*, 85(1):286–290, jan 2016.

[25] P. T. Callaghan. *Principles of nuclear magnetic resonance microscopy*, volume 3. Clarendon Press Oxford, 1991.

[26] S. Cauley, J. Polimeni, H. Bhat, L. Wald, and K. Setsompop. Interslice leakage artifact reduction technique for simultaneous multislice acquisitions. *Magn Reson Med*, 2013.

[27] W.-T. Chang, A. Nummenmaa, T. Witzel, J. Ahveninen, S. Huang, K. W.-K. Tsai, Y.-H. Chu, J. R. Polimeni, J. W. Belliveau, and F.-H. Lin. Whole-head rapid fMRI acquisition using echo-shifted magnetic resonance inverse imaging. *NeuroImage*, 78:325–338, sep 2013.

[28] L. Chen, A. T. Vu, J. Xu, S. Moeller, K. Ugurbil, E. Yacoub, and D. Feinberg. Evaluation of highly accelerated simultaneous multi-slice EPI for fMRI. *NeuroImage*, 104:452–459, jan 2015.

[29] S. Conolly, D. Nishimura, A. Macovski, and G. Glover. Variable-rate selective excitation. *Journal of Magnetic Resonance (1969)*, 78(3):440–458, jul 1988.

[30] Y. Crémillieux, S. Ding, and J. F. Dunn. High-resolutionin vivo measurements of transverse relaxation times in rats at 7 Tesla. *Magnetic Resonance in Medicine*, 39(2):285–290, feb 1998.

[31] R. Damadian. Tumor detection by nuclear magnetic resonance. *Science*, 171(3976):1151–1153, 1971.

[32] P.-F. V. de Moortele, C. Akgun, G. Adriany, S. Moeller, J. Ritter, C. M. Collins, M. B. Smith, J. T. Vaughan, and K. Uğurbil. B1 destructive interferences and spatial phase patterns at 7 T with a head transceiver array coil. *Magnetic Resonance in Medicine*, 54(6):1503–1518, 2005.

[33] R. Deichmann, J. Gottfried, C. Hutton, and R. Turner. Optimized EPI for fMRI studies of the orbitofrontal cortex. *NeuroImage*, 19(2):430–441, jun 2003.

[34] L. R. Dice. Measures of the amount of ecologic association between species. *Ecology*, 26(3):297–302, jul 1945.

[35] A. J. Duerinckx, W. D. Yu, S. El-Saden, D. Kim, J. C. Wang, and H. S. Sandhu. MR imaging of cervical spine motion with HASTE. *Magnetic Resonance Imaging*, 17(3):371–381, apr 1999.

[36] T. Q. Duong, E. Yacoub, G. Adriany, X. Hu, K. Uğurbil, and S.-G. Kim. Microvascular BOLD contribution at 4 and 7 T in the human brain: Gradient-echo and spin-echo fMRI with suppression of blood effects. *Magnetic Resonance in Medicine*, 49(6):1019–1027, may 2003.

[37] R. R. Edelman, S. S. Ahn, D. Chien, W. Li, A. Goldmann, M. Mantello, J. Kramer, and J. Kleefield. Improved time-of-flight MR angiography of the brain with magnetization transfer contrast. *Radiology*, 184(2):395–399, aug 1992.

[38] W. A. Edelstein, J. M. S. Hutchison, G. Johnson, and T. Redpath. Spin warp nmr imaging and applications to human whole-body imaging. *Physics in Medicine and Biology*, 25(4):751, 1980.

[39] C. Eichner, K. Setsompop, P. J. Koopmans, R. Lützkendorf, D. G. Norris, R. Turner, L. L. Wald, and R. M. Heidemann. Slice accelerated diffusion-weighted imaging at ultra-high field strength. *Magnetic Resonance in Medicine*, 71(4):1518–1525, 2014.

[40] C. Eichner, L. L. Wald, and K. Setsompop. A low power radiofrequency pulse for simultaneous multislice excitation and refocusing. *Magnetic Resonance in Medicine*, 72(4):949–958, 2014.

[41] S. Engel. Retinotopic organization in human visual cortex and the spatial precision of functional MRI. *Cerebral Cortex*, 7(2):181–192, mar 1997.

[42] D. C. V. Essen, S. M. Smith, D. M. Barch, T. E. Behrens, E. Yacoub, and K. Ugurbil. The WU-minn human connectome project: An overview. *NeuroImage*, 80:62–79, oct 2013.

[43] A. J. Evans, R. A. Blinder, R. J. Herfkens, C. E. Spritzer, D. O. Kuethe, E. K. Fram, and L. W. Hedlund. Effects of turbulence on signal intensity in gradient echo images. *Investigative Radiology*, 23(7):512–518, jul 1988.

[44] F. Fazekas, J. Chawluk, A. Alavi, H. Hurtig, and R. Zimmerman. Mr signal abnormalities at 1.5t in alzheimer's dementia and normal aging. *American Journal of Roentgenology*, 149(2):351–356, aug 1987.

[45] D. Feinberg, S. Moeller, S. Smith, E. Auerbach, S. Ramanna, M. Glasser, K. Miller, K. Ugurbil, and E. Yacoub. Multiplexed echo planar imaging for sub-second whole brain fmri and fast diffusion imaging. *PLoS One 2010*, 5:e15710, 2010.

[46] F. A. Fellner, M. Requardt, W. Lang, C. Fellner, W. Bautz, and A. Cavallaro. Peripheral vessels: MR angiography with dedicated phased-array coil with large–field-of-view adapter—feasibility study. *Radiology*, 228(1):284–289, jul 2003.

[47] J. Frahm, K.-D. Merboldt, and W. Hänicke. Functional MRI of human brain activation at high spatial resolution. *Magnetic Resonance in Medicine*, 29(1):139–144, jan 1993.

[48] S. Ganger, A. Hahn, M. Küblböck, G. S. Kranz, M. Spies, T. Vanicek, R. Seiger, R. Sladky, C. Windischberger, S. Kasper, and R. Lanzenberger. Comparison of continuously acquired resting state and extracted analogues from active tasks. *Human Brain Mapping*, 36(10):4053–4063, jul 2015.

[49] A. G. Gardener, S. T. Francis, M. Prior, A. Peters, and P. A. Gowland. Dependence of blood r2 relaxivity on CPMG echo-spacing at 2.35 and 7 T. *Magnetic Resonance in Medicine*, 64(4):967–974, aug 2010.

[50] A. Gibson, A. M. Peters, and R. Bowtell. Echo-shifted multislice EPI for high-speed fMRI. *Magnetic Resonance Imaging*, 24(4):433–442, may 2006.

[51] G. Glover, S. Lai, and S. Ca. Reduction of susceptibility effects in bold fmri using tailored rf pulses. In *Proceedings of the 6th Annual Meeting of ISMRM, Sydney, Australia*, 1998.

[52] G. H. Glover. 3D z-shim method for reduction of susceptibility effects in BOLD fMRI. *Magnetic Resonance in Medicine*, 42(2):290–299, aug 1999.

[53] G. Goelman. Two methods for peak rf power minimization of multiple inversion-band pulses. *Magn Reson Med*, 37:658–665, 1997.

[54] L. Griffanti, G. Salimi-Khorshidi, C. F. Beckmann, E. J. Auerbach, G. Douaud, C. E. Sexton, E. Zsoldos, K. P. Ebmeier, N. Filippini, C. E. Mackay, S. Moeller, J. Xu, E. Yacoub, G. Baselli, K. Ugurbil, K. L. Miller, and S. M. Smith. ICA-based artefact removal and accelerated fMRI acquisition for improved resting state network imaging. *NeuroImage*, 95:232–247, jul 2014.

[55] M. A. Griswold, P. M. Jakob, R. M. Heidemann, M. Nittka, V. Jellus, J. Wang, B. Kiefer, and A. Haase. Generalized autocalibrating partially parallel acquisitions (grappa). *Magnetic Resonance in Medicine*, 47(6):1202–1210, 2002.

[56] E. L. Hahn. Spin echoes. *Physical Review*, 80(4):580, 1950.

[57] S. Haller, E. Kövari, F. Herrmann, V. Cuvinciuc, A. Tomm, G. Zulian, and C. Bouras. Do brain t2/flair white matter hyperintensities correspond to myelin loss in normal aging? a radiologic-neuropathologic correlation study. *Acta neuropathologica communications*, 1(1), 2013.

[58] J. Harmer, R. M. Sanchez-Panchuelo, R. Bowtell, and S. T. Francis. Spatial location and strength of BOLD activation in high-spatial-resolution fMRI of the motor cortex: a comparison of spin echo and gradient echo fMRI at 7 T. *NMR in Biomedicine*, 25(5):717–725, sep 2011.

[59] M. P. Hartung, T. M. Grist, and C. J. François. Magnetic resonance angiography: current status and future directions. *Journal of Cardiovascular Magnetic Resonance*, 13(1):19, 2011.

[60] J. Hennig. Multiecho imaging sequences with low refocusing flip angles. *Journal of Magnetic Resonance (1969)*, 78(3):397–407, jul 1988.

[61] J. Hennig. Chemical shift imaging with phase-encoding rf pulses. *Magn Reson Med*, 25:289–298, 1992.

[62] J. Hennig, A. Nauerth, and H. Friedburg. Rare imaging: a fast imaging method for clinical mr. *Magnetic Resonance in Medicine*, 3(6):823–833, 1986.

[63] J. Hennig, M. Weigel, and K. Scheffler. Multiecho sequences with variable refocusing flip angles: Optimization of signal behavior using smooth transitions between pseudo steady states (TRAPS). *Magnetic Resonance in Medicine*, 49(3):527–535, feb 2003.

[64] D. I. Hoult. Sensitivity and power deposition in a high-field imaging experiment. *Journal of Magnetic Resonance Imaging*, 12(1):46–67, 2000.

[65] M. E. Huber, S. Kozerke, K. P. Pruessmann, J. Smink, and P. Boesiger. Sensitivity-encoded coronary MRA at 3T. *Magnetic Resonance in Medicine*, 52(2):221–227, 2004.

[66] S. Johst, S. Orzada, A. Fischer, L. Schäfer, K. Nassenstein, L. Umutlu, T. Lauenstein, M. Ladd, and S. Maderwald. Sequence comparison for non-enhanced mra of the lower extremity arteries at 7 tesla. *PloS one*, 9:e86274, 2014.

[67] S. Johst, K. Wrede, M. Ladd, and S. Maderwald. Time-of-flight magnetic resonance angiography at 7 t using venous saturation pulses with reduced flip angles. *Investig Radiol*, 47:445–450, 2012.

[68] U. Katscher and P. BÃűrnert. Parallel RF transmission in MRI. *NMR in Biomedicine*, 19(3):393–400, 2006.

[69] M. P. t. Kleinnijenhuis. *Imaging fibres in the brain, Donders Series #159*. PhD thesis, Radboud University Nijmegen, Nijmegen, The Netherlands, 2014.

[70] D.-M. Koh, M. Blackledge, A. R. Padhani, T. Takahara, T. C. Kwee, M. O. Leach, and D. J. Collins. Whole-body diffusion-weighted MRI: Tips, tricks, and pitfalls. *American Journal of Roentgenology*, 199(2):252–262, aug 2012.

[71] P. Koopmans, R. Boyacioglu, M. Barth, and D. Norris. Whole brain, high resolution spin-echo resting state fmri using pins multiplexing at 7t. *Neuroimage*, 62(3):1939–1946, 2012.

[72] P. J. Koopmans. Two-dimensional-NGC-SENSE-GRAPPA for fast, ghosting-robust reconstruction of in-plane and slice-accelerated blipped-CAIPI echo planar imaging. *Magnetic Resonance in Medicine*, 77(3):998–1009, mar 2016.

[73] F. Korosec. *Basic principles of MRI and MR Angiography*. Magnetic resonance angiography: principles and applications, Springer, 2012.

[74] A. Kumar, D. Welti, and R. R. Ernst. Nmr fourier zeugmatography. *Journal of magnetic resonance*, 213(2):495–509, 2011.

[75] K. K. Kwong, J. W. Belliveau, D. A. Chesler, I. E. Goldberg, R. M. Weisskoff, B. P. Poncelet, D. N. Kennedy, B. E. Hoppel, M. S. Cohen, and R. Turner. Dynamic magnetic resonance imaging of human brain activity during primary sensory stimulation. *Proc Natl Acad Sci U S A*, 89(12):5675–9, Jun 1992.

[76] D. Larkman, J. Hajnal, A. Herlihy, G. Coutts, I. Young, and G. Ehnholm. Use of multicoil arrays for separation of signal from multiple slices simultaneously excited. *J Magnetic Resonance Imaging*, 13:313–317, 2001.

[77] G. Laub. Displays for MR angiography. *Magnetic Resonance in Medicine*, 14(2):222–229, may 1990.

[78] P. C. Lauterbur. Image formation by induced local interactions: examples employing nuclear magnetic resonance. *Nature*, 242(5394):190–191, 1973.

[79] P. Le Van, B. Zahneisen, T. Grotz, and J. Hennig. A simultaneous eeg and high temporal resolution fmri study of trial-by-trial fluctuations in visual evoked potentials. In *Proceedings of the 19th Annual Meeting of ISMRM, Montreal, Quebec, Canada*, 2011.

[80] S.-P. Lee, A. C. Silva, K. Ugurbil, and S.-G. Kim. Diffusion-weighted spin-echo fMRI at 9.4 T: Microvascular/tissue contribution to BOLD signal changes. *Magnetic Resonance in Medicine*, 42(5):919–928, nov 1999.

[81] M. H. Levitt. *Spin dynamics: basics of nuclear magnetic resonance*. John Wiley & Sons, 2001.

[82] A.-L. Lin, Q. Qin, X. Zhao, and T. Q. Duong. Blood longitudinal (t 1) and transverse (t 2) relaxation time constants at 11.7 Tesla. *Magnetic Resonance Materials in Physics, Biology and Medicine*, 25(3):245–249, nov 2011.

[83] F.-H. Lin, L. L. Wald, S. P. Ahlfors, M. S. HämälÃd'inen, K. K. Kwong, and J. W. Belliveau. Dynamic magnetic resonance inverse imaging of human brain function. *Magnetic Resonance in Medicine*, 56(4):787–802, 2006.

[84] A. Litt, E. Eidelman, R. Pinto, T. Riles, S. McLachlan, S. Schwartzenberg, J. Weinreb, and I. Kricheff. Diagnosis of carotid artery stenosis: Comparison of 2Dft time-of-flight MR angiography with contrast angiography in 50 patients. *Am J Neuroradiol*, 12:149–154, 1991.

[85] J. Magland and C. L. Epstein. Practical pulse synthesis via the discrete inverse scattering transform. *Journal of Magnetic Resonance*, 172(1):63–78, jan 2005.

[86] M. Makki, M. Graves, and D. Lomas. Interactive body magnetic resonance fluoroscopy using modified single-shot half-Fourier rapid acquisition with relaxation enhancement (RARE) with multiparameter control. *Journal of Magnetic Resonance Imaging*, 16(1):85–93, jun 2002.

[87] J. B. Mandeville, J. J. Marota, C. Ayata, G. Zaharchuk, M. A. Moskowitz, B. R. Rosen, and R. M. Weisskoff. Evidence of a cerebrovascular postarteriole windkessel with delayed compliance. *J Cereb Blood Flow Metab*, 19(6):679–89, Jun 1999.

[88] P. Mansfield. Multi-planar image formation using nmr spin echoes. *Journal of Physics C: Solid State Physics*, 10(3):L55, 1977.

[89] P. Mansfield and P. K. Grannell. "diffraction" and microscopy in solids and liquids by NMR. *Physical Review B*, 12(9):3618–3634, nov 1975.

[90] P. Mansfield and A. Maudsley. Medical imaging by nmr. *The British journal of radiology*, 50(591):188–194, 1977.

[91] J. P. Marques, T. Kober, G. Krueger, W. van der Zwaag, P.-F. V. de Moortele, and R. Gruetter. MP2rage, a self bias-field corrected sequence for improved segmentation and t1-mapping at high field. *NeuroImage*, 49(2):1271–1281, jan 2010.

[92] A. Maudsley. Multiple-line-scanning spin density imaging. *Journal of Magnetic Resonance (1969)*, 41(1):112–126, oct 1980.

[93] T. R. McCauley, A. Monib, K. W. Dickey, J. Clemett, G. H. Meier, T. K. Egglin, R. J. Gusberg, M. Rosenblatt, and J. S. Pollak. Peripheral vascular occlusive disease: accuracy and reliability of time-of-flight MR angiography. *Radiology*, 192(2):351–357, aug 1994.

[94] A. A. Michelson. The relative motion of the earth and of the luminiferous ether. *American Journal of Science*, (128):120–129, 1881.

[95] M. Miyazaki, F. Kojima, N. Ichinose, Y. Onozato, and H. Igarashi. A novel saturation transfer contrast method for 3D time-of-flight magnetic resonance angiography: A slice-selective off-resonance sinc pulse (SORS) technique. *Magnetic Resonance in Medicine*, 32(1):52–59, jul 1994.

[96] M. Miyazaki and V. S. Lee. Nonenhanced MR angiography. *Radiology*, 248(1):20–43, jul 2008.

[97] S. Moeller, E. Yacoub, C. Olman, E. Auerbach, J. Strupp, N. Harel, and K. Uğurbil. Multiband multislice ge-epi at 7 tesla, with 16-fold acceleration using partial parallel imaging with application to high spatial and temporal whole-brain fmri. *Magn Reson Med*, 63:1144–1153, 2010.

[98] C. T. W. Moonen, G. Liu, P. V. Gelderen, and G. Sobering. A fast gradient-recalled MRI technique with increased sensitivity to dynamic susceptibility effects. *Magnetic Resonance in Medicine*, 26(1):184–189, jul 1992.

[99] R. Mulkern, S. Wong, C. Winalski, and F. Jolesz. Contrast manipulation and artifact assessment of 2D and 3D RARE sequences. *Magnetic Resonance Imaging*, 8(5):557–566, jan 1990.

[100] S. Müller. Multifrequency selective rf pulses for multislice MR imaging. *Magnetic Resonance in Medicine*, 6(3):364–371, mar 1988.

[101] D. Norris, R. Boyacioğlu, J. Schulz, M. Barth, and P. Koopmans. Application of pins radiofrequency pulses to reduce power deposition in rare/turbo spin echo imaging of the human head. *Magn Reson Med*, 71:44–49, 2014.

[102] D. Norris, P. Koopmans, R. Boyacioğlu, and M. Barth. Power independent of number of slices (pins) radiofrequency pulses for low-power simultaneous multislice excitation. *Magn Reson Med*, 66:1234–1240, 2011.

[103] D. G. Norris. Principles of magnetic resonance assessment of brain function. *Journal of magnetic resonance imaging*, 23(6):794–807, 2006.

[104] D. G. Norris. Spin-echo fMRI: The poor relation? *NeuroImage*, 62(2):1109–1115, aug 2012.

[105] D. G. Norris and J. Schulz. Reduced peak power in paired excitation and refocusing multiband pulses by quadratic phase modulation in the spatial domain. In *Proceedings of the 24th Annual Meeting of ISMRM, Singapore,*, 2016.

[106] D. G. Norris, S. Zysset, T. Mildner, and C. J. Wiggins. An investigation of the value of spin-echo-based fmri using a stroop color–word matching task and epi at 3 t. *Neuroimage*, 15(3):719–726, 2002.

[107] S. Ogawa, T.-M. Lee, A. R. Kay, and D. W. Tank. Brain magnetic resonance imaging with contrast dependent on blood oxygenation. *Proceedings of the National Academy of Sciences*, 87(24):9868–9872, 1990.

[108] S. Ogawa, R. Menon, D. Tank, S. Kim, H. Merkle, J. Ellermann, and K. Ugurbil. Functional brain mapping by blood oxygenation level-dependent contrast magnetic resonance imaging. a comparison of signal characteristics with a biophysical model. *Biophysical journal*, 64(3):803, 1993.

[109] S. Ogawa, D. W. Tank, R. Menon, J. M. Ellermann, S. G. Kim, H. Merkle, and K. Ugurbil. Intrinsic signal changes accompanying sensory stimulation: functional brain mapping with magnetic resonance imaging. *Proc Natl Acad Sci U S A*, 89(13):5951–5, Jul 1992.

[110] C. A. Olman, P.-F. V. de Moortele, J. F. Schumacher, J. R. Guy, K. Uğurbil, and E. Yacoub. Retinotopic mapping with spin echo BOLD at 7T. *Magnetic Resonance Imaging*, 28(9):1258–1269, nov 2010.

[111] C. A. Olman and E. Yacoub. High-field fMRI for human applications: An overview of spatial resolution and signal specificity. *The Open Neuroimaging Journal*, 5(Suppl 1):74–89, nov 2011.

[112] D. L. Parker, C. Yuan, and D. D. Blatter. MR angiography by multiple thin slab 3D acquisition. *Magnetic Resonance in Medicine*, 17(2):434–451, feb 1991.

[113] L. M. Parkes, J. V. Schwarzbach, A. A. Bouts, R. h R. Deckers, P. Pullens, C. M. Kerskens, and D. G. Norris. Quantifying the spatial resolution of the gradient echo and spin echo BOLD response at 3 Tesla. *Magnetic Resonance in Medicine*, 54(6):1465–1472, 2005.

[114] D. M. Patel, R. S. Tubbs, G. Pate, J. M. Johnston, and J. P. Blount. Fast-sequence MRI studies for surveillance imaging in pediatric hydrocephalus. *Journal of Neurosurgery: Pediatrics*, 13(4):440–447, apr 2014.

[115] M. R. Patel, R. A. Klufas, R. A. Alberico, and R. R. Edelman. Half-fourier acquisition single-shot turbo spin-echo (haste) mr: comparison with fast spin-echo mr in diseases of the brain. *American journal of neuroradiology*, 18(9):1635–1640, 1997.

[116] W. Pauli. Discovery of nulear spin to explain the hyperfine structure of the atomic spectra. *Naturwissenschaften*, 12:74, 1924.

[117] J. Pauly, P. Le Roux, D. Nishimura, and A. Macovski. Parameter relations for the shinnar-le roux selective excitation pulse design algorithm [nmr imaging]. *IEEE Transactions on Medical Imaging*, 10(1):53–65, Mar. 1991.

[118] D. Pflugfelder, K. Vahedipour, K. Uludağ, N. J. Shah, and T. StÃűcker. On the numerically predicted spatial BOLD fMRI specificity for spin echo sequences. *Magnetic Resonance Imaging*, 29(9):1195–1204, nov 2011.

[119] J. R. Polimeni, H. Bhat, T. Witzel, T. Benner, T. Feiweier, S. J. Inati, V. Renvall, K. Heberlein, and L. L. Wald. Reducing sensitivity losses due to respiration and motion in accelerated echo planar imaging by reordering the autocalibration data acquisition. *Magnetic Resonance in Medicine*, 75(2):665–679, mar 2015.

[120] B. A. Poser, R. J. Anderson, B. Guérin, K. Setsompop, W. Deng, A. Mareyam, P. Serano, L. L. Wald, and V. A. Stenger. Simultaneous multislice excitation by parallel transmission. *Magnetic Resonance in Medicine*, 71(4):1416–1427, may 2013.

[121] B. A. Poser, M. J. Versluis, J. M. Hoogduin, and D. G. Norris. BOLD contrast sensitivity enhancement and artifact reduction with multiecho EPI: Parallel-acquired inhomogeneity-desensitized fMRI. *Magnetic Resonance in Medicine*, 55(6):1227–1235, 2006.

[122] M. R. Prince, H. L. Zhang, G. H. Roditi, T. Leiner, and W. Kucharczyk. Risk factors for NSF: A literature review. *Journal of Magnetic Resonance Imaging*, 30(6):1298–1308, dec 2009.

[123] K. P. Pruessmann, M. Weiger, M. B. Scheidegger, P. Boesiger, et al. Sense: sensitivity encoding for fast mri. *Magnetic resonance in medicine*, 42(5):952–962, 1999.

[124] E. M. Purcell, H. Torrey, and R. V. Pound. Resonance absorption by nuclear magnetic moments in a solid. *Physical review*, 69(1-2):37, 1946.

[125] I. Rabi, S. Millman, P. Kusch, and J. Zacharias. The molecular beam resonance method for measuring nuclear magnetic moments. the magnetic moments of $_3$li^6, $_3$li^7 and $_9$f^{19}. *Physical review*, 55(6):526, 1939.

[126] J. Ridgway. Cardiovascular magnetic resonance physics for clinicians: part i. *J Cardiovasc Magn Reson*, 12(1):71, 2010.

[127] S. D. Robinson, J. Pripfl, H. Bauer, and E. Moser. The impact of EPI voxel size on SNR and BOLD sensitivity in the anterior medio-temporal lobe: a comparative group study of deactivation of the default mode. *Magnetic Resonance Materials in Physics, Biology and Medicine*, 21(4):279–290, jul 2008.

[128] P. Robson, A. Grant, A. Madhuranthakam, R. Lattanzi, D. Sodickson, and C. McKenzie. Comprehensive quantification of signal-to-noise ratio and g-factor for image-based and k-space-based parallel imaging reconstructions. *Magn Reson Med*, 60:895–907, 2008.

[129] J. Roether, R. Knab, F. Hamzei, J. Fiehler, J. R. Reichenbach, C. Büchel, and C. Weiller. Negative dip in bold fmri is caused by blood flow–oxygen consumption uncoupling in humans. *Neuroimage*, 15(1):98–102, Jan 2002.

[130] F. Rousseau, K. Kim, C. Studholme, M. Koob, and J. L. Dietemann. On super-resolution for fetal brain MRI. In *Medical Image Computing and Computer-Assisted Intervention – MICCAI 2010*, pages 355–362. Springer Nature, 2010.

[131] P. L. Roux and R. S. Hinks. Stabilization of echo amplitudes in FSE sequences. *Magnetic Resonance in Medicine*, 30(2):183–190, aug 1993.

[132] Z. Rumboldt and M. Marotti. Magnetization transfer, HASTE, and FLAIR imaging. *Magnetic Resonance Imaging Clinics of North America*, 11(3):471–492, aug 2003.

[133] C. F. Schmidt, P. Boesiger, and A. Ishai. Comparison of fMRI activation as measured with gradient- and spin-echo EPI during visual perception. *NeuroImage*, 26(3):852–859, jul 2005.

[134] R. Schulte, A. Henning, J. Tsao, P. Boesiger, and K. Pruessmann. Design of broadband RF pulses with polynomial-phase response. *Journal of Magnetic Resonance*, 186(2):167–175, jun 2007.

[135] J. Schulz, R. Boyacioğlu, and D. G. Norris. Multiband multislab 3d time-of-flight magnetic resonance angiography for reduced acquisition time and improved sensitivity. *Magnetic Resonance in Medicine*, 75(4):1662–1668, may 2015.

[136] C. Schwarzbauer, T. Mildner, W. Heinke, M. Brett, and R. Deichmann. Dual echo EPI – the method of choice for fMRI in the presence of magnetic field inhomogeneities? *NeuroImage*, 49(1):316–326, jan 2010.

[137] K. Setsompop, J. Cohen-Adad, B. Gagoski, T. Raij, A. Yendiki, B. Keil, J. Wedeen Van, and L. Wald. Improving diffusion mri using simultaneous multi-slice echo planar imaging. *Neuroimage 2012;63:569-580*, 63:569–580, 2012.

[138] K. Setsompop, B. Gagoski, J. Polimeni, T. Witzel, J. Wedeen Van, and L. Wald. Blipped-controlled aliasing in parallel imaging for simultaneous multislice echo planar imaging with reduced g-factor penalty. *Magn Reson Med*, 67:1210–1224, 2012.

[139] K. Setsompop, J. Polimeni, H. Bhat, and L. Wald. Characterization of artifactual correlation in highly-accelerated simultaneous multi-slice (sms) fmri acquisitions. In *Proceedings of 21st Annual Meeting of ISMRM, Salt Lake City, Utah, USA*, 2013.

[140] A. Sharma, M. Lustig, and W. A. Grissom. Root-flipped multiband refocusing pulses. *Magnetic Resonance in Medicine*, 75(1):227–237, feb 2015.

[141] D. K. Sodickson and W. J. Manning. Simultaneous acquisition of spatial harmonics (smash): fast imaging with radiofrequency coil arrays. *Magnetic Resonance in Medicine*, 38(4):591–603, 1997.

[142] O. Speck and J. Hennig. Functional imaging by i0- and t2*-parameter mapping using multi-image EPI. *Magnetic Resonance in Medicine*, 40(2):243–248, aug 1998.

[143] B. Stefanovic and G. B. Pike. Human whole-blood relaxometry at 1.5 t: Assessment of diffusion and exchange models. *Magnetic resonance in medicine*, 52(4):716–723, 2004.

[144] M. J. Stehling, A. Howseman, R. J. Ordidge, B. Chapman, R. Turner, R. Coxon, P. Glover, P. Mansfield, and R. Coupland. Whole-body echo-planar mr imaging at 0.5 t. *Radiology*, 170(1):257–263, 1989.

[145] V. A. Stenger, F. E. Boada, and D. C. Noll. Three-dimensional tailored RF pulses for the reduction of susceptibility artifacts in t2*-weighted functional MRI. *Magnetic Resonance in Medicine*, 44(4):525–531, 2000.

[146] C. Studholme, R. Constable, and J. Duncan. Accurate alignment of functional EPI data to anatomical MRI using a physics-based distortion model. *IEEE Transactions on Medical Imaging*, 19(11):1115–1127, 2000.

[147] T. Sugahara, Y. Korogi, T. Hirai, S. Hamatake, I. Ikushima, Y. Shigematu, and M. Takahashi. Comparison of HASTE and segmented-HASTE sequences with a t2-weighted fast spin-echo sequence in the screening evaluation of the brain. *American Journal of Roentgenology*, 169(5):1401–1410, nov 1997.

[148] Y. Tang, Y. Yamashita, and M. Takahashi. Invited. ultrafast t2-weighted imaging of the abdomen and pelvis: Use of single shot fast spin-echo imaging. *Journal of Magnetic Resonance Imaging*, 8(2):384–390, mar 1998.

[149] H. S. Thomsen. Nephrogenic systemic fibrosis: a serious adverse reaction to gadolinium – 1997–2006–2016. part 2. *Acta Radiologica*, 57(6):643–648, jun 2016.

[150] C. Triantafyllou, R. Hoge, G. Krueger, C. Wiggins, A. Potthast, G. Wiggins, and L. Wald. Comparison of physiological noise at 1.5 T, 3 T and 7 T and optimization of fMRI acquisition parameters. *NeuroImage*, 26(1):243–250, may 2005.

[151] C. Triantafyllou, J. Polimeni, M. Elschot, and L. Wald. Physiological noise in gradient echo and spin echo epi at 3t and 7t. In *Proceedings of the 17th Annual Meeting of ISMRM, Honolulu, Hawaii, USA*, 2009.

[152] W. D. Turnipseed, T. W. Kennell, P. A. Turski, C. W. Acher, and J. R. Hoch. Combined use of duplex imaging and magnetic resonance angiography for evaluation of patients with

symptomatic ipsilateral high-grade carotid stenosis. *Journal of Vascular Surgery*, 17(5):832–840, may 1993.

[153] K. Uğurbil, G. Adriany, P. Andersen, W. Chen, R. Gruetter, X. Hu, H. Merkle, D.-S. Kim, S.-G. Kim, J. Strupp, X. H. Zhu, and S. Ogawa. Magnetic resonance studies of brain function and neurochemistry. *Annual Review of Biomedical Engineering*, 2(1):633–660, aug 2000.

[154] K. Uğurbil, J. Xu, E. J. Auerbach, S. Moeller, A. T. Vu, J. M. Duarte-Carvajalino, C. Lenglet, X. Wu, S. Schmitter, P. F. V. de Moortele, J. Strupp, G. Sapiro, F. D. Martino, D. Wang, N. Harel, M. Garwood, L. Chen, D. A. Feinberg, S. M. Smith, K. L. Miller, S. N. Sotiropoulos, S. Jbabdi, J. L. Andersson, T. E. Behrens, M. F. Glasser, D. C. V. Essen, and E. Yacoub. Pushing spatial and temporal resolution for functional and diffusion MRI in the human connectome project. *NeuroImage*, 80:80–104, oct 2013.

[155] K. Uludağ, B. Müller-Bierl, and K. Uğurbil. An integrative model for neuronal activity-induced signal changes for gradient and spin echo functional imaging. *NeuroImage*, 48(1):150–165, oct 2009.

[156] P. van Gelderen, J. Duyn, N. Ramsey, G. Liu, and C. Moonen. The PRESTO technique for fMRI. *NeuroImage*, 62(2):676–681, aug 2012.

[157] P. van Gelderen, N. Ramsey, G. Liu, J. Duyn, J. Frank, D. Weinberger, and C. Moonen. Three-dimensional functional magnetic resonance imaging of human brain on a clinical 1.5-t scanner. *PNAS*, 29(15):6906–6910, 1995.

[158] A. G. van Norden, K. F. de Laat, R. A. Gons, I. W. van Uden, E. J. van Dijk, L. J. van Oudheusden, R. A. Esselink, B. R. Bloem, B. G. van Engelen, M. J. Zwarts, I. Tendolkar, M. G. Olde-Rikkert, M. J. van der Vlugt, M. P. Zwiers, D. G. Norris, and F.-E. de Leeuw. Causes and consequences of cerebral small vessel disease. the RUN DMC study: a prospective cohort study. study rationale and protocol. *BMC Neurology*, 11(1), feb 2011.

[159] P. C. M. van Zijl, J. Hua, and H. Lu. The bold post-stimulus undershoot, one of the most debated issues in fmri. *Neuroimage*, 62(2):1092–102, Aug 2012.

[160] E. Visser, S. Qin, and M. Zwiers. Epi distortion correction by constrained nonlinear coregistration improves group fmri. In *Proceedings of the 18th Annual Meeting of ISMRM, Stockholm, Sweden*, 2010.

[161] M. White. Magnetic resonance angiography of the brain and neck: Techniques and applications. *Seminars in Cerebrovascular Diseases and Stroke*, 1(4):287–302, dec 2001.

[162] G. Wilms, H. Bosmans, P. Demaerel, and G. Marchal. Magnetic resonance angiography of the intracranial vessels. *European Journal of Radiology*, 38(1):10–18, apr 2001.

[163] E. Wong. Optimized phase schedules for minimizing peak rf power in simultaneous multislice rf excitation pulses. In *Proceedings of the 20th Annual Meeting of ISMRM, Melbourne, Australia*, page 2209, 2012.

[164] M. Woolrich. Robust group analysis using outlier inference. *NeuroImage*, 41(2):286–301, jun 2008.

[165] M. W. Woolrich, T. E. Behrens, C. F. Beckmann, M. Jenkinson, and S. M. Smith. Multilevel linear modelling for FMRI group analysis using Bayesian inference. *NeuroImage*, 21(4):1732–1747, apr 2004.

[166] E. Yacoub, P.-F. V. D. Moortele, A. Shmuel, and K. Uğurbil. Signal and noise characteristics of hahn SE and GE BOLD fMRI at 7 T in humans. *NeuroImage*, 24(3):738–750, feb 2005.

[167] E. Yacoub, A. Shmuel, N. Logothetis, and K. Uğurbil. Robust detection of ocular dominance columns in humans using hahn spin echo BOLD functional MRI at 7 Tesla. *NeuroImage*, 37(4):1161–1177, oct 2007.

[168] S. Zysset, K. Müller, G. Lohmann, and D. von Cramon. Color-word matching stroop task: Separating interference and response conflict. *NeuroImage*, 13(1):29–36, jan 2001.

Acknowledgments

This part is devoted to all of those people who have supported me throughout the past years. Without this constant support and help, this thesis would not have been as it is. I've been supported directly and indirectly, scientifically and privately, a lot and just slightly, but a big THANK YOU goes to everyone. A few people, I'd still like to mention specifically:

I will start with my promoter **David G. Norris**. You have given me an exceptional opportunity by working in your group and supervising my thesis. During the years of my PhD-project, I've learned a lot about the world of MR and how to work scientifically which was due to your long experience and will to distribute your knowledge. With an open ear at all times and a sharp focus on the work, you manage in your very own way to motivate and support while creating a warm working atmosphere. Although not all "2-week-projects" turned out to be done within 2 weeks, I appreciate your enthusiasm about the work we've been doing, your patience, dedication and perseverance. I am very grateful to have been your PhD student. Thank you.

I would also like to thank the **MR-techniques group**, current and former members. I really enjoyed working in this international team and getting to know so many different people. Whether it was at the group drinks, the retreat or during meetings, I always felt like everyone is trying to use his/her expertise to help solving daily and/or specific problems. It is really a great team which welcomes any new and returning members with open arms at all times.
A special thanks goes of course to those which I've been working with most closely:
Rasim, I met you at the interview and you helped me from the first day finding my place at the Donders. Thanks for that!
Lauren, thanks for the senior knowledge and your incredible patience.
And **Tim**, thanks so much for taking the time and translating my summary chapter.

I also would like to thank the **Donders** as a whole. It is a great interdisciplinary place to work at with a fantastic spirit and wonderful atmosphere.
Tildie, the good soul of the Donders, you are really pulling the strings. Thank you for taking care of pretty much everything.
Marek and the TG-team, thank you for the wonderful support. Without you, there would be no research at this place.
Paul, a special thanks to you as well for always helping out and keeping the basement up and running.
Thanks also to all the people at the **Erwin L. Hahn Institute**. It's always been fun to "visit" and "play" with the 7T. Whereas the control room in Nijmegen always seems super busy, the atmosphere in Essen was rather calm creating a nice working environment.

I also don't want to forget external collaborations such as **Lausanne**, **Boston** or **Maastricht**. Working with you really felt like "learning from the best".

Before starting my PhD-project, I was encouraged by colleagues and friends from my studies and the department of nuclear particle physics in **Münster** to take this step and follow my interest of physical applications in medicine. Thank you for that!

There is so much more to life besides work... :
Although we have very different personalities, **Kevin**, in a lot of ways, we are also the same. Thank you for your humor and circumventing mama's and papa's rules without letting them know.
Ganz besonders möchte ich euch, **Oma und Opa**, danken. Ihr seid immer für mich da gewesen und versucht noch stets zu helfen, wo es nur geht. Ich weiss, dass ihr verdammt stolz auch mich seid, aber ich weiss auch, dass ich ohne euch nicht so weit gekommen wäre. Danke, dass ihr immer ein offenes Ohr habt und eure Tür immer offen steht.
Es ist noch schwerer die Dankbarkeit, die ich euch, **Mama und Papa**, entgegen bringe in Worte zu fassen. Ich bin euch natürlich unendlich dankbar, dass ihr immer für mich da seid und man wirklich immer auf euch zählen kann. Aber ich bin euch auch sehr dankbar dafür, dass ihr

mich immer ermutigt habt meinen Weg zu gehen, meine eigenen Entscheidungen zu treffen, Konsequenzen zu tragen und so zu sein, wie ich nun mal bin.
Last, but not least.... **Lilly und Lucy**, wie schön ist es doch euch wachsen und lachen zu sehen... und **Johannes**, DANKE für deine unendliche Geduld and being a fantastic husband, dad and friend op zo veel verschillende manieren.

About the Author

Jenni was born in Gelsenkirchen (Germany) in September 1986. She graduated from Belmont Secondary School (Victoria, BC, Canada) in 2004 and from the Heisenberg-Gymnasium (Gladbeck, Germany) with the Abitur in 2006. During her school time, she was very active in music and dancing. Besides playing violin in an orchestra, Jenni did ballet and show dance while further teaching dancing classes for children in the local dance club. In Fall 2016, Jenni started studying Physics at the University of Münster (Germany). As an undergraduate, she got in touch with various facets of Physics and decided to specialize in “nuclear particle physics” and “medical physics and biophysics”. For her Diploma, she worked in the group of Prof. Dr. Johannes P. Wessels on “positron-emission-tomography (PET)” research and was involved in teaching sessions and lab classes for medical students. Her thesis was on the topic of “Development of small animal PET detectors based on multi-wire proportional chambers” and in collaboration with the SFB 656 MoBil ("Molekulare kardiovaskuläre Bildgebung") strengthening her interest in the combination of physics and medical applications.

To broaden her scientific as well as personal horizon, Jenni switched subjects and moved to the Netherlands to work in the MR Techniques for Brain Function research group at the Donders Institute for Brain, Cognition and Behaviour (Centre for Cognitive Neuroimaging) at the Radboud University Nijmegen. Her PhD project on “Pulse Sequence Development” for Neuroimaging was supervised and promoted by Prof. Dr. David G. Norris. She especially concentrated on the development of methods for artifact-free and accelerated acquisition techniques in functional magnetic resonance imaging, angiography and fast spin-echo imaging.

During her Diploma and PhD project, Jenni presented her work at various (international) conferences and took part in different workshops.

List of Publications

Boyacioğlu, R., **Schulz, J.**, and Norris, D. G. (2016). Multiband echo-shifted echo planar imaging. Magnetic resonance in medicine.

Schulz, J., Boyacioğlu, R., and Norris, D. G. (2015). Multiband multislab 3D time-of-flight magnetic resonance angiography for reduced acquisition time and improved sensitivity. Magnetic resonance in medicine.

Boyacioğlu, R., **Schulz, J.**, Koopmans, P. J., Barth, M., and Norris, D. G. (2015). Improved sensitivity and specificity for resting state and task fMRI with multiband multi-echo EPI compared to multi-echo EPI at 7T. Neuroimage, 119, 352-361.

Boyacioğlu, R., **Schulz, J.**, Müller, N. C., Koopmans, P. J., Barth, M., and Norris, D. G. (2014). Whole brain, high resolution multiband spin-echo EPI fMRI at 7T: a comparison with gradient-echo EPI using a color-word Stroop task. Neuroimage, 97, 142-150.

Norris, D. G., Boyacioğlu, R., **Schulz, J.**, Barth, M., and Koopmans, P. J. (2014). Application of PINS radiofrequency pulses to reduce power deposition in RARE/turbo spin echo imaging of the human head. Magnetic resonance in medicine, 71(1), 44-49.

Schulz, J., Marques, J. P., ter Telgte, A., van Dorst, A., de Leeuw, F., Meijer, F. J. A. and Norris, D. G. (2017). Clinical application of Half Fourier Acquisition Single Shot Turbo Spin Echo (HASTE) imaging accelerated by simultaneous multi-slice acquisition (under review)

Donders Graduate School for Cognitive Neuroscience

For a successful research Institute, it is vital to train the next generation of young scientists. To achieve this goal, the Donders Institute for Brain, Cognition and Behaviour established the Donders Graduate School for Cognitive Neuroscience (DGCN), which was officially recognised as a national graduate school in 2009. The Graduate School covers training at both Master's and PhD level and provides an excellent educational context fully aligned with the research programme of the Donders Institute.

The school successfully attracts highly talented national and international students in biology, physics, psycholinguistics, psychology, behavioral science, medicine and related disciplines. Selective admission and assessment centers guarantee the enrolment of the best and most motivated students.

The DGCN tracks the career of PhD graduates carefully. More than 50% of PhD alumni show a continuation in academia with postdoc positions at top institutes worldwide, e.g. Stanford University, University of Oxford, University of Cambridge, UCL London, MPI Leipzig, Hanyang University in South Korea, NTNU Norway, University of Illinois, North Western University, Northeastern University in Boston, ETH Zürich, University of Vienna etc.. Positions outside academia spread among the following sectors: specialists in a medical environment, mainly in genetics, geriatrics, psychiatry and neurology. Specialists in a psychological environment, e.g. as specialist in neuropsychology, psychological diagnostics or therapy. Positions in higher education as coordinators or lecturers. A smaller percentage enters business as research consultants, analysts or head of research and development. Fewer graduates stay in a research environment as lab coordinators, technical support or policy advisors. Upcoming possibilities are positions in the IT sector and management position in pharmaceutical industry. In general, the PhDs graduates almost invariably continue with high-quality positions that play an important role in our knowledge economy.

For more information on the DGCN as well as past and upcoming defenses please visit: `http://www.ru.nl/donders/graduate-school/phd/`